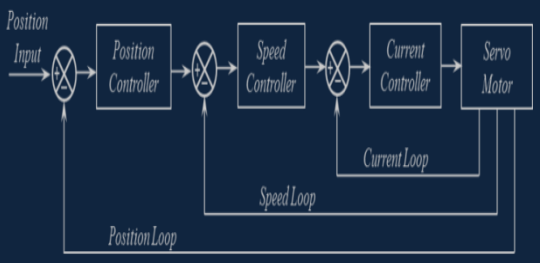

International Advanced Researches and Engineering Journal

e-ISSN

2618-575X

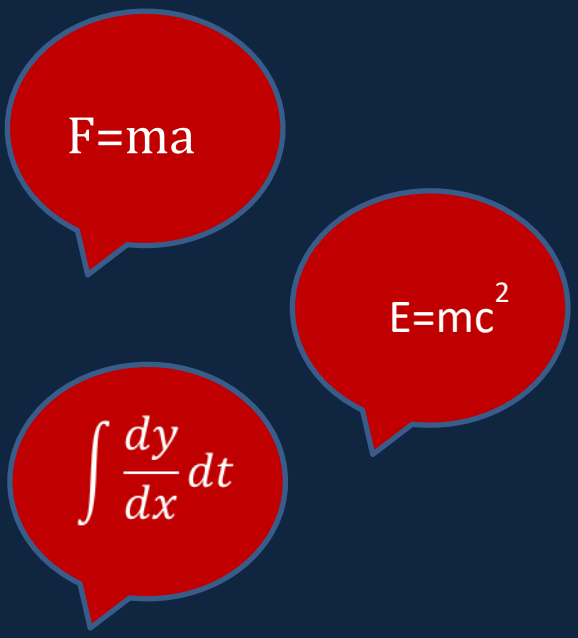

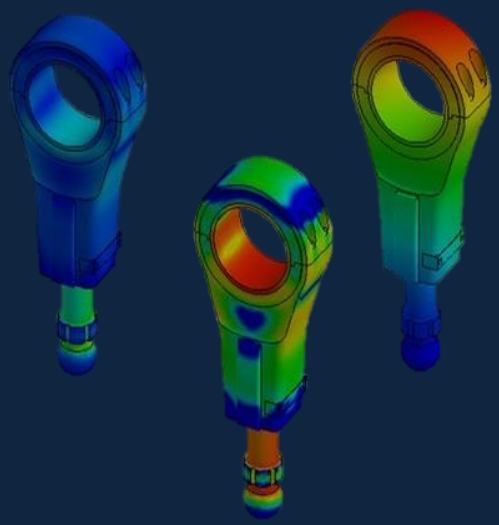

Volume 07 | **Issue** 03

December, 2023

e-ISSN: 2618-575X

Available online at www.dergipark.org.tr/en

INTERNATIONAL ADVANCED RESEARCHES
and
ENGINEERING JOURNAL

Journal homepage: www.dergipark.org.tr/en/pub/iarej

International
Open Access

Volume 07
Issue 03

December, 2023

International Advanced Researches and Engineering Journal (IAREJ) is a double-blind peer-reviewed and publicly available online journal that has Editorial Board (https://dergipark.org.tr/en/pub/iarej/board). The editor in chief of IAREJ welcomes the submissions that cover theoretical and/or applied researches on **Engineering** and related science with Engineering. The publication language of the Journal is **English**. **Writing Rules** are given in Author Guidelines (https://dergipark.org.tr/en/pub/iarej/writing-rules). IAREJ publishes **original papers** that are research papers and technical review papers.

IAREJ publication, which is **open access**, is **free of charge**. There is no article submission and processing charges (APCs).

IAREJ is indexed & abstracted in:

Crossref (Doi prefix: 10.35860/iarej.)
Directory of Open Access Scholarly Researches (ROAD)
Directory of Research Journals Indexing (DRJI)
EBSCO
Google Scholar
Index Copernicus (ICI Journal Master List)
J-Gate
TUBITAK ULAKBIM TR Dizin (TR index)
WorldCAT

Authors are responsible from the copyrights of the figures and the contents of the manuscripts, accuracy of the references, quotations and proposed ideas and the Publication Ethics (https://dergipark.org.tr/en/pub/iarej/page/4240).

e-ISSN: 2618-575X

Available online at www.dergipark.org.tr/en

INTERNATIONAL ADVANCED RESEARCHES
and
ENGINEERING JOURNAL

Journal homepage: www.dergipark.org.tr/en/pub/iarej

International
Open Access

Volume 07
Issue 03

December, 2023

TABLE of CONTENTS

RESEARCH ARTICLES

Available online at www.dergipark.org.tr/en

INTERNATIONAL ADVANCED RESEARCHES and ENGINEERING JOURNAL

Journal homepage: www.dergipark.org.tr/en/pub/iarej

e-ISSN: 2618-575X

International Open Access

Volume 07
Issue 03

December, 2023

Research Article

Optimal PID control with anti-windup in neutralization process

ZeynepYilmazer Hitit [a,*], ***Ismet Kocer*** [a], ***Gokce Kus*** [a], ***Nermin Zeynep Arslan*** [a], ***Elif Pinar Dal*** [a] **and** ***Habipcan Koz*** [a]

[a]*Ankara University, Faculty of Engineering, Department of Chemical Engineering; 06100 Tandogan, Ankara; Turkey*

ARTICLE INFO

Article history:
Received 24 February 2023
Accepted 31 October 2023
Published 15 December 2023

Keywords:
Anti-wind up
Automation
Neutralization
PID controller
Process control

ABSTRACT

PID control, which is a type of automation, was used to ensure that neutralization takes place in a controlled manner. To determine the PID parameters of the system with the Cohen-Coon tuning method, two different dynamic experiments were carried out for pH and temperature in the first stage, and the transfer function and model parameters were found. In the experiment carried out for the pH variable; time constant (τ) is 59 s, dead time (Θ) is 261 s and steady state gain (K) is read from the graph as 14,72, while PID parameters are calculated as K_C =0.0375, τ_I =315.759 s and τ_D =52.601 s. Likewise, while τ=1402 s., Θ= 88 s, and K=-6 were read for the temperature variable, the PID parameters were calculated as K_C =6.196, τ_I =47.23 s, and τ_D =-19.20 s. The determined controller parameters were used as initial parameters and simulated using the S-function block via MATLAB (2007b). The pH set range was coded as 6.5-8.5 and T_{set} for temperature was coded as 22 °C. As a result of the oscillation observed due to the nature of the PID control parameters that are intended to be controlled, the safe operation of the process and the desired set values are ensured. When the obtained PID controller parameters were applied to the neutralization reaction, the PID control successfully controlled the reactor temperature and pH and eliminated possible hazards in operation. Anti-windup provides better control rather than traditional PID control method.

1. Introduction

Acids are substances that give hydronium or hydroxyl ions to their solutions when dissolved in water. Bases are substances that increase the hydroxide ion concentration in their aqueous solutions. When acids and bases come together, they give neutralization reactions [1]. Acids are classified according to their strength. Acids that have a high tendency to ionize in their aqueous solutions and are assumed to be 100% ionized in theory are called strong acids. Similarly, bases that can ionize close to 100% in water in theory are called strong bases [2].

pH is the negative logarithm of the hydrogen ion concentration in the aqueous solution. Accordingly, while pH is 7 in neutral solutions, pH is less than 7 in acid solutions and pH is greater than 7 in base solutions [3]. The molecular structure of Hydrochloric Acid (HCl), an example of a strong acid, is quite simple. Hydrochloric acid has a pronounced effect on bases [4]. This effect can be seen as the temperature rises rapidly as a result of the reaction of acids and bases. Hydrochloric acid can be used to lower the basicity or increase the acidity in a solution. For example, if hydrochloric acid is dropped into a solution containing OH- ions, the base in the solution is replaced by water and H+ ions [5]. Hydrochloric acid should not be released directly into the environment. Inhalation of even a small amount of gaseous hydrochloric acid poses a great risk to the entire respiratory tract for human health [6, 7].

The formation of water and salt as a result of the reaction of the H+ ion in the acid with the OH- ion in the base is called the neutralization reaction. Not every acid and base can be used as a reactant in the reaction [8]. The main properties sought in acids and bases to be used for this purpose are as follows; they must dissociate into ions to a great extent in the aqueous medium, are not volatile in their dilute solutions, dilute solutions are not easily affected by air and light, dilute solutions must not be strongly oxidizing or reducing, and the salts produced

* Corresponding author. Tel.: +90 312 203 3433; Fax: +90 312 212 7464.
E-mail addresses: zyilmazer@ankara.edu.tr *(Z.Y. Hitit,* issmetkocer@gmail.com *(I. Kocer),* gokceks09@gmail.com *(G. Kus),* *neparslan@outlook.com* *(N.Z.Arslan),* pinardal47@gmail.com *(E.P.Dal),* *kozhabipcan@gmail.com* *(H. Koz)*
ORCID: 0000-0001-9078-191X *(Z.Y. Hitit), 0000-0001-8319-5437 (I. Kocer), 0000-0001-9931-3899 (G. Kus), 0000-0001-7221-8058 (N.Z. Arslan), 0000-0001-5060-1275 (E.P.Dal), 0000-0002-1054-6993 (H. Koz)*
DOI: 10.35860/iarej.1256107

during neutralization should dissolve well in water. In this respect, HCl and NaOH acid-base pairs (Equation1) are suitable chemicals for neutralization [9, 10].

$$HCl + NaOH \rightarrow H_2O + NaCl + Heat \quad (1)$$

For neutralization to occur, the number of moles of hydrogen or hydronium ions from the acid must be equal to the number of moles of hydroxide ions from the base [11]. Accordingly, 1 mol of HCl can neutralize with 1 mol of NaOH. Depending on the strength of the acid and base used, the quality of the salt formed as a result of the reaction changes. The salt obtained (NaCl) is a neutral salt, since HCl and NaOH are strong acid-base pairs [12].

HCl, which is generally obtained as a by-product (production of common organic chemicals such as chlorination in the chemical industry, sodium hypochlorite, Teflon, polyvinyl chloride, and perchloroethylene) may not be at a suitable concentration or purity for use as an input in any process. Therefore, it has a destructive feature on the environment and must be disposed of or converted to another harmless form [13]. Based on this information, one of the best methods that can be applied is to obtain salt (NaCl) by performing a neutralization reaction with sodium hydroxide (NaOH). However, it is known that it is difficult to control the reaction parameters by manual methods due to the high rate ($1x10^{-14}$ L/gmol.s) of this reaction [14]. For this reason, neutralization systems are supported by PID control, which is a type of automation [15, 16]. Automatic controllers which are used to control important parameters such as pH, temperature, level, and keep process variables at desired design values in order to maintain the entire chemical process efficiently.

In this study, it was aimed to keep the pH and temperature parameters within the targeted value range throughout the reaction. PID control method, which provides a safe, environmentally friendly and automatic process, is used to keep the parameters within the desired range. Process control systems provide the opportunity to make changes on other process variables while keeping a process variable constant in order to control the above-mentioned variables. In this way, PID control method ensures that the process works in line with the desired values [17, 18].

Since the HCl-NaOH reaction discussed in this study is an exothermic reaction, it is aimed to determine the system parameters at the laboratory scale and design the process control system accordingly. Process control includes reaching the target and maintaining the current situation after reaching the target in the process extending from the input of the desired target to the result. Control parameters vary according to the type of process considered. In order to ensure product quality and continuity, parameters affecting the course of the process such as product concentration, temperature, pH and flow rate should be controlled. Thus, neutralization is achieved successfully [19, 20].

2. Materials and Method

2.1. Experimental Setup

In this study, it is aimed to maintain the process in maximum efficiency and safe conditions while removing HCl. In the system, a reactor made of glass, with a volume of 2 L and a jacket volume of 1.5 L, was used in continuous operation. In order to ensure homogenization in the system, a mechanical agitator was used. A thermocouple was added into the reactor to determine the temperature changes that will occur due to the nature of the reaction used in the experiment. So as to prevent the heat that will be released during the reaction from affecting the process negatively, cooling water is passed through the jacket around the reactor with the help of a peristaltic pump. In order to monitor the pH and temperature desired to be controlled, a pH probe and thermocouple was placed in the system. Temperature, conductivity, pH, and pump flow rates which are desired to be recorded throughout the experiment are provided using a computer and electronic circuit equipment. The HCl that should be neutralized was chosen at 0.014 M as waste at a constant flow rate of 0.193 L/min. To realize neutralization properly, a 1:1 (mol/mol) ratio of acid and base should react. Varying flow rates of NaOH based on controller output value was used to neutralize HCl. Therefore, 0.014 M HCl and 0.025 M NaOH were prepared in beakers and fed to the reactor by peristaltic pumps. The NaCl salt to be obtained during this reaction was removed from the system in the form of anaqueous solution. In Figure 1, PID control experimental setup is given.

2.2. Transfer Function and Closed Loop Control System

The dynamic relationship between an input and an output variable in a process can be explained by the transfer function (Equation2). In a system where simultaneous control of the pH and temperature in the reactor is desired, the feedback control loop operates to ensure that the reactor temperature and pH value in the system are controlled at the targeted set values. This control loop

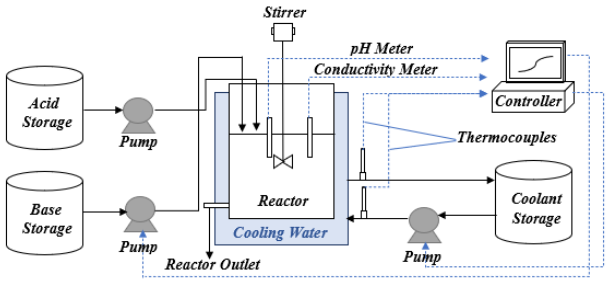

Figure 1. PID Control Experimental Setup

takes place by adjusting the flow rate of the cooling water through the cooling jacket and the flow rate of the base pump for temperature and pH control, respectively [21, 22].

In the feedback control system for temperature, electrical signals are received using a thermocouple of the reactor internal temperature and converted into digital signals by means of a transducer [23, 24]. Thus, these signals can be read with the help of a computer. Then, in order to provide temperature control, the difference between the temperature values measured with the help of a thermocouple and the temperature set value is determined and the error value is calculated. According to this error value, a manipulated variable signal is sent to the cooling water pump by the controller, and temperature control is provided.

For pH control, while the electrical signal is given to the computer by the pH meter, the difference between the measured pH value and the pH set value is calculated in the same way, and the base pump flow rate changes according to the error value.

Considering the data obtained after the system identification with dynamic response analysis, it was concluded that the system is a first order plus dead time model. Accordingly, the transfer function of the mentioned model is given in Equation 2.

$$G(s) = \frac{K(e^{-\theta s})}{\tau s+1} \qquad (2)$$

Where G(s) is the transfer function, K is the process gain, θ is the dead time and τ is the time constant of process. To find the model parameters along with the transfer function the process reaction curve method was used. Negative step effect was given to the flow rate of the cooling water whereas, positive step effect was given to the base pump after the control system became stable. The temperature of the cooling water at the entrance and exit of the jacket with the thermocouples placed in the reactor and the pH data with the pH probe placed in the reactor were continuously recorded. To control the desired neutralization reaction with automation using the information obtained, PID control parameters were calculated by Cohen-Coon tuning method, and these values were used in control experiments using MATLAB Simulink as initial parameters and simulated with the S-function block with the help of MATLAB Simulink.

2.3. PID Control Method and Algorithm

The PID method is widely used in processes with rapid and large load changes. In PID control, the derivative and integral of the difference signal between the set value and the measured value are taken. The proportional signal, integral signal and derivative signal are collected in the adder circuit. In this way, a correction is made in manipulated variable according to Equation (3) [25, 26].

$$m(t) = K_P(t) + K_I \int_0^t e(t)d(t) + K_d \frac{de(t)}{d(t)} + V_o \qquad (3)$$

PID controller parameters need to be adjusted according to process dynamics. For adjustment, firstly the process model must be defined. Process Reaction Curve (PRC) Method was used in order to calculate the PID parameters with Cohen-Coon Method [21].

2.4. Dynamic Experiment

In general, dynamic experiments are known as laboratory-scale measurements performed under excitation conditions that change over time. Since dynamic experiments are performed under physical, economic, and device constraints, they should be applied after excellent preliminary research [18]. After deciding on the parameter to be controlled before the experiment, it should be determined how the variable will be measured. These parameters are the factors that directly form the character of the system. Within the scope of this study, two different dynamic experiments were carried out for two different parameters to be controlled. While the process output variable was defined as pH to determine the pH control, the process output variable was defined as temperature to determine the temperature control. The flow rate of the base pump and cooling water pump was changed to create a load effect (step input) on pH and temperature, respectively. The experimental setup of the PID control for pH and temperature control is given in Figure 2.

2.5. Anti-Windup

Actuators always possess both a lower and an upper limit, referred to as saturation limits. When these limits, or saturations, are reached, the dynamics of the process output tend to respond more slowly compared to instances where there's a significant set point alteration or disturbance. Consequently, in such scenarios, the integral component (I) of a PID controller experiences rapid escalation due to the gradual reduction in error caused by saturation. The control output, or actuator, becomes saturated. This occurrence is termed "integral windup" [27].

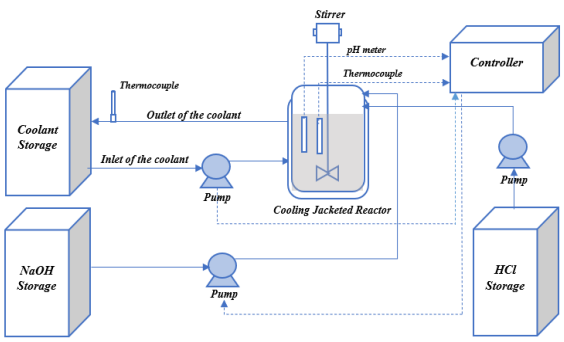

Figure 2. PID Control for the Temperature and pH

As a result of actuator saturation, the integral component, up until the rise time, becomes substantially larger than its eventual value. Consequently, a notable overshoot (i.e., a considerable negative error) becomes unavoidable in order to diminish the already accumulated integral component to the desired final integral value. In this manner, integral windup adversely affects control performance [28, 29].

Numerous techniques exist to mitigate integral windup. One of these approaches is known as "back calculation," while another is referred to as the "Conditional Integration Method." The Back Calculation Anti-windup technique employs an internal feedback loop to guide the convergence of the integral component toward the actuator's limit [18].

The Conditional Integration (CI) Anti-windup method, on the other hand, prevents integral windup by temporarily suspending the integral action when the actuator reaches its limit value[30].

3. Result and Discussion

PID controller parameters were calculated with the help of Cohen-Coon tuning method, so the transfer function of the system was determined with the help of a dynamic experiment.

3.1. Dynamic Experiment for Calculating PID Control Parameters

A dynamic experiment was carried out to determine the PID Control Parameters for the neutralization reaction. Two different dynamic experiments were carried out for two different parameters that were to be controlled. For the determination of pH control parameters, the process variable is defined as pH and manipulated variable is defined as base flow rate, while the temperature for the determination of control parameters, the process variable is defined as temperature and the manipulated variable as cooling water flow rate. To determine these parameters, the step inputs are given to manipulated variables for the dynamic analysis. Figure 3.a shows pH change with time by giving step input to base flow rate. Figure 3.b represents T change with time by giving step input to cooling water flow rate. Accordingly, since the transition from the first steady state to the second steady state was observed, it was concluded that the system has shown first order plus dead time model properties [27, 31]. In addition, a positive step effect is given to the system when the system reaches the first steady state for the purpose of determining the model parameters. This positive charge effect was achieved by increasing the base pump flow rate from 10 mL/min to 40 mL/min at 491 s. It was observed that the pH value increased from 3,1536 to 10.5176 when this effect was given to the system. Model parameters were determined by dynamic process reaction curve method. For this purpose, the "S curve" formed between 0-500 s was examined. In the area covered, the run time (τ) is 59 s, the dead time (Θ) is 261 s, and the static gain (K) is found as 14.72 ◦Cs/mL pH value/mL NaOH flow rate. After the model parameters are determined, the Cohen Coon method is applied to find the PID parameters according to the PID control algorithm. Accordingly, PID parameters calculated for pH were calculated as K_C=0.0375, τ_I=315.759 1/s, and τ_D=52.601 s using Cohen-Coon equations as shown in Table 1.

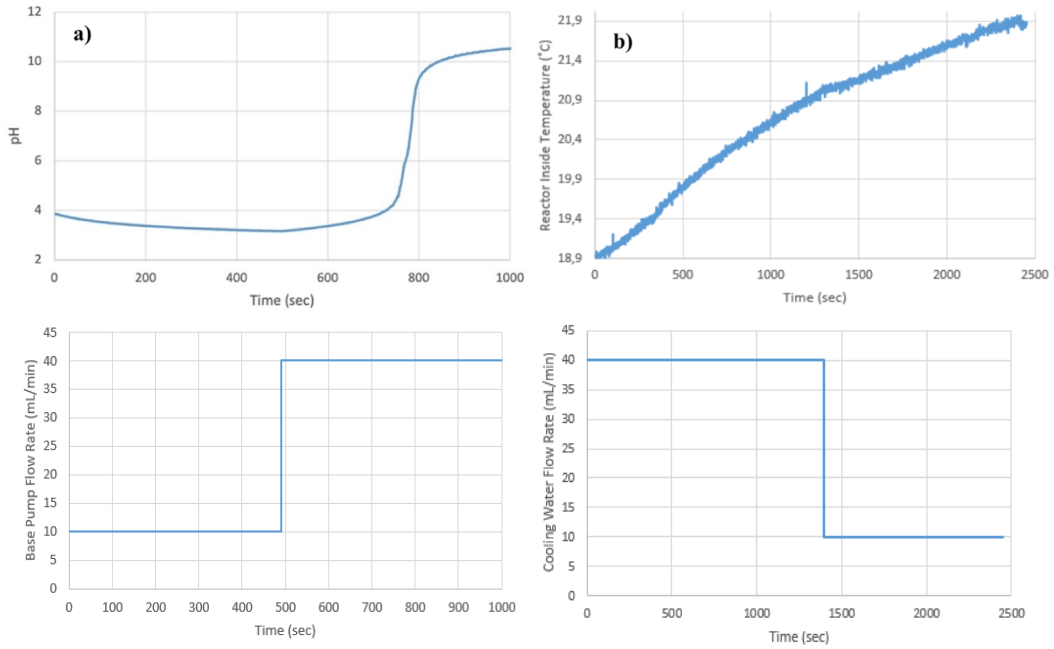

Figure 3. a) pH and base flow rate change b) T and cooling water flow rate change with time during the dynamic experiment

Table 1. Determination of PID control parameters with positive and negative step input given to controlled variables pH and T

Controller	Input	PID Parameters	Controller	Input
pH Controller with PID	Positive step input to NaOH flow rate from 10 mL/min to 40 mL/min	0.0375	315.759	52.601
T Controller with PID	Negative step input to Cooling water flow rate from 40 mL/min to 10 mL/min	6.196	47.23	-19.20

The temperature change with time is given in Figure 3.b, as pH. In addition, a negative load effect is given to the system when the system reaches the first steady state to determine the model parameters. This negative charge effect was achieved by changing the cooling water flow rate from 40 mL/min to 10 mL/min, which is given in Figure 3.b. It was observed that the temperature value increased from 18.87 ºC to 21.87 ºC when this effect was given to the system.

To investigate the model parameters for temperature, between 0-3835 s in the graph were examined. In the area covered, the time constant (τ) is 1402 s., the dead time (Θ) is 88 s, and the steady state gain (K) is found as -6 ◦C s/mL Then, PID parameters are calculated as K_C = 6.196, τ_I = 47.23 1/s, and τ_D= -19.20 s. by using Cohen-Coon equations as shown in Table 1.

3.2. Experimental PID Control of Neutralization Reaction

After the PID parameters were determined for pH, a neutralization reaction of hydrochloric acid and sodium hydroxide was performed with PID control. In the experiment performed in pH control with PID, the determined pH set point must be between 6.5-8.5 according to the water pollution control regulation [32], and pH control with PID is given in Figure 4.a, base flowrate changes with time is given in Figure 4.b and accordingly the Integral Square Error (ISE) change for pH with time is given in Figure 4.c.

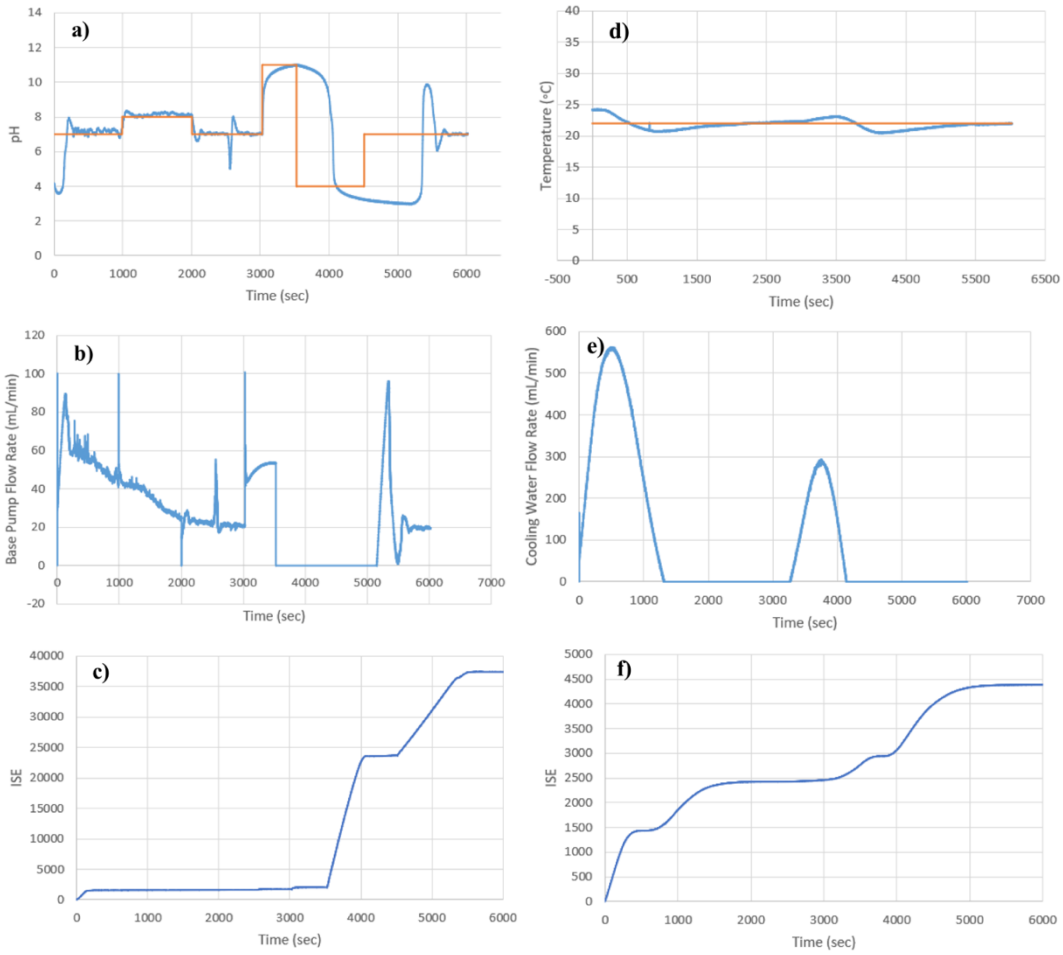

Figure 4. Experimental pH and Temperature Control with PID Control
a. pH control b. Base flow rate c. Integral Square Error (ISE) change for pH d. T control e. B flow rate f. Integral Square Error (ISE) change for T

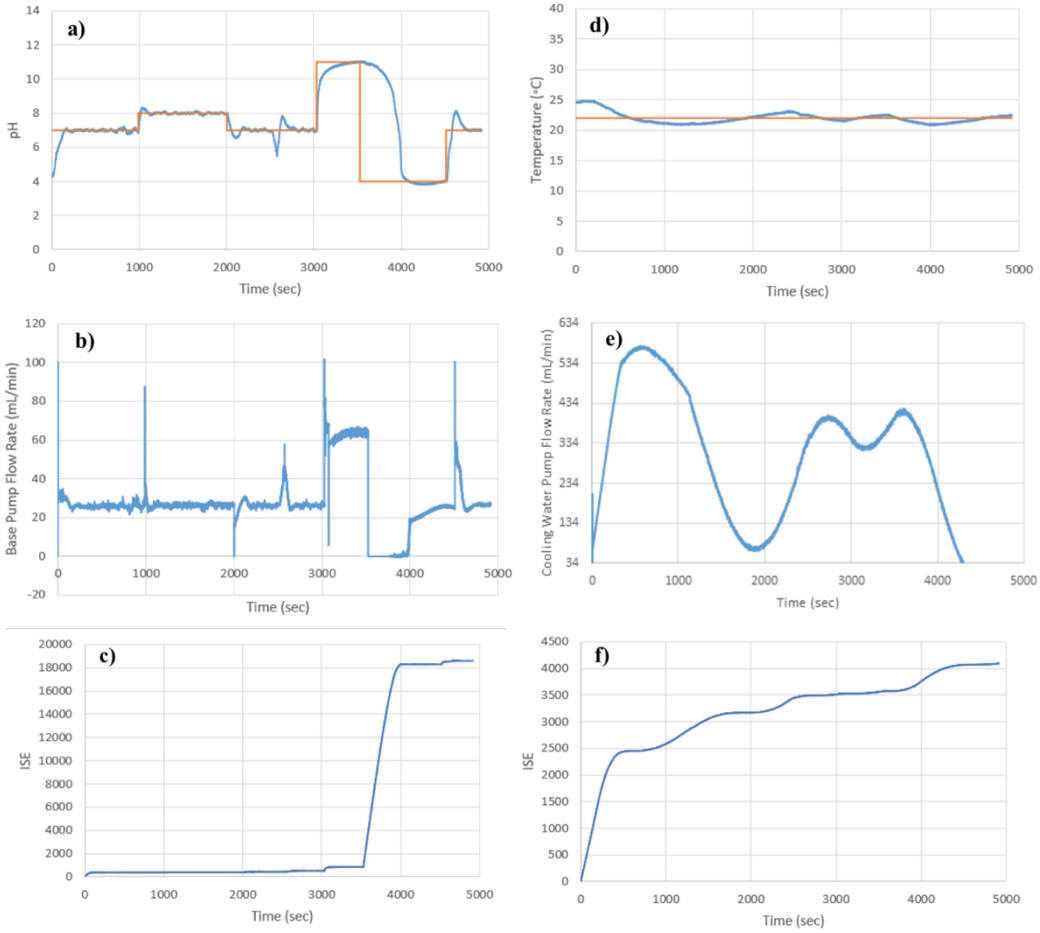

Figure 5. Experimental pH and Temperature Control with PID Control

a. pH control b. Base flow rate c. Integral Square Error (ISE) change for pH d. T control e. B flow rate f. Integral Square Error (ISE) change for T

Similarly, the PID parameters determined for the temperature were used in the neutralization reaction. Thus, temperature in the reactor changes according to time is given in Figure 4.

The flow rate of the cooling water determines the ability to keep the temperature at the desired set value. Temperature control is given in Figure 4.d. The change of cooling water flow rate with a time graph is given in Figure 4.e. Likewise, error signals are given to the cooling water pump while PID controls the temperature. Figure 4.f shows a graph of the evolution over time of the sum of the squares of the integrals of various error signals.

After the dynamic analysis, PID control parameters were calculated and coded into the controller. To observe the time-dependent variation of pH and temperature data under PID control, the flow rate of the 0.014 M HCl pump is kept constant at 0.193 mL/min, and flow rate the pH of the 0.025 M NaOH pump is changed by the flow rate controller. pH of the reaction has been tried to be kept in the range of 6.5-8.5. Considering the graphics, it has been observed that the coded set values reached after the oscillation, which is the behavior characteristic of the PID. Input variables were changed to observe the load effect. The load effect is given by increasing the acid pump flow rate from 40 mL/min to 80 mL/min at 2500 s. As a result of this effect, although a sudden increase in pH is observed, it has been observed that PID control is successful in controlling pH at the pH set point.

3.3. PID Control with Anti-windup

Anti-windup, a type of PID control, was applied for both pH parameter and temperature parameter in order to provide better control while performing PID control in the neutralization reaction. Anti-windup control is achieved by using the conditional integral (CI) method. pH change with time by ARW is given in Figure 5.

pH change with time by Anti-windup is given in Figure 5.a. While pH control was achieved with the Anti-windup method, the pH set points were changed. It has been observed that when the pH set point is lowered from 11 to 4 at 3524 s, the control with Anti-windup control provides better control than the PID control without Anti-windup. To keep the pH at set values base flow rate change with time by Anti-windup is shown in Figure 5.b. It has been observed that the sum of the integrals of the error signals decreases thanks to the PID with Anti-windup method,

which is used to ensure that integral part of PID controller output the sum of the integrals of the error signals is not above or below the maximum or minimum outputs values of the final control element. The graph of the sum of the squares of the integrals of these error signals for pH versus time is given in Figure 5.c.

Likewise, the temperature control in the reactor was carried out with the Anti-windup method. The results obtained and the variation of the temperature values in the reactor against time are given in Figure 5.d whereas, the change in the flow rate of the cooling water pump against time to keep the temperature at set value is given in Figure 5.e. Finally, the graph of the sum of the squares of the integrals of these error signals for temperature versus time is given in Figure 5.f.

The pH range of the product is 6.5-8.5 in the targeted direction, the experimental designs were made according to this purpose. With the literature search, it was observed that when NaOH and HCl reactants were taken in a 1:1 molar ratio, neutralization was achieved, and the pH value was within the predicted range. The effects of acid and base used in the neutralization process on pH, conductivity, and temperature were investigated by conducting experiments in a continuous type of reactor using constant acid/base concentrations.

4. Conclusion

In order to provide pH and temperature control in neutralization reactions with PID Control Method, PID control without Anti-windup and PID control with Anti-windup were used. PID control method with Anti-windup provides control according to the maximum and minimum working capacities of the working equipment. Based on the data, it has been observed that Anti-windup method, which provides control by adhering to the sudden changes in the nature of pH and temperature parameters in exothermic reactions, where the reaction rate is high, is much more successful in controlling the system parameters that are desired to be controlled. As a conclusion, process control steps were applied systematically to make the hydrochloric acid produced as a by-product in the industry suitable for disposal, and with the help of PID control, the pH of the product formed as a result of the reaction was successfully controlled in the range of 6.5-8.5 and its temperature at 22 °C. A better performance was obtained by using the conditional integral method as an anti-windup technique. In future studies, experiments can be performed using the back calculation method, which is another anti-windup method, and its performance can be compared.

Declaration

The author(s) declared no potential conflicts of interest with respect to the research, authorship, and/or publication of this article. The author(s) also declared that this article is original, was prepared in accordance with international publication and research ethics, and ethical committee permission or any special permission is not required.

Author Contributions

Z.Y.Hitit supervised the study. I.Kocer implemented the controller algorithm, data acquisition and methodology, G.Kus , N.Z. Arslan, E.P.Dal, H.Koz performed experiments and wrote the manuscript together.

Acknowledgment

This study was supported by the Department of Engineering of Ankara University and the Scientific and Technological Research Council of Turkey (TÜBİTAK) 2209-A University Students Research Projects Support Program with project number 1919B012005917.

References

1. Silberberg, M. , *Principles of general chemistry*. 2012, McGraw-Hill Education.
2. Ekambaram, S. . *General chemistry*. 2012, India: Pearson Education India.
3. Harris, D. C.. *Quantitative chemical analysis*. 2010, Macmillan.
4. Gomma, G. K. and Wahdan, M. H. *Schiff bases as corrosion inhibitors for aluminium in hydrochloric acid solution.* Materials chemistry and physics, 1995. **39**(3): 209–213.
5. Ebbing, D., and Gammon, S. D. . *General chemistry. 2016*, Cengage Learning.
6. Dimian, A. C., Bildea, C. S., and Kiss, A. A. *Integrated design and simulation of chemical processes*. 2014, Elsevier.
7. Shannon, M. W., Borron, S. W., Burns, M. J., Haddad, L. M., & Winchester, J. F. *Haddad and Winchester's clinical management of poisoning and drug overdose*. 2007, Saunders/Elsevier.
8. Drechsler, M., & Schmidt, H.-J. (2005). Textbooks' and teachers' understanding of acid-base models used in chemistry teaching. *Chemistry Education Research and Practice*, 2005. **6**(1): p. 19–35.
9. Levenspiel, O. Chemical Reaction Engineering. *Industrial & Engineering Chemistry Research*, **1999. 38**(11): p. 4140–4143. https://doi.org/10.1021/ie990488g
10. Petrucci, R. H., Herring, F. G., & Madura, J. D. *General chemistry: principles and modern applications*. 2010, Pearson Prentice Hall.
11. Raymond, C., & Jason, O. *General chemistry-The Essenstial Concepts*. 2008, McGraw-Hill.
12. Sadler, G. D., & Murphy, P. A. pH and titratable acidity. *Food analysis*, 2010. **4**: p.219–238.

13. Suresh, S., and Sundaramoorthy, S. *Green Chemical Engineering*. 2015, Boca Raton: CRC Press.
14. Avery, H. E. *Basic reaction kinetics and mechanisms*. 1974, Macmillan International Higher Education.
15. Nazım, İ.. Su Şebeke Otomasyon Sistemi ve Uygulaması. *Bilecik Şeyh Edebali Üniversitesi Fen Bilimleri Dergisi*, 2020. **7**:p. 353–362.
16. Küçük, H. Otomasyon yönetiminde insan faktörü ve Türk otomotiv sektöründe bir uygulama. Fen Bilimleri Enstitüsü. 1995, Istanbul Technical University: Turkey.
17. Luyben, W. L. *Chemical reactor design and control*. 2007, John Wiley & Sons.
18. Visioli, A. *Practical PID control*. 2006, Springer Science & Business Media.
19. Sung, S. W., Lee, J., & Lee, I. B. *Process Identification and PID Control. Process Identification and PID Control*. 2009, John Wiley & Sons.
20. Green, D. W. and Southard, M. Z. *Perry's Chemical Engineers' Handbook. New York. 2019, USA: McGraw-Hill Education*.
21. Seborg, D. E., Edgar, T. F., Mellichamp, D. A. and Doyle III, F. J. *Process dynamics and control*. 2016, John Wiley & Sons.
22. Aldemir, A., & Anwer, M. S. Determination of optimal PID control parameters by response surface methodology. *International Advanced Researches and Engineering Journal*, 2020. **4**(2): 142–153.
23. Bleicher, F., Biermann, D., Drossel, W.-G., Moehring, H.-C., & Altintas, Y. Sensor and actuator integrated tooling systems. 2023, *CIRP Annals*.
24. Zarrop, M. B. *Optimal experiment design for dynamic system identification*. 1979, Springer.
25. Bera, S. C., Mandal, N., & Sarkar, R. An accurate technique of measurement of a transducer output by using a modified two core saturable reactor. *Measurement*, 2009. **42**(8):p. 1233–1240.
26. Stanelytė, D., & Radziukynas, V. Analysis of voltage and reactive power algorithms in low voltage networks. *Energies*, 2022. **15**(5): 1843.
27. Liptak, B. G. *Process Control and Optimization. Instrument Engineers' Handbook, Volume II.* 2006, CRC Press.
28. Elguindy, A. Drum-boiler control performance optimization using an observer-based state-feedback controller within MATLAB/Simulink environment. 2013, *Bremen University*.
29. Wen, S.-X., Pan, Z.-R., Liu, K.-Z., & Sun, X.-M. Practical anti-windup for open-loop stable systems under magnitude and rate constraints: Application to turbofan engines. *IEEE Transactions on Industrial Electronics*, 2022. **70**(4): p. 4128–4137.
30. Walgama, K. S., & Sternby, J. Inherent observer property in a class of anti-windup compensators. *International Journal of Control*, 1990. **52**(3): p. 705–724.
31. Muresan, C. I., Birs, I., Ionescu, C., Dulf, E. H., & De Keyser, R. A review of recent developments in autotuning methods for fractional-order controllers. *Fractal and Fractional*, 2022. **6**(1): 37.
32. Gazette, O. Turkish State Water Pollution Control Regulation, 4 Sept. 1988, Number: 19919, Ankara. Turkish.

Available online at www.dergipark.org.tr/en

INTERNATIONAL ADVANCED RESEARCHES and ENGINEERING JOURNAL

Journal homepage: www.dergipark.org.tr/en/pub/iarej

e-ISSN: 2618-575X

International Open Access

Volume 07
Issue 03

December, 2023

Research Article

Investigation of mechanical properties and thermal conductivity coefficients of 3D printer materials

Furkan Parmaksız [a], ***Nergizhan Anaç*** [a], ***Oğuz Koçar*** [a,*] ***and Beytullah Erdoğan*** [a]

[a]*Department of Mechanical Engineering, Bülent Ecevit University, İncivez, Zonguldak, 67030, Türkiye*

ARTICLE INFO

Article history:
Received 27 May 2023
Accepted 04 October 2023
Published 15 December 2023

Keywords:
Filament material
Fused deposition modeling (FDM)
Mechanical properties
Thermal conductivity coefficient

ABSTRACT

The demand for 3D printer technology and products, one of the additive manufacturing methods, is increasing daily in the sectoral and academic fields. Many types of polymer-based filaments are used in 3D printers, pure or filled/reinforcement. Utilizing these specialized materials in places suitable for their mechanical and thermal properties will help efficiently use resources. Using 3D printers, it is possible to manufacture products that provide thermal insulation or good heat conduction in heating and cooling areas. Especially due to the energy requirements for heating and cooling, it is very important to know the thermal performance of materials to ensure and maintain energy efficiency. This study experimentally investigated the mechanical properties and heat conduction coefficients of 3D printed parts. The experiments were conducted with seven different filament materials (PLA, PLA+, PLA-CF, PLA Wood, Tough PLA, ABS+, TPU) and three layer thicknesses (0.1, 0.2, and 0.3 mm). Samples for tensile testing, hardness, and thermal conductivity coefficient measurements were produced, and measurements were performed. In the experiments, the highest tensile strength was obtained in PLA-CF with 0.3 mm layer thickness, and the lowest tensile strength was obtained in PLA Wood with 0.3 mm layer thickness. Tensile strength decreased with an increasing layer thickness in PLA, PLA Wood, ABS+, and TPU, while it increased in PLA-CF. The highest tensile strength of PLA+ was determined to be 0.2 mm and 0.1 mm layer thickness in Tough PLA. Hardness results showed minimal change in hardness values with increasing layer thickness. The thermal conductivity values of the samples varied according to the additives and layer thicknesses. The highest thermal conductivity increase was measured in PLA-CF with 11.84%, and the lowest thermal conductivity decrease was measured in Tough PLA with 9.44%.

1. Introduction

From the 1950s to 2022, global plastic production witnessed a significant surge, escalating from 1.5 million tons to a staggering 390 million tons [1]. The use of plastic cannot be abandoned due to reasons such as cost and weight advantages and easy processing [2]. Most plastic materials are petroleum-based, and those that can be recycled can be reused. However, waste management of plastics that are not biodegradable or cannot undergo recycling processes is not easy. Plastic waste poses a significant environmental problem for both water sources and natural habitats [2]. In recent years, with the growing environmental and economic concerns, the production and consumption of biodegradable materials called bioplastics, which are based on bio-based polymers and can be recycled, have been supported [3, 4]. Currently, there are various biobased materials developed, and the most popular one is polylactic acid (PLA) [5]. The use of PLA as a filament material in additive manufacturing methods (such as 3D printers) is one of the primary drivers behind its increased consumption.

Additive manufacturing is a production process in which any model designed in accordance with the production method is transformed into a physical part by being sequentially layered and fused. With additive manufacturing method, complex and multi-material parts that are difficult to produce using traditional methods can be produced. Due to its advantages, additive manufacturing is utilized in various fields such as aviation and space, automotive, architecture, and healthcare. The

* Corresponding author. Tel.: *+90-372-291-11-81*; Fax: +90-372-291-18-00.
E-mail addresses: parmaksizfurkan67@gmail.com (*F. Parmaksız*) ,nergizhan.kavak@beun.edu.tr *(N. Anaç)*, oguz.kocar@yahoo.com.tr *(O. Koçar)*, beytullaherdogan@hotmail.com, (*B. Erdoğan*).
ORCID: 0000-0001-7002-9157 *(F. Parmaksız)*, 0000-0001-6738-9741 *(N. Anaç)*, 0000-0002-1928-4301 *(O. Koçar)*, 0000-0002-6120-9196 *(B. Erdoğan)*
DOI: 10.35860/iarej.1303538

method is continuously evolving, and its applications are expanding over time.

The most widely used additive manufacturing method is 3D printing, which operates with the FDM (Fused Deposition Modeling) technology. Despite having a limited number of material options compared to traditional production techniques, 3D printers are present in almost every industry. 3D printers have played an important role in the popularity of the method as they are the choice of both industrial manufacturers and home users. With this method, it is possible to produce personalized products rapidly and at a low cost. In the simplest terms, 3D printers work according to the principle of melting thermoplastic material and layering it on a platform to build the final product [6, 7]. The consumables, known as filaments, are produced from a wide range of thermoplastics. PLA, ABS (Acrylonitrile Butadiene Styrene), PETG (Polyethylene terephthalate glycol), ASA (Acrylonitrile styrene acrylate), and their derivatives are commonly used in 3D printers. The surface quality of the final products manufactured through additive manufacturing should be good. While a good surface quality is expected, the product must also be robust and durable [8]. Since the mechanical properties of the produced items, such as strength and hardness, are primarily determined by the chosen thermoplastic filaments, the selection of the appropriate material and printing parameters is crucial [9].

The low thermal conductivity of polymers can be attributed to several factors, including their low atomic densities, weak chemical bonds, and complex crystal structures, which result in intricate molecular vibrations. [10]. In addition, they are preferred as insulation materials because they have low thermal conductivity properties [11]. For this reason, the thermal conductivity properties of polymers are improved with carbon, ceramic and metallic fillers [12, 13]. The low thermal conductivity of polymers can lead to thermal fatigue. Additives, various metal powders and fibers (fiberglass, carbon fiber) are added to polymer materials to reduce thermal fatigue [11, 13]. Polymer materials also have low electrical conductivity. Most polymer materials possess electrical insulation properties. For this reason, they are used as insulating materials in the electrical and electronic industry. However, the electrical conductivity can be increased by adding conductive additives to polymer materials.

The thermal conductivity of a material indicates its energy storage capacity and its ability to withstand extreme heat [14]. Many researchers have examined the thermal conductivity properties of 3D printer materials at different temperatures by adding different additives (nanoparticle, composite, polymer, wood, etc.) in various amounts to 3D printer materials. In most of the filaments obtained in these studies, a significant increase (up to 80%) was obtained in thermal conductivity, while some exhibited (up to 25%) decreases [15-20]. In the literature, there is a lot of of studies that examine the impact of various 3D printing parameters on the mechanical properties of filaments. These parameters include bed and nozzle temperature, printing speed, orientation angle, infill density, and more. Researchers have extensively investigated these factors to understand their influence on the final mechanical characteristics of printed objects. Nevertheless, there exists an insufficiency of investigations regarding the influence of material characteristics and printing variables on alterations in thermal conduction. Yet, thermal conductivity plays an important role in the selection of 3D printers and their filament, which have a wide range of applications. To improve the applicability of polymer materials in cooling or heating applications, it becomes imperative to comprehend the thermal conductivity characteristics of filaments and enhance them when necessary, through the incorporation of suitable fillers [21-23]. With this aim, the relationship between the mechanical and thermal conductivity properties of different filament materials used in 3D printing and the layer thicknesses has been investigated in this study. The thermal conductivity, hardness, and tensile tests were conducted on materials produced with different layer thicknesses to evaluate their material properties. In this study, unlike the literature, the mechanical properties and thermal conductivity properties of eight different filaments, which are most commonly used in 3D printing, were investigated and the changes depending on the layer thickness were revealed. This study also emphasized the importance of filament selection according to the conditions of use.

2. Material and Methods

2.1. Material

In this study, seven different thermoplastic filament materials were used, namely PLA, PLA+, carbon fiber-reinforced PLA (PLA-CF), wood-filled PLA (PLA Wood), Tough PLA, ABS+, and TPU (Thermoplastic Polyurethane). PLA is the most commonly used filament material in 3D printers. PLA, a thermoplastic derived from organic sources like corn starch and sugar cane, boasts several advantages such as being non-toxic, biodegradable, and harmless to human health. In addition to these benefits, PLA offers ease of production and excellent printing capabilities [25, 26]. The PLA-enhanced filaments used in this study are variations that enhance the mechanical properties of standard PLA. PLA+ and Tough PLA materials exhibit higher toughness and impact resistance compared to standard PLA filaments while showing less hygroscopic behavior [24]. PLA Wood filaments are composite PLA with 30% (by weight) wood content. Wood is a biodegradable material. Small pieces of

wood are ground into smaller pieces to obtain fine wood flour. Fine wood particles can be used as a filler material for filaments [25]. PLA Wood filaments have higher temperature resistance, unclear layer lines and a matte wood appearance with the addition of real wood [26]. PLA-CF filament is a PLA composite filament reinforced with 15% (by weight) carbon fiber. Carbon fiber (CF) produced from natural plants and resources is lightweight, biodegradable, and biocompatible. Natural fibers can enhance the crystallization and improve the mechanical and thermal properties of PLA. PLA-CF filaments exhibit lower tensile and bending properties, dimensional stability, lightness, and ease of printing [27, 28]. ABS+ filament material is a petroleum-based thermoplastic with high strength, hardness, and toughness [29]. TPU filaments, on the other hand, are elastic filaments with high durability, toughness, wear resistance, and good chemical resistance. TPU is classified as a copolymer because of its two-phase microstructure, which comprises both hard and soft segments. This unique composition gives TPU its distinctive properties and makes it suitable for a wide range of applications [30]. The properties of the filaments used in the experiments are provided in Table 1.

2.2. Preparation of Samples

In the study, filament with a diameter of 2.85 mm (PLA, Tough PLA, ABS+) was printed using the Ultimaker S5 printer, while filament with a diameter of 1.75 mm (PLA+, PLA-CF, PLA Wood, and TPU) was printed using the Ender 3 S1 printer. The printers used in the printing process are shown in Figure 1. The produced samples had a 100% infill ratio, and the layer thicknesses were determined as 0.1 mm, 0.2 mm, and 0.3 mm. Decreasing the layer thickness improves dimensional accuracy [39] and surface roughness. However, the length of the manufacturing process varies inversely with the layer thickness. In the experiments, the layer thicknesses were determined based on the information presented in the literature. Figure 2 provides a schematic representation of the used layer thicknesses.

Table 1. Technical properties of filament materials.

Characteristic	PLA [31]	PLA+ [32]	PLA-CF [33]	PLA Wood [34]	Tough PLA [24]	ABS+ [35]	TPU 92A [36]
Diameter (mm)	2.85	1.75	1.75	1.75	2.85	2.85	1.75
Brand	Ultimaker	eSUN	Filameon	Filameon	Ultimaker	eSUN	SAVA
Color	Black	Black	Black	Light Brown	Black	Green	Light Blue
Tensile Strength	52.5	63	55	47	45.3	40	-
Elongation (Break %)	7.8	20	-	-	9.4	30	600
Density (g/cm^3)	1.24	1.23	1.23	1.13	1.22	1.06	1.20

Figure 1. 3D printers (a) Ultimaker S5 and (b) Ender 3S1

Table 2. Printing materials.

Material	PLA	PLA+	PLA-CF	PLA Wood	Tough PLA	ABS+	TPU 92A
Infill Density (%)	100	100	100	100	100	100	100
Printing Temperature (°C)	200	210	215	220	210	250	235
Build Plate Temperature (°C)	60	60	65	65	60	110	55
Print Speed (mm/sec)	60	60	45	50	45	50	30

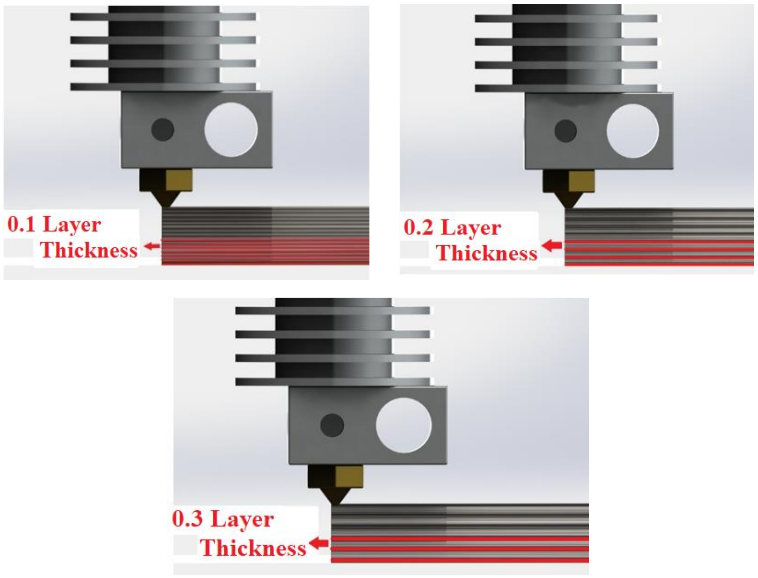

Figure 2. Change of layer thickness applied in 3D printer

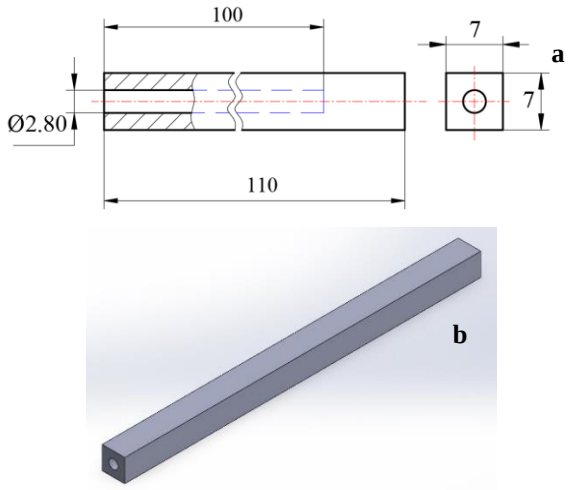

Figure 3. Thermal conductivity measurement samples a) Technical drawing (mm) b) Solid model

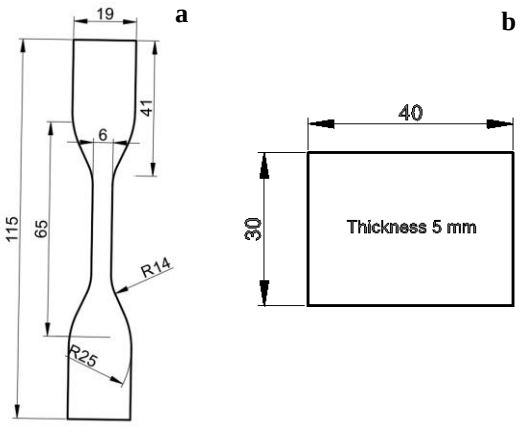

Figure 4. Sample dimensions (mm) for tensile specimen (a) and hardness measurement (b)

The three-dimensional models of the samples used for thermal conductivity measurement were created using the Fusion 360 modeling program. The subsequent step involved the slicing process, which was conducted using the Cura 5.2.1 program. Finally, the production process was completed using the FDM (Fused Deposition Modeling) method.

The parameters required to produce parts using 3D printers are given in Table 2. The technical drawing and solid model of the samples prepared for thermal conductivity measurement are provided in Figure 3. The samples were printed without supports, with 100% infill, and in the horizontal printing orientation (printing direction along the thickness/horizontal growth direction).

2.3. Tensile test and hardness measurements

Tensile samples (Figure 4 a) were printed with 0.1 mm, 0.2 mm, and 0.3 mm layer thicknesses at 100% infill ratios in order to determine the mechanical properties of PLA, PLA+, PLA-CF, PLA Wood, Tough PLA, ABS+, and TPU according to ASTM D638-10 [40] standards. Tensile tests were conducted at room temperature using a WDW-5 model universal testing machine with a 5 kN capacity at a crosshead speed of 1 mm/min. The Durometer (Shore) hardness measurement method was used for hardness measurements of the plastic materials. Durometer hardness measurements, which evaluate the material's resistance to indentation, are widely used in evaluating the mechanical properties of polymers [41]. ASTM D2240-15 standard was followed by using LOYKA D-type shore hardness durometer to perform the hardness tests.

Hardness measurement samples were prepared in different layer thicknesses of 5x30x40 mm for each filament material (Figure 4 b). Measurements were repeated at five different points for each sample and the averages were taken. Additionally, the surfaces of the printed parts were examined using a digital microscope, and the damage types were evaluated by taking the images of the rupture surfaces after the tensile test.

2.4. Thermal conductivity coefficient measurement

The coefficient of thermal conductivity is the rate of heat transfer from a unit area through a unit thickness of a material at a unit temperature. A high thermal conductivity value indicates that the material conducts heat well. Materials with low thermal conductivity are called insulators. The thermal conductivity of solid materials is measured using the Decagon/KD2 Pro [42] device with a TR-1 sensor (2.4 mm diameter x 100 mm length) operating based on the transient hot wire method. The KD2 Pro thermal conductivity measurement device and TR-1 sensor are shown in Figure 5. The operating temperature range of the TR-1 sensor used for determining the thermal conductivity value of filament materials is -50 to +150 °C, a measurement time is 5 minutes per sample, and a measurement range is between 0.10 to 4.00 W/mK [43]. The thermal conductivity measurements of PLA, PLA+, PLA-CF, PLA Wood, Tough PLA, ABS+, and TPU filaments used in different layer thicknesses (0.1, 0.2 and 0.3 mm) were repeated at least 5 times for each sample. The average thermal conductivity and temperature values are provided in Table 3. It was observed that the measured thermal conductivity values measured from the experimental samples with different layer thicknesses varied between 0.082 and 0.113 W/mK.

Figure 5. Thermal conductivity measurement device

Table 3. Thermal conductivity and Temperature Values Measured from Samples.

Material	Layer Thickness (mm)	Thermal Conductivity (W/mK)	Temp. (°C)
PLA	0.1	0.096	23.12
	0.2	0.098	25.27
	0.3	0.099	24.69
PLA +	0.1	0.094	23.12
	0.2	0.096	25.57
	0.3	0.096	25.20
PLA-CF	0.1	0.095	22.96
	0.2	0.102	24.84
	0.3	0.106	26.12
PLA Wood	0.1	0.091	21.24
	0.2	0.094	22.21
	0.3	0.101	25.77
Tough-PLA	0.1	0.090	23.22
	0.2	0.090	23.67
	0.3	0.082	23.42
ABS +	0.1	0.085	24.24
	0.2	0.091	24.98
	0.3	0.087	24.81
TPU	0.1	0.104	24.65
	0.2	0.108	25.64
	0.3	0.113	24.80

3. Result and Discussion

There are many variables that affect the strength in the design and production process of parts manufactured using the EYM method. Some of these variables are called 3D printer printing parameters, including printing temperature, printing speed, layer thickness, infill pattern, part orientation angle, and infill ratio [44]. Additionally, it is known that the addition of fillers to filaments significantly affects the strength, toughness, and elongation. Therefore, in the literature, different mechanical properties can be observed for the same material due to the use of different variables in printing [45].

3.1. Tensile test and evaluation of hardness values

In ± this study, the highest tensile strength (56.26 ± 2.6 MPa) was obtained in PLA-CF with 0.3 layer thickness, and the lowest tensile strength (26.31 ± 1.3 MPa) was obtained in PLA Wood with 0.3 mm layer thickness. It can be observed that the strength value decreases with an increase in layer thickness for PLA, PLA Wood, ABS+, and TPU (Figure 6). This result is consistent with the literature [28, 46, 47]. The highest tensile strength (49.31 ± 2.95 MPa) was obtained in PLA+ with a layer thickness of 0.2 mm. Similarly, Tymrak et al. achieved the highest tensile values at a layer thickness of 0.2 mm and a production angle of 45/-45 in their study on ABS and PLA

filament materials using three different layer thicknesses (0.2,1, 0.2 and 0.3 mm) and two different production angles [48]. While the highest tensile strength (55.11 3.8 MPa) for Tough PLA was obtained at a layer thickness of 0.1 mm, it was observed that the strength decreased at 0.2 mm layer thickness and increased slightly at 0.3 mm layer thickness. According to this result, it can be understood that the parts to be produced with Tough PLA and a layer thickness of 0.1 mm will have higher strength. It has been determined that the mechanical properties will change with the addition of filler material into the filament. It is seen that the tensile strength of PLA-CF increases with the increase of the layer thickness. On the other hand, in PLA Wood, although the increase in layer thickness decreases the tensile strength, the tensile strength has decreased significantly when compared to PLA. The low strength observed in PLA Wood can be attributed to high porosity, adhesion defects between layers, and irregularities in the print diameter due to the wood additive [49].

The filaments used in the experiments were selected from among the materials that are highly demanded in the 3D printing industry and user forums. Due to the difficulty of accessing some filament materials from the same manufacturer and manufacturers producing in the diameters they determine, the printing processes of the samples were carried out using two different printers. Therefore, it was accepted at the beginning of the study that there might be some differences due to the use of different printers and brands.

The rupture surface images of the samples printed in the horizontal growth direction after the tensile test are given in Figure 7. The fracture behaviour of PLA+, PLA-CF, PLA Wood, Tough PLA and TPU was in zigzag pattern. This is due to the internal structure where the layer lines create either parallel and 45° angles or 45° and -45° angles with the applied tensile load. The flat and sharp form of rupture of PLA and ABS+ tensile samples suggests that the tensile load follows the angle of the lines forming the structure of the samples [50].

After the tensile test, it was observed that the PLA-CF samples had thin, wire-like extensions at the fracture ends. These extensions are believed to be the carbon fiber additives present in the filament. In contrast, although PLA Wood is an additive-based filament, a similar situation did not occur at the fracture end. Unlike the carbon fiber in PLA-CF, the wood additives in PLA Wood filament have thin and small powder-like dimensions. The unit strain of the tensile specimens were found to be 2.73% ± 0.13 for PLA, 7.23% ±0.36 for PLA+, 4.67% ±0.23 for PLA-CF, 1.8% ±0.1 for PLA Wood, 3.27% ±0.16 for Tough PLA, and 3% 0.15 for ABS+. While the unit strain values for these samples ranged from 1.8% to 7.23%, the TPU rod showed significantly greater elongation due to the flexibility of the material, with a value of 567.5% ±11.35.

When examining the hardness results, it can be observed that there is minimal change in hardness with increasing layer thickness (Figure 8). The highest hardness values were obtained in PLA-CF (due to the carbon fiber additive), while the lowest hardness values were found in TPU. The hardness of TPU materials can vary depending on their chemical composition. The second lowest hardness value was measured in PLA Wood parts. The low hardness value of PLA Wood can be attributed to its high porosity and uneven gaps between layers caused by the presence of wood particles. In the case of ABS+, it can be seen that the hardness value is not significantly affected by the layer thickness. This is believed to be due to the high printing temperature of ABS+, which allows for better interlayer fusion and adhesion (Figure 9).

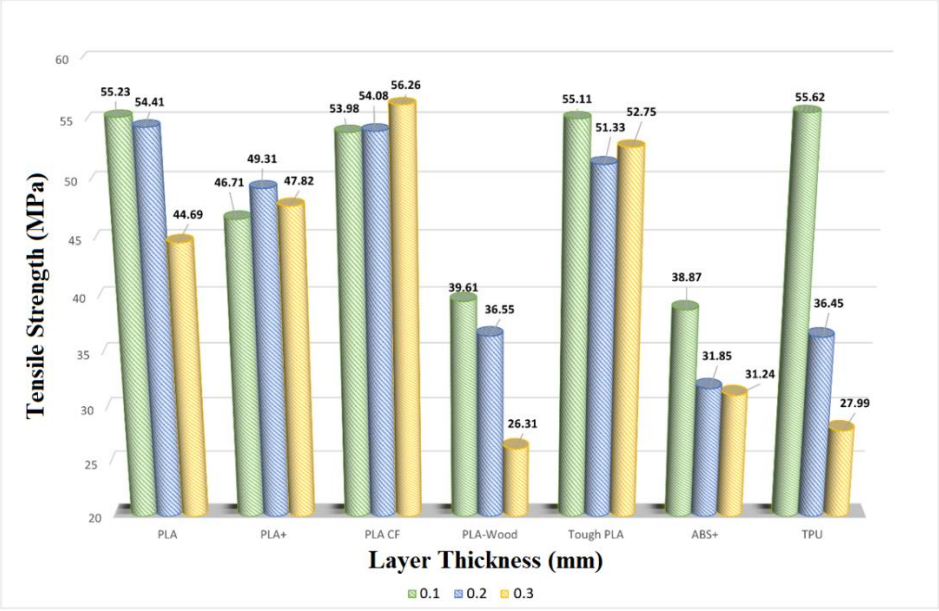

Figure 6. Change of tensile strength with layer thickness

Figure 7. Image of the sample with a 0.1 mm layer thickness after tensile testing

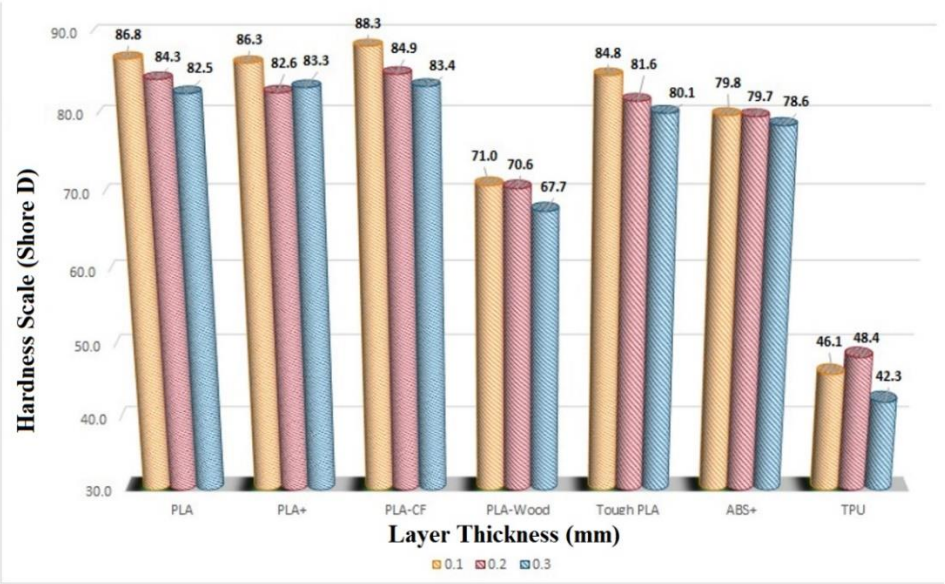

Figure 8. Change of hardness values depending on layer thickness

3.2. Evaluation of optical microscope images

The surface images of PLA, PLA+, PLA-CF, PLA Wood, Tough PLA, ABS+, and TPU materials with 0.1, 0.2 and 0.3 mm layer thicknesses are given in Figure 9 and Figure 10. The layer thicknesses and the number of layers are clearly visible in PLA, PLA+, Tough PLA, and TPU. In these materials, 12, 6 and 4 layers were placed in the same unit area for 0.1, 0.2 and 0.3 mm layer thicknesses, respectively (Figure 9). In ABS+, it can be observed that the transitions between layers become less visible, and the layers merge better.

In PLA-CF and PLA Wood, on the other hand, the presence of carbon fiber and wood additives within the filament leads to a discontinuity in the layers. Therefore, surface images were taken again using a digital microscope (Figure 10). When the surface images are examined, it is seen that the additive materials change the appearance of PLA. It has been determined that the carbon fiber additive does not significantly affect the printing process, and a linear and smooth printing is obtained during the 3D printing process. In PLA Wood, on the other hand, during the 3D printing process, dimensional differences and burning marks resulting from the wood additives are seen. Therefore, it can be said that the fusion between the layers is insufficient compared to PLA. Surface views of PLA-CF and PLA Wood samples are given in Figure 10.

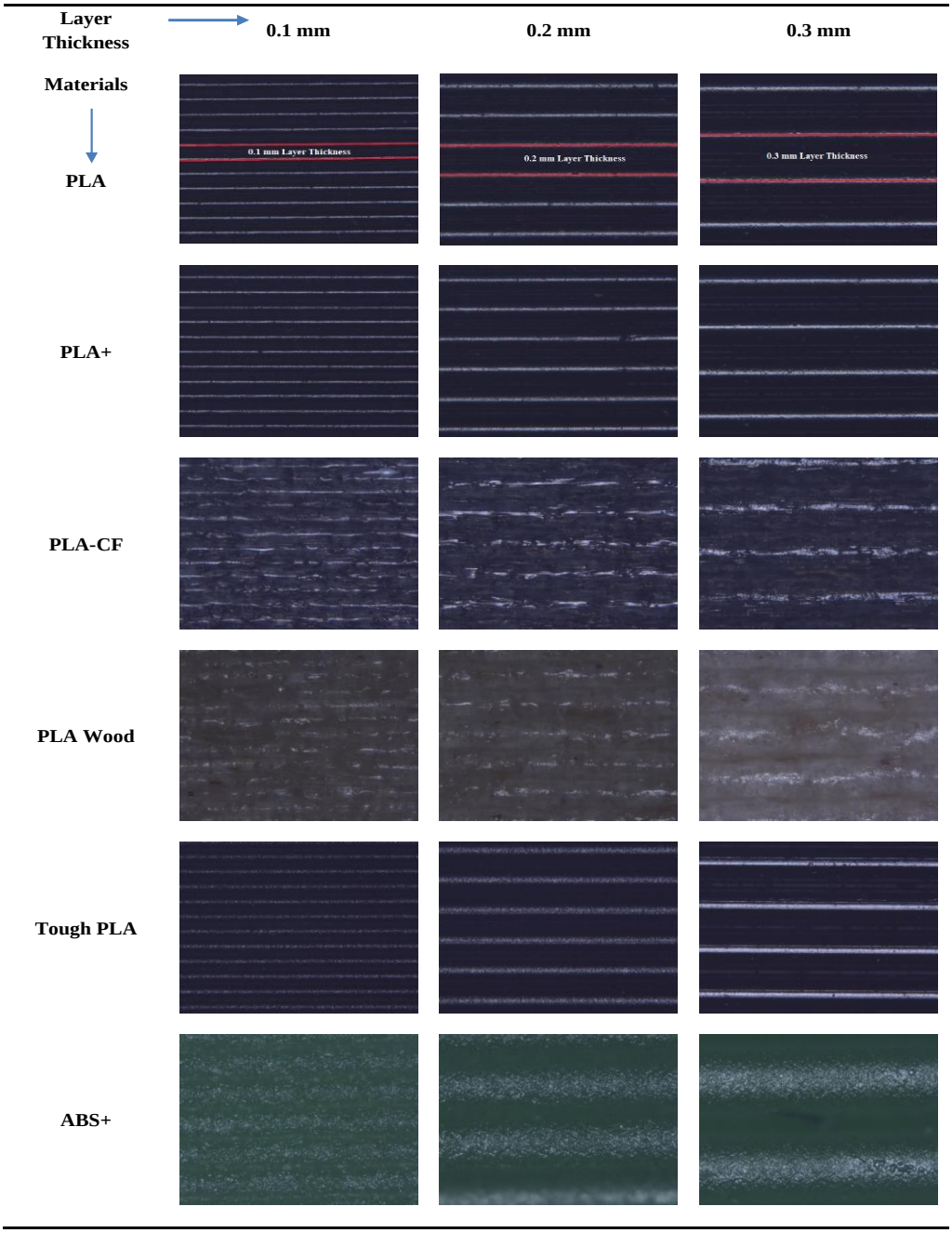

Figure 9. Surface images with an optical microscope (50x)

3.3. Evaluation of thermal conductivity coefficient measurement

The thermal conductivity values of the parts produced in 3D printers from PLA, PLA+, PLA-CF, PLA Wood, Tough PLA, ABS+ and TPU filaments with different layer thicknesses (0.1, 0.2 and 0.3 mm) were measured. The variation between the measured thermal conductivity values and the layer thicknesses is given in Figure 11. It was observed that the thermal conductivity of TPU, PLA-CF, and PLA Wood increased with the increasing layer thickness. In contrast, Tough PLA showed no significant change in thermal conductivity when layer thickness was changed from 0.1 mm to 0.2 mm. However, a noticeable decrease in thermal conductivity was observed with a layer thickness of 0.3 mm. ABS+, PLA+, and PLA materials, on the other hand, exhibited little change in thermal conductivity with increasing thickness. PLA-CF, PLA Wood, TPU, and Tough PLA filaments showed a maximum increase of 11.84%, 11.33%, and 8.65% in thermal conductivity, respectively, with increasing layer thickness, while Tough PLA showed a decrease of 9.44%. It was observed that the thermal conductivity properties were improved due to the additives added to PLA-CF and PLA Wood filaments, and the two-phase structure of TPU. The thermal conductivity properties of PLA-CF and PLA Wood improved due to the additives in the filaments, while the thermal conductivity of TPU improved due to its two-phase structure.

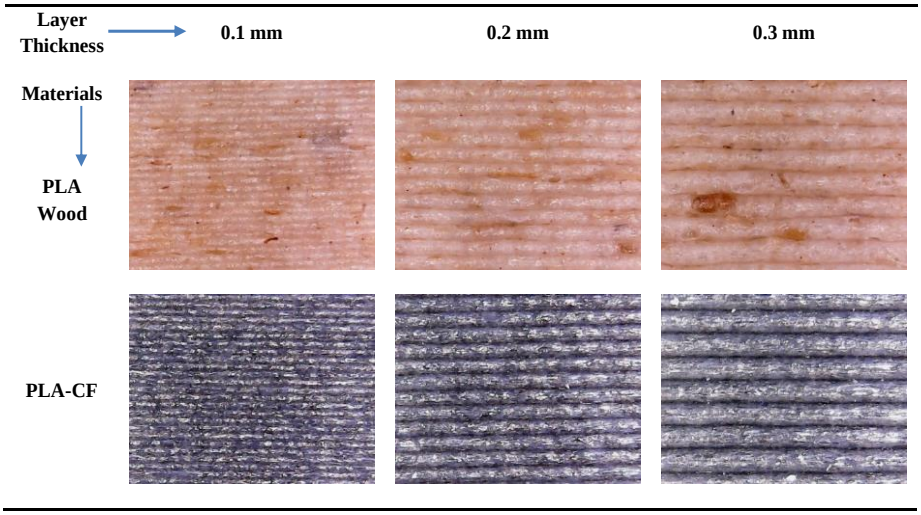

Figure 10. Surface images of PLA-CF and PLA Wood with a digital microscope (100x)

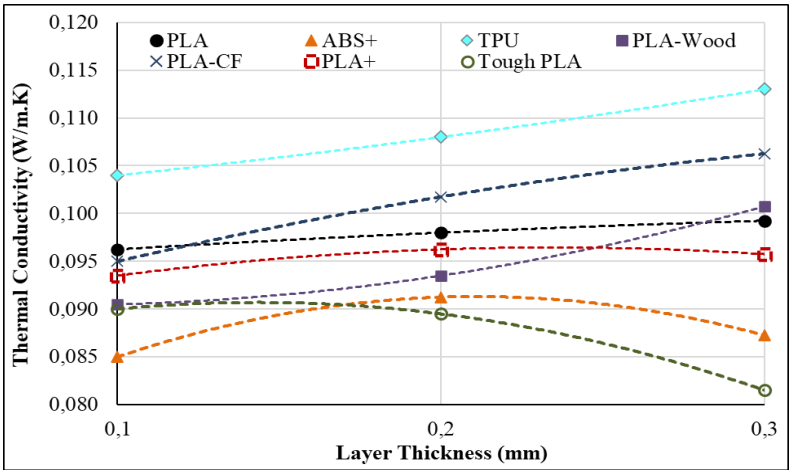

Figure 11. Change of thermal conductivity depending on layer thickness.

In PLA-CF and PLA Wood, the thermal conductivity decreased in parts with a layer thickness of 0.1 mm due to the higher number of layers per unit. The reason for this is that as the number of layers increases, the number of gaps and irregularities between the layers increases. PLA-CF, PLA Wood and TPU materials can be used in cooling and heating systems because of their good heat transfer capacity compared to other test materials. It has been observed that the layer thickness of these filament materials directly affects the thermal conductivity property. Therefore, layer thickness and selection of appropriate filament materials play an important role for 3D printed materials to be used in heating and cooling systems. Materials produced from other filament types (PLA, PLA+, Tough PLA, ABS+) can be considered as insulation materials.

4. Conclusion

The rapid development of technology has affected both user demands and production techniques. 3D printers have emerged as innovative technologies and tools that can meet the needs of many different sectors, ranging from the furniture industry to food production. This technology has been expanding its market share in the manufacturing field day by day due to the increasing variety of filament materials, which are the raw input, and the growing number of products produced with them. Therefore, it is necessary to have knowledge about the mechanical and thermal properties of the parts produced with 3D printers.

In this study, the effects of different layer thicknesses and filament materials on the mechanical and thermal conductivity properties of printed parts were examined. The results obtained are summarized below:

- The highest tensile strength of 56.25 MPa was obtained in PLA-CF with a layer thickness of 0.3 mm. The lowest tensile strength of 26.31 MPa was obtained in PLA Wood with a layer thickness of 0.3 mm. It was observed that the tensile strengths obtained in the PLA types with additives varied depending on the strength of the additive material. In PLA, PLA Wood, ABS+, and TPU, the tensile

strength decreased as the layer thickness increased. In PLA-CF, on the other hand, the tensile strength increased with an increase in layer thickness.

- In PLA+ and Tough PLA, it was observed that the tensile strength did not show a clear change depending on the layer thickness.
- When the hardness results are examined, it is seen that the hardness values change very little depending on the layer thickness and the hardness value is inversely proportional to the increase in layer thicknesses. Among the six different filament materials used in the experiments, the highest hardness values were observed in the 0.1 mm layer thickness, with the exception of TPU material, which showed the highest hardness value at 0.2 mm layer thickness.
- When the surfaces of the 3D parts were examined, it was seen that the layers bonded well, especially at low layer thicknesses, due to the use of high nozzle and bed temperature to produce ABS+ samples. In PLA Wood, it was determined that high porosity and interlayer adhesion defects increased with the increase of layer thickness. On the other hand, in PLA, PLA+, Tough PLA and TPU, the layers were stacked smoothly, with a distinct and gapless structure.
- When the measured thermal conductivity values are examined, it is seen that the additive materials and layer thicknesses in the filament are significant factors. Except for Tough PLA material, as the layer thickness increased, the thermal conductivity values increased. PLA Wood, TPU and PLA-CF showed better energy storage capacity and heat resistance at lower layer thicknesses.
- It can be said that PLA-CF, PLA Wood and TPU materials, which have an increase in thermal conductivity value as the layer thickness increases, have good thermal conductivity. It can be said that other materials with constant or decreasing thermal conductivity as the layer thickness increases can be preferred as insulating materials

Declaration

The authors declared no potential conflicts of interest with respect to the research, authorship, and/or publication of this article. The authors also declared that this article is original, was prepared in accordance with international publication and research ethics, and ethical committee permission or any special permission is not required.

Author Contributions

Conceptualization, O.K. and N.A.; methodology, O.K. and B.E.; investigation, F.P. and N.A.; data curation, N.A. and F.P; writing—original draft preparation, F.P., O.K., N.A. and B.E.; writing— review and editing, F.P., O.K., N.A. and B.E. All authors have read and agreed to the published version of the manuscript.

References

1. Tiseo, I., *Annual production of plastics worldwide from 1950 to 2020*, Statisca, 2021. **11:** p. 10-21.
2. Da Costa, J.P., T. Rocha-Santos, and A.C. Duarte, *The environmental impacts of plastics and micro-plastics use, waste and pollution: EU and national measures*. EPRS: European Parliamentary Research Service, 19 Aug 2020, Belgium.
3. Moetazedian, A., A. Gledall, X. Han, A. Ekinci, E. Mele, and V. V. Silberschmidt, *Mechanical performance of 3D printed polylactide during degradation. Additive Manufacturing*, 2021. **38:** p. 101764.
4. Patti, A., S. Acierno, G. Cicala, M. Zarrelli, and D. Acierno, *Assessment of recycled PLA-based filament for 3D printing*. Materials Proceedings, 2021. **7**(1): p. 16-23.
5. Garrison, T.F., A. Murawski, and R. L. Quirino, *Bio-based polymers with potential for biodegradability*, Polymers, 2016. **8(7)**: p. 262-271.
6. Solomon, I.J., P. Sevvel, and J. Gunasekaran, *A review on the various processing parameters in FDM*, Materials Today: Proceedings, 2021. **37**: p. 509-514.
7. Aydin, M., B. Güler, and K. Çetinkaya, *Dikey Ekstrüzyon (Filament) Sistemi Tasarim Ve Prototip İmalati*, International Journal of 3D Printing Technologies and Digital Industry, 2018. **2(1)**, p. 1-10.
8. Mirón, V., S. Ferrandiz, D. Juarez, and A. Mengual, *Manufacturing and characterization of 3D printer filament using tailoring materials*, Procedia Manufacturing, 2017. **13**: p. 888-894.
9. Tanabi, H. *Investigation of the temperature effect on the mechanical properties of 3D printed composites*, International Advanced Researches and Engineering Journal, 2021. **5 (2)**: p. 188-193.
10. Shindé, S.L. and J. Goela, *High thermal conductivity materials*, Springer, 2006. **91**: p. 167-198.
11. Singh, R., G. S. Sandhu, R. Penna and I. Farina, "*Investigations for thermal and electrical conductivity of ABS-graphene blended prototypes*, Materials, **10(8)**: p. 881-898.
12. Rumeysa, B. and M. Öksüz, *Polimer Malzemelerin Isıl İletkenlik Özelikleri*, https://www.plastik-ambalaj.com/en/plastic-packaging-article/3014-polimer-malzemelerin-is-l-iletkenlik-oezelikleri, Ocak 23 2022.
13. Sandhu, S., *Investigations for Development of ABS-Grephene Blended Feed Stock Filament for FDM Applications*, PhD. Thesis, Guru Nanak Dev Engineering College Ludhiana, India, 2017.
14. Kazmer, D., *Three-dimensional printing of plastics, in Applied plastics engineering handbook*, Processing, Materials, and Applications, 2017. p. 617-634.
15. Wondu, E., Z.C. Lule, and J. Kim, *Improvement of dielectric properties and thermal conductivity of TPU with alumina-encapsulated rGO*, Polymer Testing, 2021. **102**: p. 107322,
16. Xiong, J., Z. Zheng, X. Qin, M. Li, H. Li, and X. Wang, *The thermal and mechanical properties of a polyurethane/multi-walled carbon nanotube composite*, Carbon, 2006. **44(13)**: p. 2701-2707.
17. Ma, X.-Y. and W.-D. Zhang, *Effects of flower-like ZnO nanowhiskers on the mechanical, thermal and antibacterial properties of waterborne polyurethane*, Polymer Degradation and Stability, 2009. **94(7**): p. 1103-1109.

18. Kuan, H.-C., C. C-M. Ma, W-P. Chang, S-M. Yuen, H-H. Wu, and T-M. Lee. *Synthesis, thermal, mechanical and rheological properties of multiwall carbon nanotube/waterborne polyurethane nanocomposite*, Composites Science and Technology, 2005. **65(11-12)**: p. 1703-1710.
19. Wondu, E., Z. Lule and J. Kim, *Thermal conductivity and mechanical properties of thermoplastic polyurethane-/silane-modified Al2O3 composite fabricated via melt compounding*, Polymers, 2019 **11(7)**: p. 1103.
20. Yuan, C., B. Duan, L. Li, B. Xie, M. Huang, and X. Luo, *Thermal conductivity of polymer-based composites with magnetic aligned hexagonal boron nitride platelets*, ACS applied materials & interfaces, 2015. **7(23)**: p. 13000-13006.
21. Xie, B.-H., X. Huang, and G.-J. Zhang, "High thermal conductive polyvinyl alcohol composites with hexagonal boron nitride microplatelets as fillers", Composites Science and Technology, 2013. **85**: p. 98-103.
22. Ha, S.M., O. H. Kwon, Y. G. Oh, Y. S. Kim, J. C. Won, B. G. Kim, Y. Yoo, *Thermally conductive polyamide 6/carbon filler composites based on a hybrid filler system*, Science and technology of advanced materials, 2015. **16**: p. 1-10.
23. Choi, S.W., K. H. Yoon, and. S. S. Jeong, Morphology and thermal conductivity of polyacrylate composites containing aluminum/multi-walled carbon nanotubes, Composites Part A: Applied Science and Manufacturing, 2013. **45**: p. 1-5.
24. Yu, A., R. Ramesh, X. Sun, E. Bekyarova, M.E. Itkis, and R.C. Haddon, *Enhanced thermal conductivity in a hybrid graphite nanoplatelet–carbon nanotube filler for epoxy composites*, Advanced Materials, 2008. **20(24)**: p. 4740-4744.
25. Incorporated. P.S. 3 Types of Plastic Used in 3D Printing, https://www.polymersolutions.com/blog/plastic-in-3d-printing/, Feb 12, 2023.
26. Kyutoku, H., N. Maeda, H. Sakamoto, and K. Yamada, *Effect of surface treatment of cellulose fiber (CF) on durability of PLA/CF bio-composites*, Carbohydrate polymers, 2019. **203**: p. 95-102.
27. Ultimaker. *Ultimaker Tough PLA TDS*. https://support.makerbot.com/s/article/1667411002379, 17 Feb 2023.
28. Ayrilmis, N., M. Kariz, J.H. Kwon, and M. K. Kuzman, *Effect of printing layer thickness on water absorption and mechanical properties of 3D-printed wood/PLA composite materials*, The International Journal of Advanced Manufacturing Technology, 2019. **102**: p. 2195-2200.
29. Guessasma, S., S. Belhabib, and H. Nouri, *Microstructure and mechanical performance of 3D printed wood-PLA/PHA using fused deposition modelling: Effect of printing temperature*, Polymers, 2019. **11**(11): p. 1778.
30. Magri, A.E., K. E. Mabrouk, and M. Touhami, *Mechanical properties of CF-reinforced PLA parts manufactured by fused deposition modeling*, Journal of Thermoplastic Composite Materials, 2021. **34**(5): p. 581-595.
31. Abbott, A., G.P. Tandom, R.L. Bradford, R.L. Koerner, and J.W. Baur, *Process-structure-property effects on ABS bond strength in fused filament fabrication*, Additive Manufacturing, 2018. **19**: p. 29-38.
32. Petrović, Z.S. and J. Ferguson, *Polyurethane elastomers", Progress in Polymer Science*, 1991. **16(5)**: p. 695-836.
33. Ultimaker. Ultimaker PLA TDS, https://support.makerbot.com/s/article/1667410781972, 11 Ekim 2022.
34. eSUN, *PLA+*, https://www.esun3d.com/uploads/eSUN_PLA+-Filament_TDS_V4.0.pdf, 22 Ocak 2023.
35. Filameon. PLA-CF 15 Filament, https://www.filameon.com/urun/filameon-pla-cf-15-filament/#%20, 06 Eylül 202.
36. Filameon. PLA Wood, https://www.filameon.com/urun/filameon-pla-wood-filament/, 05 Kasım 2022.
37. eSUN, ABS+, https://www.esun3d.com/uploads/eSUN_ABS+-Filament_TDS_V4.0.pdf, 13 Aralık 2022.
38. Filament, S. TPU 92A, https://savafilament.com/standart-92a, 11 April 2022.
39. Nuñez, P., A. Rivas, E.G. Plaza, E. Beamud, and A.S. Lobera, *Dimensional and surface texture characterization in fused deposition modelling (FDM) with ABS plus*, Procedia Engineering, 2015. **132**: 856-863.
40. Şentürk, B., K. Çetin, S.N. Ürküt, N. Anaç, N. and O. Koçar, *Jig design and manufacturing for adhesive thickness control in adhesive joints*, Journal of Materials and Manufacturing, 2022. **1(2)**: p. 17-23.
41. Qi, H., K. Joyce, and M. Boyce, *Durometer hardness and the stress-strain behavior of elastomeric materials*, Rubber chemistry and technology, 2003. **76(2)**: p. 419-435.
42. Topuz, A., B. Erdogan and O. Aycan, *Determination and measurement of some thermophysical properties of nanofluids and comparison with literature studies*, Thermal Science, 2021. **25(5): p.** 3579-3594.
43. Manualslib, https://www.manualslib.com/manual/1247577/Decagon-Devices-Kd2-Pro.html, 07.01.2023.
44. Karaman, E. and O. Çolak, *Eriyik biriktirme yönteminde farklı üretim parametrelerinin mekanik özelliklere etkisi*, ALKÜ Fen Bilimleri Dergisi, 2019. **1(2)**: p. 90-99.
45. Ngo, I. and C. Byon, *Thermal conductivity of particle-filled polymers", Polymer Science Book Series*, 2016. p. 554-565.
46. Kovan, V., G. Altan and E.S. Topal, *Effect of layer thickness and print orientation on strength of 3D printed and adhesively bonded single lap joints*, Journal of Mechanical Science and Technology, 2017. **31**: p. 2197-2201.
47. Shubham, P., A. Sikidar, and T. Chand, *The influence of layer thickness on mechanical properties of the 3D printed ABS polymer by fused deposition modeling in Key engineering materials*, Trans Tech Publ, 2016. **706**, p. 63-67.
48. Tymrak, B., M. Kreiger and J.M. Pearce, *Mechanical properties of components fabricated with open-source 3-D printers under realistic environmental conditions*, Materials & Design, 2014. **58**, p. 242-246.
49. Liu, Z., Q. Lei, and S. Xing, *Mechanical characteristics of wood, ceramic, metal and carbon fiber-based PLA composites fabricated by FDM*, Journal of Materials Research and Technology, **8(5)**: p. 3741-3751.
50. Hanon, M.M., J. Dobos and L. Zsidai, *The influence of 3D printing process parameters on the mechanical performance of PLA polymer and its correlation with hardness*, Procedia Manufacturing, 2021. **54**: p. 244-249.

Available online at www.dergipark.org.tr/en

INTERNATIONAL ADVANCED RESEARCHES and ENGINEERING JOURNAL

Journal homepage: www.dergipark.org.tr/en/pub/iarej

e-ISSN: 2618-575X

International Open Access

Volume 07
Issue 03

December, 2023

Research Article

Design and optimization of a computer simulation model for green hydrogen production by waste heat recovery from Afyon biogas plant

Muhammed ARSLAN [a,*], ***Mehmet KUNT*** [b] ***and Ceyhun YILMAZ*** [c]

[a]*Afyon Kocatepe University, Çay Vocational High School, Afyon, 03700, Turkey*
[b]*EgeUniversity, Ege Vocational High School, İzmir, 35040, Turkey*
[c]*Afyon Kocatepe University, Faculty of Technology, Afyon, 03200, Turkey*

ARTICLE INFO

Article history:
Received
Revised
Accepted

Keywords:
Biogas plant
Optimization
Thermodynamic analysis
Thermoeconomic analysis

ABSTRACT

In this study, a thermodynamic model was designed with the Aspen Plus program and optimized multidimensionally of the Afyon biogas power plant to reduce the unit electricity cost and produce green hydrogen. The model also includes ORC integration to use the exhaust gas energy of the existing power plant. In the model, which includes the whole process from biomass receiving to final electricity production, the plant produces 4000 kW of net electrical power. As a result of ORC integration and optimization, the net electricity production of the plant and ORC were determined as 4625.42 kW and 1215.31 kW, respectively. These values correspond to 0.039 $/kWh unit electricity cost. The power obtained in ORC is stored by producing hydrogen during periods of low electricity demand. For this purpose, ORC power is primarily used to electrolyze H_2S (green hydrogen) released in biogas production. The rest of the power is used in the electrolysis of water. Hydrogen, released in biogas production, is added to the storage process. As a result, approximately 7.447 kg/min of hydrogen is produced at the power plant, costing 0.18 $/kg.

1. Introduction

In 2020, 83% of the world's primary energy consumption is fossil fuels. Energy Council also indicates that it will be 77% in 2040. The energy sector will face fossil fuel scarcity in the future. In addition, population growth and industrial developments have increased the global energy consumption met by fossil fuels. Also, oil and gas extraction techniques are getting more expensive daily. Environmental problems accompany these problems. Using non-renewable energy sources has led to greenhouse climate change, global warming, and gas emissions. These effects have prompted scientists to explore alternative energy technologies. In order to provide energy to a growing population and reduce fossil fuel consumption without harming the environment, switching to a renewable-based energy generation combination is necessary. Biogas can support energy source variations and act as a buffer. Biogas is an important energy source, especially for rural areas, and its other name is green energy. It is a clean energy source that can easily replace fossil fuels and is easy to control. It is mostly (more than 60%) burned in combined heat and power (CHP) to obtain electricity and heat [1-6].

Biogas is an important renewable biofuel produced by the anaerobic digestion of organic wastes such as sewage, animal manure, agro-industrial wastes, landfills, domestic solid waste, and wastewater sludge. In addition to generating heat and electricity in cogeneration systems, it can be used to improve the content of biogas. The gas composition depends on different parameters but generally consists of 35-75% methane, 25-65% carbon dioxide, 1-5% hydrogen, and small amounts of ammonia, water vapor, halides, and hydrogen sulfide. An environmentally friendly fuel feature is that the crops absorb some of the carbon dioxides during biogas production. The upper and lower calorific value of biogas containing 50-75% methane by volume varies between 22-30 MJ/m^3 and 19-26 MJ/m^3, respectively [1, 3, 7-9]. About 40% of the biogas energy is converted to electricity, while about 25% is used to heat the digester. The rest is emitted to the atmosphere as waste heat with exhaust gases. Waste heat units can be used for waste heat recovery. However, waste heat recovery must be economically justified; therefore, a

* Corresponding author. Tel.:0 272 218 35 35 (3505); Fax: 0 272 218 35 33
E-mail addresses: muarslan@aku.edu.tr *(M. Arslan)*, mehmet.kunt@ege.edu.tr *(M. Kunt)*, ceyhunyilmaz@aku.edu.tr *(C. Yılmaz)*
ORCID:0000-0001-8387-7008 *(M. Arslan)*, 0000-0002-2033-6703*(M. Kunt)*, 0000-0002-8827-692X *(C. Yılmaz)*
DOI:10.35860/iarej.1271925

thermo-economic optimization should include the entire waste heat recovery unit. This model should be sized correctly for realistic investment costs [3].

Organic Rankine Cycles are generally used for power generation from low-temperature heat sources. They are important alternatives to reduce costs and emissions. At the same time, it creates another alternative as a bottom cycle for the recovery of waste energy in medium and large-scale CHP plants. This technology has advantages such as simple structure, convenient applicability, and user-friendliness over the traditional steam Rankine cycle and is ideal for using medium-low temperature heat sources (<350 ºC). ORC uses organic working fluids; Isobutane is a typical working fluid for temperatures below 200 ºC, while toluene is generally used at higher welding temperatures. ORC applications have been studied on other fluids such as n-pentane, ethanol, R-11, R-123, HFE7100, iso-pentane, benzene, p-xylene, ammonia, cyclohexane, etc. [10-12].

Many studies have been carried out on cogeneration systems regarding thermodynamics and thermoeconomics.

Holik et al. (2021) proposed a thermo-economic optimization model to exploit the waste heat of a two-engine biogas power plant via the Rankine and Organic Rankine Cycle. With the application of the model, the efficiency of the power plant, which was 66.7%, increased by 2.97% with the Rankine Cycle. The payback period of the investment is 6.8 years, and the electricity cost is determined as 0.0419 $/kWh [3].

Baccioli et al. (2019) performed a thermo-economic analysis of ORC integration in a biogas power plant with a 600 kW micro gas turbine in Italy. In the model they developed, it was observed that 77% energy recovery was achieved, and the payback period of the ORC modification was less than 6 years [13].

Gholizadeh et al. (2020) designed a biogas-fed trigeneration system for electricity, cooling, and freshwater production and optimized it exergo-economically for different working fluids. As a result of optimization, a 2.58 % increase in net electricity, 22.69% in cooling load, 14.04% in TGOR (trigeneration-based gain-output-ratio), and 13.26% increase in exergy efficiency was obtained with toluene. The unit cost of the trigeneration system has decreased by 6.71% [14].

Gholizadeh et al. (2019) integrated a gas turbine cycle into the bi-evaporator electric/cooling cogeneration system and analyzed the power plant thermodynamically with the EES program. The cooling load of their proposed system is 505.2 kW; on the other hand, the net electricity it can produce is 1168 kW, and its energy and exergy efficiencies are 54.54% and 36.83%, respectively as a result of integrating the system with the gas turbine cycle increased energy and exergy efficiency by 67.3% and 19.15%, respectively [15].

Gholizadeh et al. (2019) made the feasibility of a biogas-powered gas turbine cycle with ORC. They performed thermodynamic and thermo-economic analyses to estimate system performance and cost. As a result of the analysis, the net electrical power, energy efficiency, exergy efficiency, and total product cost are 1368 kW, 41.83%, 38.91%, and 17.2 $/GJ, respectively [16].

Lu et al. (2022) proposed a new strategy to increase a biogas energy plant's energy efficiency and economic effectiveness. The study consists of 4E and sensitivity analyses. According to simulation results, the plant's thermal efficiency increased from 38% to 46%. The developed system reduces CO_2 emissions by 5100 tons per year. The dynamic payback period and the net present value of the system are about 9.1 years and 4.5 M$, respectively [17].

He et al. (2023) designed a multi-generation system powered by biogas and produced hydrogen, analyzed and optimized thermodynamic, thermoeconomic, and economic. According to thermodynamic analysis results, the system produces 108.7 kW power and 888.7 kW cooling load, respectively; it also produces 703.3 kg/h hydrogen by integrating the steam reforming method and purification process into the system. The energy and exergy efficiencies of the system were also calculated as 31.51% and 31.14%, respectively. The thermoeconomic analysis results show that the total product cost is 16.23 $/GJ [18].

Zhou et al. (2023) proposed a method for a biogas cogeneration system that is powered by biogas and generates electricity and cooling with recovered heat from liquefied natural gas (LNG). The cogeneration system was investigated in terms of thermodynamic, exergoeconomic, environmental, economic, and multi-objective optimization. According to thermodynamic analysis, the developed system produces 1864 kW of electricity and 424.1 kW of cooling power. It has also 80.4% energy efficiency and 41.24% exergy efficiency. According to thermoeconomic analysis, the system has 10.07 $/GJ for the unit's overall product cost for a selling price of 0.27 $/kWh for cooling and 0.06 $/kWh for electricity. Finally, according to environmental analysis, the cogeneration system reduces amounts of CO_2 released from 6091 kg/MWh to 3913 kg/MWh after optimization [19].

Gargari et al. (2019) performed the multi-criteria optimization of the power plant in terms of energetic, exergetic, exergoeconomic, and environmental aspects. As a result of the optimization, the system has a 123.59 MW cooling capacity, 0.73 MW heating capacity, 280.35 MW net power, 18.14 kg/h distilled water, and 0.2432 kg/h hydrogen production capacity. In this case, the system's energy efficiency is 72.75%, the exergy efficiency is 50.21%, the unit product cost is 6.79 $/GJ, and the environmental penalty cost rate (environmental penalty

cost rate) is determined as 168 $/h [4].

Abusoglu et al. (2021) investigated the potential of district heating (DH) based on biogas, heat, and electricity production of a wastewater treatment plant. The study consists of district heating scenario I (DH Scenario I) based on excess biogas storage and exhaust gas and district heating scenario II (DH Scenario II) based on exhaust gas and power output using all biogas. According to the analysis results, with the district heating scenario I, 458 houses can be heated, and the natural gas needs 1112 houses with the same heating load; with district heating scenario II, the heating load of 755 houses can be met with waste heat. In addition, payback periods for district heating scenarios I and II are calculated as 2.5 and 2 years, respectively [8].

Cao et al. (2021) proposed a biogas-fed seasonal gas turbine cycle in terms of thermodynamics and economy. They designed and optimized a cogeneration system for electricity/heating and electricity/cooling, with the bottom cycle independent of the season. As a result, energy efficiency, exergy efficiency, and cost of products were calculated as 79.2%, 45.6%, and 21.7 $/GJ for summer, and 70.7%, 37%, and 17.6 $/GJ for winter, respectively [7].

This study presents a realistic model to reduce the unit cost of electricity produced by a biogas power plant operating in Afyon, make exhaust gases less harmful, and use waste exhaust gas energy. The current power plant has a power of 4 MW and does not utilize exhaust gas waste heat. In this regard, the model proposes the integration of an ORC into the power plant and optimizing the combined system. With the proposed model, the power plant produces green hydrogen by electrolysis of water by producing extra electricity with waste heat.

2. Afyon Biogas Plant and Operating Principle

The Afyon biogas plant is given in Figure 1. Afyon Biogas Plant produces biogas by decomposing 150,000 tons of organic vegetable and animal waste annually in an airless environment with anaerobic fermentation technology. The power plant has an electrical power of 4000 kW. It produces odorless, solid organic fertilizer with high organic matter content, free from gases and other components which harm the air and soil, after hygiene process of raw material. The plant solves this problem by transforming it into renewable energy and organic fertilizer production with high organic matter content. So, 177,000 tons of carbon emissions annually are prevented as well as disposing of animal and vegetable origin wastes, a important environmental problem. Solid and liquid organic fertilizer production are 20,000 and 80,000 tons/year, respectively.

The operating principle of the Afyon biogas plant is given in Figure 2. The biomass received by the plant is mixed with water in the circulation tank. It is then sent to the reactor to be digested. Biogas is released as a result of digestion. The biogas is passed through a bio cleaner and a dryer to turn into pure methane.

On the other hand, atmospheric air is compressed by a compressor. The exhaust gas heats the compressed air in the preheater and is ready for combustion. In the combustion chamber, methane gas and air perform the combustion reaction. Exhaust gas from the combustion reaction runs the turbine, producing electricity. The shaft power produced is converted into electrical power by the generator. Exhaust gas is passed through the air preheater due to its high energy. Finally, the exhaust gas is sent to the reactor to increase the temperature. In this study, the exhaust gas drives an ORC before the reactor. So, the power plant efficiency increases, and the electricity produced becomes cheaper. While the electricity produced in the existing power plant is transferred to the grid, The electricity produced in the ORC is used to produce hydrogen. In this way, hydrogen energy can be used when needed.

The hydrogen separated from the biogas in the bio cleaner is sent to the hydrogen tank, and hydrogen sulfide separated from the biogas in the bio cleaner is sent to electrolysis. The power required for electrolysis is supplied from the ORC. The remaining ORC power is used in the electrolysis of water. The exhaust gas driving the ORC then heats the water to increase efficiency in water electrolysis. Finally, the exhaust gases are sent to the reactor and released into the atmosphere.

3. Analyzes and Optimization

3.1 Thermodynamic Analysis

The thermodynamic analysis is done to see the thermodynamic performance of the power plant and to be a preliminary step towards optimization with thermoeconomic analysis. The power plant is optimized by using thermodynamic and thermoeconomic equations. The main equations given below were used for thermodynamic analysis. The electrical power, ORC power, and net electrical power of the plant are:

$$\dot{W}_{electricity} = \dot{W}_{turbine} - \dot{W}_{compressor} \tag{1}$$

$$\dot{W}_{ORC} = \dot{W}_{ORC\,turbine} - \dot{W}_{pump} \tag{2}$$

$$\dot{W}_{Net\ electricity} = \dot{W}_{electricity} + \dot{W}_{ORC} \tag{3}$$

Specific physical exergy and physical exergy are:

$$ex_{phy.n} = h_n - h_0 - T_0(s_n - s_0) \tag{4}$$

$$\dot{E}x_{phy.n} = \dot{m}_n ex_{phy.n} \tag{5}$$

Chemical exergy is:

$$\dot{E}x_{ch.n} = \sum_{k=1} x_k ex^{-}_{ch_k} + \overline{R}T_0\left(\sum_{k=1} x_k \ln^{x_k}\right) \tag{6}$$

So, total exergy is:

$$\dot{E}x_n = \dot{E}x_{phy.n} + \dot{E}x_{ch.n} \tag{7}$$

Figure 1. Afyon biogas plant [20].

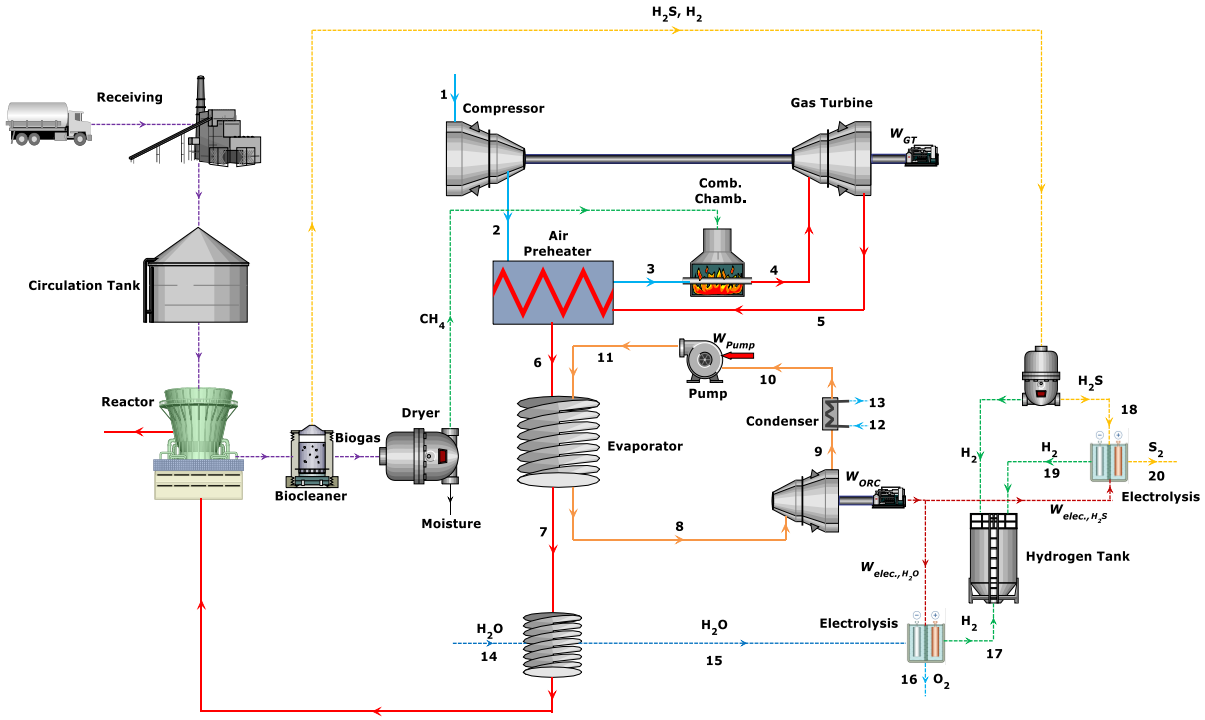

Figure 2. The operating principle of the Afyon biogas plant.

In this case, energy and exergy efficiencies are where *HV* is the heating value of biogas:

$$\eta_{energy} = \frac{\dot{W}_{Net\ electricity}}{\dot{m}_{biogas} HV_{biogas}} \quad (8)$$

$$\eta_{exergy} = \frac{\dot{W}_{Net\ electricity}}{\dot{E}x_{biogas}} \quad (9)$$

In addition, the equations used in the electrolysis are as follows:

$$\Delta G + T\Delta S = \Delta H \quad (10)$$

$$\eta_{energy} = \frac{HV_{H_2}\dot{m}_{H_2}}{\dot{W}_{electricity}} \quad (11)$$

$$\eta_{exergy} = \frac{\sum \dot{E}x_{products}}{\dot{W}_{electricity} + \dot{E}x_{reactants}} \quad (12)$$

3.2 Thermoeconomic Analysis

Thermoeconomic analysis is done to calculate the unit costs of the products of the plant. Exergetic data obtained in the thermodynamic analysis are used in thermoeconomic analysis. Each exergy is based on a specific cost to establish an economic relationship between the plant's products, equipment, heats, works, fuel, operating and maintenance, etc. The capital recovery factor, total cost rates, and unit costs must be calculated. The main equations used in thermoeconomic analysis are as follows. Here *CRF*, *i*, and *n* are capital recovery factors, interest rate = 15% and plant life = 20, respectively.

$$CRF = \frac{i(1+i)^n}{(1+i)^n - 1} \quad (13)$$

C_k, φ and $\dot{Z}_k$ are equipment purchasing cost, operation and maintenance factor and total cost rate, respectively.

$$\dot{Z}_k = \frac{C_k(CRF)\varphi}{(n \times 3600)} \quad (14)$$

The exergy cost rate equations are as follows:

$$\dot{C}_w = c_w \dot{W} \quad (15)$$

$$\dot{C}_q = c_q \dot{E}x_q \quad (16)$$

$$\dot{C}_i = c_i \dot{E}x_i = c_i(\dot{m}_i ex_i) \quad (17)$$

$$\dot{C}_e = c_e \dot{E}x_e = c_e(\dot{m}_e ex_e) \quad (18)$$

A cost balance for a system component can be written as follows:

$$\sum_i \dot{C}_{i,k} + \dot{C}_{q,k} + \dot{Z}_k = \sum_e \dot{C}_{e,k} + \dot{C}_{w,k} \quad (19)$$

3.3 Optimization

The main factor in formulating an optimization problem is the selecting of independent variables which characterize design options. In selection of variables, there is a need to consider entire critical variables which affect the cost-effectiveness and performance of system, not select variables that are too detailed or unimportant, and distinguish between independent variables whose values may vary. For example, in a preliminary design, it is generally optional to consider each system component's design details [21].

In this study, optimization was made in the Aspen Plus program to maximize the CHP net electrical power and minimize unit electricity cost in a multidimensional way. Aspen Plus is chemical process optimization software used by the biochemical industries to design, operate, and optimize safe and profitable manufacturing facilities. Aspen Plus changes many parameters to increase economic performance. These parameters can be the increase or decrease of pressures and temperatures or the addition or removal of equipment in the workflow. With the change made, the economic performances of the existing and changed processes are compared. If the modified process does not meet the optimization goal, the process is changed again. Optimization parameters and operating limits are given in Table 1 [22].

4. Results and Discussion

To facilitate interpretation of the results, Figures 3, 4, and 5 represent key findings from the optimization process. Figure 3 shows the effect of the change in AFR on net electricity generation. According to the figure, the power produced by the plant increases with the increase of AFR. However, with the increase of AFR, the exhaust gas (T_6) temperature that drives the ORC unit decreases. For this reason, the working fluid Toluene cannot be evaporated in the ORC unit because the T_6 temperature drops excessively at AFR values greater than 70. Therefore, this area is a risky area for ORC business fluid. The optimum AFR has been determined as 70 to avoid power loss in the ORC unit.

Table 1. Optimization parameters and operating limits.

Parameter	Operating Limits
Air-fuel ratio (AFR)	50 – 70
Rise of pressure(r_p)	6 – 15
T_3 (K)	750 – 825

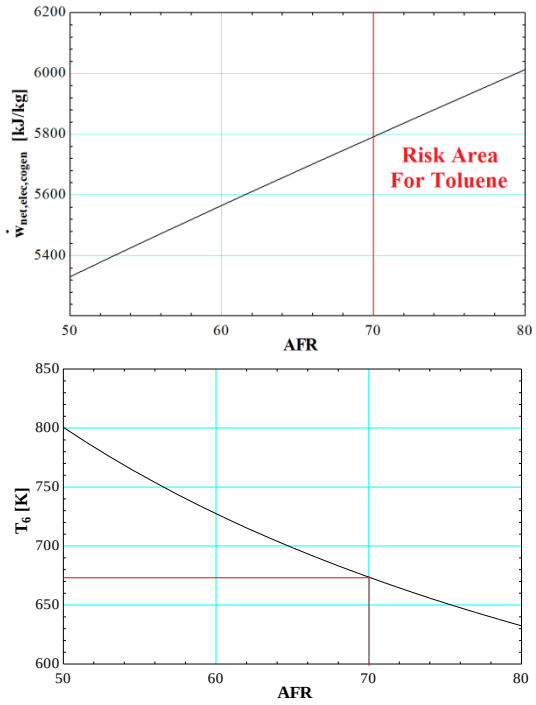

Figure 3. The effect of the change in AFR on net electricity generation.

Figure 4 shows the effect of the change in rp on net electricity generation. In Figure 4, r_p of 9.393 is the compressor's critical value; at higher r_p values, the net power produced from the plant decreases. Therefore, the compression ratio is determined as the optimum r_p.

Figure 5 shows the effect of the change in T_3 temperature on the net power produced by the plant. According to the figure, as the T_3 temperature increases, the power of the plant increases. However, as the T_3 temperature increases, the exhaust temperature T_6 decreases. As in Figure 3, since the exhaust gas temperature of T_6 drops too much at levels of T_3 higher than 780 K, the working fluid (Toluene) cannot be evaporated in the ORC. Therefore, T_3 temperatures above 780 K are risky for the working fluid in the ORC cycle. Therefore, the optimum T_3 temperature is determined as 780 K.

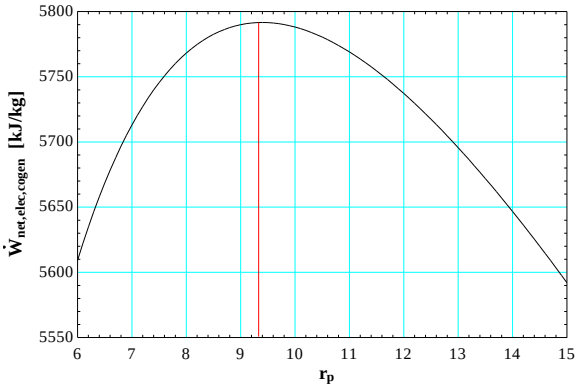

Figure 4. The effect of the change in r_p on net electricity generation.

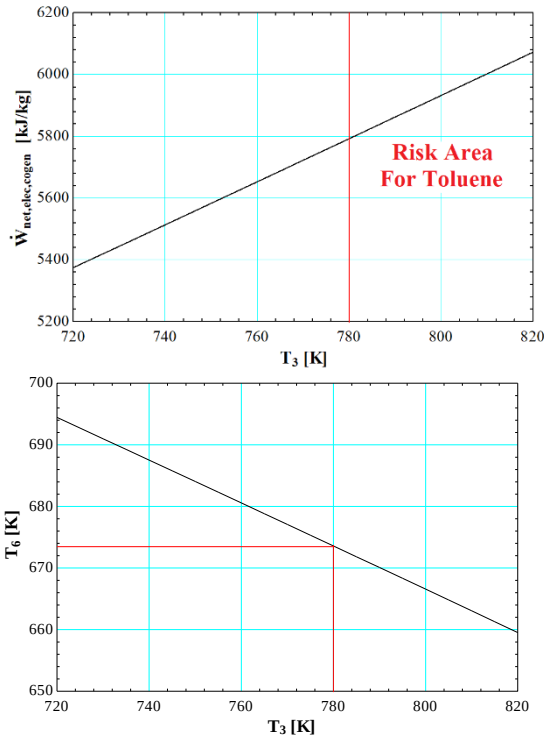

Figure 5. The effect of the change in T_3 on net electricity generation.

Figure 6 shows the Afyon biogas plant designed and optimized in Aspen Plus. The upper left side of the figure represents biogas production from biomass. The upper right side shows the electricity production of an existing plant. The released exhaust gases drive the ORC at the bottom right side, producing ORC power. On the lower left side, the electrolysis of water is seen. The light green lines in the middle of the figure represent hydrogen storage.

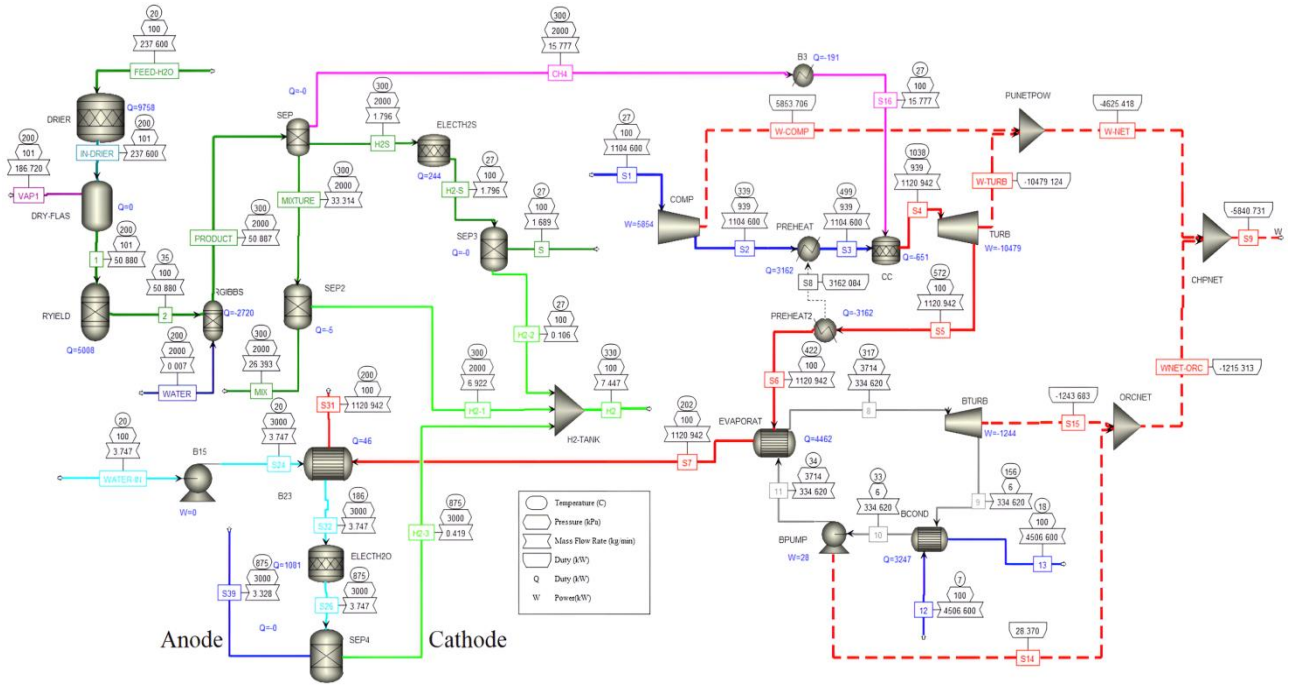

Figure 6. The model designed and optimized in Aspen Plus of Afyon biogas plant.

The figure shows that 5840.73 kW of total power can be produced in the plant. 4625.41 kW of total power is used for electricity generation. Also, 71.86 kW of the 1215.31 kW of power produced in ORC is used at electrolysis of H_2S to produce 0.106 kg/min green hydrogen because if H_2S is not separated from biogas, it damages equipment [23]. The remaining 1095.14 kW ORC power is used at electrolysis to produce 0.419 kg/min hydrogen. In addition, 6,922 kg/min of hydrogen released during biogas production is stored in a hydrogen tank. Therefore, the final hydrogen production is 7.447 kg/min. According to thermodynamic analysis, the energy and exergy efficiency of the plant were calculated as 42% and 36.81%, respectively.

According to thermoeconomic analysis, the cost of unit electricity produced by the plant, which was optimized, was calculated as 0.039 $/kWh. The unit costs of hydrogen obtained from the electrolysis of H_2S and water electrolysis were obtained as 1.42 $/kg and 2.85 $/kg, respectively. The unit cost of hydrogen released in the biogas production process is 0. Therefore, the average hydrogen unit cost is 0.18 $/kg.

5. Conclusions

This study designed a 4000 kW Afyon biogas power plant model to produce cheaper electricity, release less harmful exhaust gas to the environment, and use waste exhaust gas energy. Then, the model was analyzed in terms of thermodynamics and thermoeconomics. The critical results of the study are as follows:

- To use the energy of waste exhaust gas, an ORC was integrated into the power plant, and the combined plant was optimized multi-dimensionally.
- In this way, the power of the plant was increased, and the unit electricity cost was reduced. Reducing unit electricity cost also reduces unit hydrogen cost.
- Generating electricity by utilizing the energy of the exhaust gas ensures that less energetic exhaust gas is released into the atmosphere. In this way, less harm is done to the environment.
- The electricity produced in ORC is stored by hydrogen production when electricity demand is low. ORC power is not used directly in water electrolysis to produce hydrogen. It is first used in H_2S electrolysis to remove H_2S, a harmful component with corrosion for the fuel injection system, and released during biogas production. It is also an advantage that the power required for the electrolysis of H_2S is less than that required for the electrolysis of water [24]. The remaining ORC power is used in the electrolysis of water.

Declaration

The author(s) declared no potential conflicts of interest with respect to the research, authorship, and/or publication of this article. The author(s) also declared that this article is original, was prepared in accordance with international publication and research ethics, and ethical committee permission or any special permission is not required.

Author Contributions

M.K. wrote the introduction chapter, and M.A. designed the model, carried out analyses, and formed methodology, formulation, and conclusions. C.Y checked up on analyses, grammar, and content of the entire study.

Nomenclature

AFR	: Air-fuel ratio
$\dot{C}$	: Exergy cost rate ($/h)
C_k	: Equipment purchasing cost ($)
ch	: Chemical
CHP	:Combine heat and power
CRF	: Capital recovery factor
ex	: Spesific exergy (kJ/kg)
$\dot{E}x$	: Exergy (kW)
G	: Gibbs free energy (kJ/kmol)
h	: Spesific enthalpy (kJ/kg)
HV	: Heating Value (kJ/kg)
H_2S	: Hydrogen sulfide
i	: Interest rate (%)
n	: Plant life (year)
ORC	: Organic rankine cycle
phy	: Physical
r_p	: Rise of pressure
s	: Specific entropy (kJ/kgK)
S	: Entropy (kJ/K)
T	: Temperature (^{o}C or K)
$\dot{W}$	: Power (kW)
$\dot{Z}_k$	: Total cost rate ($/h)
η	: Efficiency (%)
Δ	: Change
$\sum$	: Summation symbol
φ	: Operation and maintenance factor
4E	: Energy, exergy, economic and environmental

References

1. Momayez, F., K. Karimi, and I. S. Horváth, *Enhancing ethanol and methane production from rice straw by pretreatment with liquid waste from biogas plant*. Energy Conversion and Management, 2018. **178**: p. 290–298.
2. Laperrière, W., B. Barry, M. Torrijos, B. Pechiné, N. Bernet, and J. P. Steyer, *Optimal conditions for flexible methane production in a demand-based operation of biogas plants*. Bioresource Technology, 2017. **245**: p. 698–705.
3. Holik, M., M. Zivic, Z. Virag, A. Barac, M. Mujanovic, and J. Avsec, *Thermo-economic optimization of a Rankine cycle used for waste-heat recovery in biogas cogeneration plants*. Energy Conversion and Management, 2021. **232**: p. 113897.

4. Gargari, S. G., M. Rahimi, and H. Ghaebi, *Energy, exergy, economic and environmental analysis and optimization of a novel biogas-based multigeneration system based on Gas Turbine-Modular Helium Reactor cycle*. Energy Conversion and Management, 2019. **185**: p. 816-835.
5. Khoshgoftar Manesh, M. H., A. Razazadeh, and S. Kabiri, *A feasibility study on the potential, economic, and environmental advantages of biogas production from poultry manure in Iran*. Renewable Energy, 2020. **159**: p. 87-106.
6. Calise, F., F. L. Cappiello, L. Cimmino, M. D. d'Accadia, and M. Vicidomini, *Dynamic analysis and investigation of the thermal transient effects in a CSTR reactor producing biogas*. Energy, 2023. **263:** p. 126010.
7. Cao, Y., H. A. Dhahad, H. Togun, M. A. Haghghi, A. E. Anqi, N. Farouk, and M. A. Rosen, *Seasonal design and multi-objective optimization of a novel biogas-fueled cogeneration application*. International Journal of Hydrogen Energy, 2021. **46**(42): p. 21822-21843.
8. Abusoglu, A., A. Tozlu, and A. Anvari-Moghaddam, *District heating and electricity production based on biogas produced from municipal WWTPs in Turkey: A comprehensive case study*. Energy, 2021. **223**: p. 119904.
9. Song, Y., S. F. Ahmad, M. A. Houran, M. K. Agrawal, T. U. K. Nutakki, M. R. Siddiqui, A. Albani, and Q. Su, *Multi-variable study of a novel multigeneration system using biogas separation unit and LNG cold energy utilization, producing electricity, cooling, heat, fresh water, liquid CO_2, biomethane, and methanol*. Process Safety and Environmental Protection, 2023. **180:** p. 616 – 638.
10. Facão, J., and A. C. Oliveira, *Analysis of Energetic, Design and Operational Criteria When Choosing An Adequate Working Fluid For Small ORC Systems*, in *IMECE2009*. 2009. Florida: p. 12420.
11. Ge, Z., J. Li, Y. Duan, Z. Yang, and Z. Xie, *Thermodynamic Performance Analyses and Optimization of Dual-Loop Organic Rankine Cycles for Internal Combustion Engine Waste Heat Recovery*. Appl. Sci., 2019. **9**: p. 680.
12. Karthikeyan, B., and G. P. Kumar, *Thermoeconomic and optimization approaches for integrating cooling, power, and green hydrogen production in dairy plants with a novel solar-biomass cascade ORC system*. Energy Conversion and Management, 2023. **295:** p. 117645.
13. Baccioli, A., L. Ferrari, F. Vizza, and U. Desideri, *Feasibility analysis of coupling an ORC to a mGT in a biogas plant*. Energy Procedia, 2019. **158**: p. 2311-2316.
14. Gholizadeh, T., M. Vajdi, and H. Rostamzadeh, *Exergoeconomic optimization of a new trigeneration system driven by biogas for power, cooling, and freshwater production*. Energy Conversion and Management, 2020. **205**: p. 112417.
15. Gholizadeh, T., M. Vajdi, and H. Rostamzadeh, *Energy and exergy evaluation of a new bi-evaporator electricity/ cooling cogeneration system fueled by biogas*. Journal of Cleaner Production, 2019. **233**:p.1494-1509.
16. Gholizadeh, T., M. Vajdi, and F. Mohammadkhani, *Thermodynamic and thermoeconomic analysis of basic and modified power generation systems fueled by biogas*. Energy Conversion and Management, 2019. **181:** p. 463–475.
17. Lu, F., C. Pan, H. Zhu, F. Pan, and Q. Wu, *Energy management strategy for a biogas plant in Anhui, China based on waste heat recovery and thermoeconomic analysis*. Energy Conversion and Management, 2022. **273:** p. 116399.
18. He, J., N. Han, M. Xia, T. Sun, and H. Ghaebi, *Multi-objective optimization and exergoeconomic analysis of a multi-generation system based on biogas-steam reforming*. International Journal of Hydrogen Energy, 2023. **48:** p. 21161 –21175.
19. Zhou, J., M. A. Ali, A. M. H. Wais, S. F. Almojil, A. I. Almohana, A. F. Alali, M. R. Ali, and M. Sohail, *A novel modified biogas-driven electricity/cooling cogeneration system using open-and-closed Brayton cycle concepts: Environmental Analysis and Optimization*. Ain Shams Engineering Journal, 2023. In Press, Available online 22 March 2023, 102230.
20. Enerji Gunlugu. [cited 2023 18 December]; Available from: https://www.enerjigunlugu.net/epdk-afyon-biyogaza-17-yil-3-ay-uretim-izni-verdi-39863h.htm
21. Bejan, A., G. Tsatsaronis, and M. J. Moran, *Thermal design and optimization*. 1995, USA: John Wiley & Sons.
22. Aquino, J. R., M. A. C. Bautista, D. C. F. Lat, and R. C. M. Liave, *Optimization and Economic Performance Improvement of Processes Using Aspen HYSYS and Streamlined Life Cycle Assessment*, in 6th*ICENV2018*. 2019. p. 020020.
23. Mutegoa, E., and M. G. Sahini, *Approaches to mitigation of hydrogen sulfide during anaerobic digestion process – A review*. Heliyon, 2023. **9:** p. e. 19768.
24. John, S., j. C. Hamann, S. S. Muknahallipatna, S. Legowski, J. F. Ackerman, and M. D. Argyle, *Energy efficiency of hydrogen sulfide decomposition in a pulsed corona discharge reactor*. Chemical Engineering Science, 2009. **64:** p. 4826 – 4834.

Available online at www.dergipark.org.tr/en

INTERNATIONAL ADVANCED RESEARCHES and ENGINEERING JOURNAL

Journal homepage: www.dergipark.org.tr/en/pub/iarej

e-ISSN: 2618-575X

International Open Access

Volume 07
Issue 03

December, 2023

Research Article

Combined application of ANN prediction and RSM optimization of performance and emission parameters of a diesel engine using diesel-biodiesel-propanol fuel blends

Yusuf Karabacak [a,*], ***Doğan Şimşek*** [b] ***and Nuri Atik*** [a]

[a]*Depart. of Mechatronics Technology, Army NCO Vocational HE School, National Defence University, Balıkesir,10100, ,Türkiye*
[b]*Depart. of Automotive Technology, Army NCO Vocational HE School, National Defence University, Balıkesir,10100, ,Türkiye*

ARTICLE INFO

Article history:
Received 03 July 2023
Accepted 15 October 2023
Published 15 December 2023

Keywords:
ANN
Biodiesel
Emission
Engine performance
Propanol
RSM

ABSTRACT

In this study, an artificial neural network (ANN) was used to estimated the performance and exhaust emission parameters of a diesel engine running on diesel, biodiesel, and propanol fuel mixtures. In addition, the parameters estimated by ANN were tried determining the optimum operating parameter by using Response Surface Methodology (RSM). In the experimental study, propanol was added in 3 different ratios (5%, 10% and 20%) into 100% diesel, 80% diesel and 20% biodiesel fuel blends. In addition, engine tests, were made at 5 different engine speeds with 400 min^{-1} intervals between 1000 min^{-1} and 2600 min^{-1} revolutions at full load. In addition, HC (Hydrocarbon), CO (Carbon Monoxide), NOx (Nitrogen oxides) and Smoke emissions were measured during in the working. ANN model was developed for estimation of engine output parameters depending on fuel mixture ratios and engine speed. In the ANN results, the regression coefficients (R^2) of the proposed model were found to be between 0.924 and 0.99. When the obtained ANN results were compared with the experimental results, it was seen that the maximum mean relative error (MRE) was 6.895%. It has been shown that the applied model can predict with a low error rate. The RSM results showed that the optimum operating parameters were 2034-min^{-1} engine speed, 74.667% diesel, 11.36% biodiesel and 15% propanol fuel mixture. In addition, in the validation tests of the model where the desirability was 0.7833%, the highest error rate was obtained as 7.37% as a result of NOx. As a result of the study, it was seen that RSM supported ANN is a good method for estimating diesel engine parameters working with diesel/biodiesel/propanol mixtures and determining optimum operating parameters.

1. Introduction

In the last quarter century, the limited fossil-based resources, have encouraged researchers to explore different alternative fuels [1-6]. In addition, increasing environmental concerns as a result of the use of petroleum-based fuels are the other and main reason for these studies. Studies on reducing emissions from motor vehicles are being studied by many researchers with different methods [7-10]. In addition to these studies, esters of vegetable and animal oil, especially for diesel engines, were remarkable. Vegetable oil methyl esters, however, are encountered a number of issues, including low energy content, high density and viscosity, iodine value, and poor volatility. [11, 12]. While vegetable oil methyl esters can be used alone as fuel in the studies, they can also be used by mixing with diesel fuel in certain proportions. Especially in diesel/biodiesel fuel blends, it can provide almost the same engine torque and power, while causing an increase in specific fuel consumption (due to lower energy content) [13]. However, the general consensus in the studies is that there is a decrease in HC (hydrocarbon), CO (carbon monoxide) and soot emissions while using biodiesel and diesel biodiesel fuel mixtures, while NOX emissions increase [2, 14, 15]. The use of biodiesel as a fuel is a suitable fuel choice among biofuels due to these advantages. However, with long-term use of biodiesel in the engine, some negative consequences (such as accumulation of injectors, sticking of pistons and rings, dilution in engine oil) can be seen. Therefore, there may be a need to improve the fuel properties of vegetable oils [16]. For this reason, a fuel that can be mixed with biodiesel and has complementary properties is needed to minimize the difficulties arising from the diesel-biodiesel

* Corresponding author. Tel.: +90-266-221-23-50; Fax: +90-266-221-2358.
E-mail addresses: ykarabacak@msu.edu.tr *(Y. Karabacak)*, dsimsek@msu.edu.tr *(D. Şimşek)*, natik@msu.edu.tr *(N.Atik)*
ORCID: 0000-0001-9864-7512 *(Y. Karabacak)*, 0000-0002-5509-9314 *(D. Şimşek)*, 0000-0001-5203-3646 *(N.Atik)*
DOI: 10.35860/iarej.1322332

fuel mixture. Most of the researchers working in this field prefer alcohol as an additional fuel or oxygen additive [14, 17]. Especially since the high viscosity of biodiesel needs to be reduced, many researchers have recently started to use alcohol in compression ignition engines by mixing it with biodiesel [18, 19]. Propanol is a 3-carbon alcohol with a high energy density, straight chain structure, making it a potential alternative to light alcohols (methanol and ethanol). The most economical method for producing propanol from petrochemicals is called oxo synthesis [20]. But in order to make this alcohol, sustainable methods have been devised due to worries about the depletion of fossil fuel stocks. From sources like biomass or household solid waste, propane can be manufactured [21]. Although propanol is seen as a good alternative among alcohol fuels, its ratio in diesel or biodiesel is limited. According to the European diesel fuel quality norm EN590, mixtures above 45% by volume do not meet the requirements for kinematic viscosity and lubricity at higher mixing ratios [22]. For this reason, although propanol is seen as a good alternative fuel, its ratio in the fuel mixture is an important parameter.

A statistical analytic tool known as an artificial neural network (ANN) is used to accurately anticipate output results based on input values that have undergone training. It is also a supervised machine learning technique that shows sharp results due to its highly sensitive algorithm. ANN allows to reduce the time and cost required for multiple experiments and increase the overall efficiency of the system [23, 24]. Therefore, ANN can solve a wide variety of problems for engineering applications where traditional and numerical techniques have become tedious and time consuming. The time cost reduction of ANN has been used in the estimation of performance and emission parameters in internal combustion engines as in many different engineering fields in recent years [25-27]. ANN is capable of producing correct motor behavior. This allows it to act as an inexpensive virtual sensing system for on-board measurement of engine performance and emission characteristics in real time. However, Response Surface Methodology (RSM), a statistical analysis tool, is widely used to know the effect of each input variable on the output effect, especially when the output response is affected by three or more independent variables. It is also widely used to determine and predict the optimum combination of input variables for desired properties from RSM output parameters [27, 28]. Furthermore, RSM (Response Surface Methodology) is more advantageous compared to other methods in terms of simultaneously changing and optimizing effective parameters with the minimum number of experiments, to achieve maximum information [29-31]. In many studies in the literature, there are many studies with RSM approach for the optimization of engine responses by using biodiesel fuel in diesel engines. Atmanlı et al. [18] stated that they utilized RSM to optimize the triple fuel mixture with the goal of achieving maximum performance and minimum emissions. According to their findings, the optimal mixing ratio of diesel-Butanol-cotton oil methyl ester, with a predictability level of 0.98, is 65.5%, 23.1%, and 11.4% (by volume), respectively. Similarly, Simsek and Uslu, [32] determined the optimum injection pressure, biodiesel ratio and engine load parameters for maximum Brake Thermal Effect (BTE) and minimum emission parameters in their optimization study using RSM optimization technique. In their results, they reported that the error rates for different parameters were between 1.5% and 7.26%, and that RSM was an effective method to optimize various motor parameters. In their study, Yilmaz et al. [29] utilized the RSM (Response Surface Methodology) approach to determine the optimal blending ratio of eight different fuel mixtures prepared by adding alcohol to a diesel-biodiesel blend. They successfully developed a complete second-degree mathematical model with a 95% confidence level based on the obtained results. They stated that the validation test results yielded a successful outcome with a low error rate. Similarly, Rajesh Kumar et al., [33] conducted an optimization study for the minimum BSFC and NOX effect of injection timing and EGR (Exhaust Gas Recirculation) in their studies with biofuels prepared by adding alcohol such as dimethyl-carbonate, isobutanol and n-pentanol to diesel fuel. The optimum operating parameters for minimum BSFC and NOx were obtained as 0.988 for isobutanol/diesel mixture at 22° BTDC and 0% EGR valve opening. They stated that there was an error rate of about 5% between the estimated and mean experimental values. When the studies in the literature are examined, it is seen that the RSM-based optimization technique is widely used to improve the engine performance and emissions of different engine operating parameters with diesel/biodiesel dual and triple fuel mixtures such as diesel/biodiesel/alcohol. However, there are not enough studies in which the ANN technique to predict the diesel engine input and output parameters of Artificial Intelligence (AI) techniques and the RSM technique to optimize it together. In addition, in this study, two different techniques were used and compared to determine the optimum parameters to eliminate some the negative effect of biodiesel. In this context, in this study, the estimation of the optimum biodiesel and alcohol ratio for maximum engine performance and minimum BSFC and emission parameters and the optimum parameters were determined according to these estimation results. It is aimed that the results obtained in the study are an important approach to improve the emission results, especially to determine the fuel mixture ratios and to contribute to the literature in this field.

2. Materials and Methods

2.1 Experimental Setup

In experimental studies, sunflower oil methyl ester obtained by transesterification method was used. Propanol alcohol was obtained from Sigma-Aldrich company with 99% purity. In experimental studies, test fuels are 100% diesel (D), 80% diesel + 20% biodiesel (B80), 75% diesel + 20% biodiesel + 5% propanol (P5), 70% diesel + 20% biodiesel + 10% propanol (P10).) and 65% diesel + 20% biodiesel + 15% propanol (P15). Some properties of the fuels used are given in Table 1.

Prepared test fuels were carried out in a single-cylinder four-stroke air-cooled ANTOR 3 LD 510 brand experimental engine. Test engine specifications are given in Table 2. An electric dynamometer is used in the test system with a torque of 26 kW, 80 Nm and a maximum speed of 5000 rpm. The schematic view of the engine test stand used in the experimental studies is given in Figure 1. In the test system, fuel consumption, engine torque and engine power data were instantly recorded digitally with the interface program used. The interface program used is shown in Figure 2. The test was carried out at 5 different engine speeds (1000-1400-1800-2200-2600 min^{-1}) in full load position. The tests were waited until the engine temperature was reached, then measurements were made.

Exhaust emission measurements were made at all engine speeds. Mobydic brand gas analyzer, whose characteristics are given in Table 3, was used for emission measurements. All tests were repeated three times and the average value was calculated and used.

Table 1. Physical properties of use fuels

Properties	D2	Biodiesel	Propanol
Molecular weight (kg/kMol)	210	------	74.12
C (%)	86.13	77.1	64.82
H (%)	13.87	12.1	13.49
O (%)	0	10.8	21.59
Cetan number	52	56	12
Density (kg/m^3) 15 °C	835	884	803.7
Viscosity (mm/s2) 40 °C	2.72	4.51	1.74
Lower calorific value (Mj/kg)	42.49	38.65	30.63
Evaporation heat (kj/kg)	375	-----	727.88

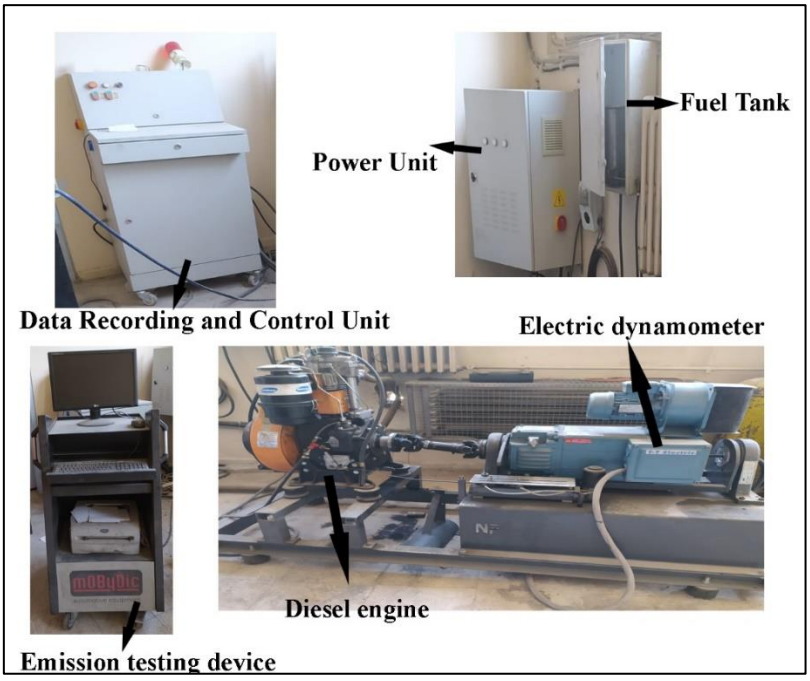

Figure 1. Schematic view of the experimental setup

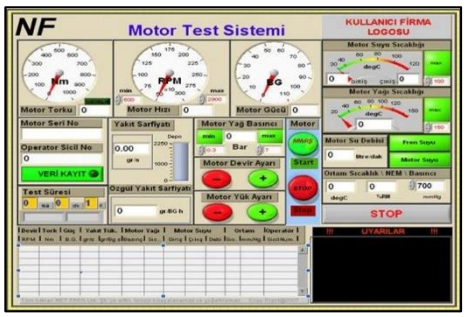

Figure 2. The interface program used.

Table 2. Properties of test engine

Engine Type ANTOR 3 LD 510	
Cylinders Number	1
Cylinder Diameter x Stroke	85 x 90 mm
Cylinder Displacement	510 cm^3
Compression Ratio	17:01
Maximum Engine Speed	3200 min^{-1}
Maximum Engine Power	12 Hp
Maximum Engine Torque	35 Nm 1800 min^{-1}

Table 3. Emission device measuring ranges

MOBYDIC 5000 GAS ANALYZER	
CO % Vol	0 – 10
CO_2 % Vol	0 – 20
HC ppm	0 – 20000
O_2 % Vol	0 – 21
NOx ppm	0 – 5000
Lambda	0 – 5
n %	0 – 100
k 1/m	0 – 20
Particle mg/m^3	0 – 1000

2.2 ANN

ANN is one of the AI methods inspired by the biological nervous system and used for solving various engineering problems, especially for which traditional modeling techniques are inadequate [34]. ANN is widely used in different engineering fields [35]. It is a mathematical and computational modeling technique that has been widely used in the automotive industry, especially in the processing of performance and emission parameters of internal combustion engines [36]. There is no limit to the number of layers in modeling with ANN. Generally, three layers are used in modelling. These layers are called input, output and hidden layers [37]. ANN progresses through three distinct stages. The first stage is modelling, the second stage is the learning (training stage) and the last stage is the testing stage. In the first stage, a model was created according to the input and obtained results (output) parameters (factors) used in the testing phase. In the training phase, the model was run to generate a target estimate based on the network input parameters. The output parameters obtained in the test procedure and the estimated values with the model prepared were compared, and the training phase was stopped when the error between the predicted results and the test results reached an acceptable value. In order to measure the prediction success of the created model, the regression coefficients MRE (Mean Relative Error) and RMSE (Root Mean Square Error) created with the goals and outputs of the ANN model and given in Equation 1-3 were used [38].

$$R^2 = 1 - \left(\frac{\sum_{i=1}^{n}(t_i - o_i)^2}{\sum_{i=1}^{n}(o_i)^2}\right) \quad (1)$$

$$MRE(\%) = \frac{1}{n}\sum_{i=1}^{n}\left|100\frac{t_i - o_i}{t_i}\right| \quad (2)$$

$$RMSE = \sqrt{\frac{1}{n}\sum_{i=1}^{n}(t_i - o_i)^2} \quad (3)$$

Here, 'n' is the amount of data in the information set, 'o' is the predicted output data, and 't' is the actual output. In the prepared model, engine speed, diesel, biodiesel and propanol ratios as input layer parameters, Engine Power (EP), Engine Torque (ET), Brake Specific Fuel Consumption (BSFC), Hydrocarbon (HC), Nitrous oxides (NOx) as output layer parameters, Carbon monoxide (CO) and soot emissions were selected. The schematic view of the developed ANN is shown in Figure 3. A commonly used feedforward backpropagation network type was chosen to explain complex problems in system modeling and description [39]. Generally, the Levenberg-Marquardt (Trainlm) training function is applied for precise predictions where the mean square error (MSE) determines the failure function of the network [40]. The (4-16-7) topology was used to estimate the input-output parameters. Four neurons make up the input layer, sixteen neurons make up the hidden layer, and six neurons make up the output layer in this example. Because it is a differentiable, continuous, and nonlinear function, the logarithmic sigmoid (logsig) activation function outperforms other functions in creating the right model, according to the majority of studies [41].

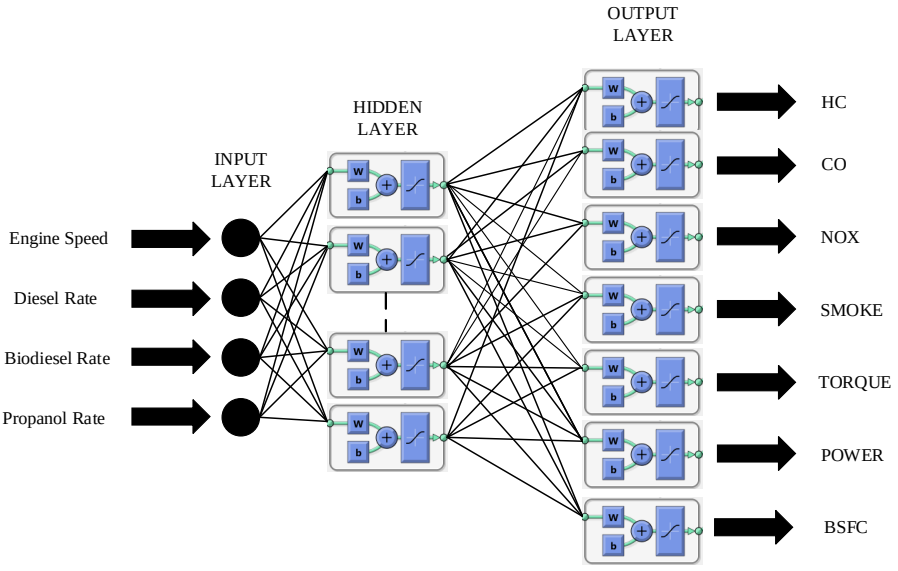

Figure 3. The schematic representation of the ANN

Table 4. Properties of neural network

Network	4 inputs, 7 outputs and 1 hidden layer
Network Type	Feed-forward back propagation
Data	Training: Randomly selected data from the experimental data at the rate of 80%. Test: Randomly selected data of 10% from experimental data. Confirmation: Randomly selected data of 10% from experimental data.
Training function	Trainlm
Adaptation learning function	Learngdm
Transfer function	Logsis
Performance function	Mean Square Error
Stopping criteria	Stop training the network when the validation error starts to increase.

Table 5. Input parameters

Input Factor	Code	Levels		
Engine Speed (min-1)	A	1000	1800	2600
Biodiesel (%)	B	0	20	-
Diesel (%)	C	75	70	65
Iso-propanol (%)	D	5	10	15

2.3 RSM

Response Surface Methodology (RSM), which has achieved successful results in applications in many different fields, is a computer-based application. This application is widely used for modeling and optimization of the performance and emissions of internal combustion engines [13, 40, 41]. RSM establishes a relationship between input and output parameters. It optimizes the responses according to the input factors, according to the relationship between the input and output parameters. For this purpose, RSM uses the least squares technique. According to RSM, each of the motor input parameters is assumed to be computable and can be expressed by the equation given below [42]:

$$y = f(X_1, X_2, \dots, X_n) \tag{4}$$

Here; X_1 X_1 …. X_n respectively, the input parameters and y are the output parameters. The first step in RSM consists of the field or independent variables of the process and empirical statistical modeling in order to develop empirical relationships for estimation and optimization, and to develop an appropriate approximation relationship between response and process variables. A quadratic equation model is applied for this relationship as shown below [38].

$$y = \beta_0 + \sum_{i=1}^{k} \beta_i x_i + \sum_{i=1}^{k} \sum_{j\geq 1}^{k} \beta_{ij} x_i x_j + \sum_{i=1}^{k} \beta_{ii} x_i^2 + \varepsilon \tag{5}$$

The linear coefficient, the quadratic coefficient j, the regression coefficient β, the number of parameters k, and the error ε found in the response are all given in this equation. Central Composite Design (CCD), which provides results that are considerably more exact when compared to other experimental designs, has been used in this investigation. The optimization is mainly aimed at maximizing ET and EP while minimizing BSFC, NOX, CO, HC and Soot emissions. At the same time, it is aimed to establish functional relationships between ANN estimated target parameters (ET, EP, BSFC, NOx, HC, CO and is) and design parameters. Input variables were chosen as engine speed (ES), Biodiesel ratio and Propanol ratio. Input variables and levels are given in Table 5. ET, BSFC, HC, CO, NOX and S are selected as output parameters of the model.

3. Results and Discussion

3.1 ANN Result

In this study, an ANN was designed by using the data obtained from experimental studies to predict diesel engine parameters. The general regression plot obtained from the designed ANN is given in Figure 4. When the general regression graphs obtained from the ANN given in Figure 4 are examined, the correlation coefficients are 0.99996 for training, 0.9983 for validation, and 0.98999 for testing. The overall (Training, Validation and Testing) correlation coefficient was 0.99863. The fact that the correlation coefficient is close to 1 indicates that the accuracy is high [38]. The fact that these values are very close to 1 shows high accuracy in modelling the outputs obtained from the designed ANN results. Baranitharan et al. [26] stated in their study that the correlation coefficient (R-value) of 0.99 indicates the success of the Artificial Neural Network (ANN) model in predicting diesel engine performance. They further emphasized that the R-value of the motor performance and emission characteristics demonstrates the accurate prediction of the output responses by the ANN model [43]. Additionally, the obtained prediction values from the ANN model show a high level of agreement with the experimental values [44] (Figure 5 and Figure 6).Comparison results of experimental results and estimation results for EP, BSFC, ET are given in Figure 5. When the comparison charts of the experimental results and estimation results for ET, EP, BSFC given in Figure 5 are examined, it is seen that the experimental results and the ANN estimation results are highly similar. The R^2 value was obtained as 0.924, 0.99 and 0.907, respectively. Results from the ANN model show that the use of ANN is sufficient to predict ET, EP and BSFC. In a study by Akçay et al., [7] they stated that the R^2 value of all the equations

used was 0.98 0.99. As a result, diesel engine operation can be estimated with acceptable error value for further investigation using obtained equations or given algorithms. Also Rao et al., [28] they used a multi-layered sensing (MLP) network for nonlinear matching between input and output parameters in a study where they examined the performance and emissions of an engine with biodiesel and isopropanol added. In their results, they stated that ANN can predict engine performance and emissions with a correlation coefficient in the range of 0.98-0.999. The RMSE values obtained from the ANN results were 0.82 Nm, 0.224 kW and 11.96 g/kWh for ET, EP and BSFC, respectively, while the MRE values were 1.907%, 5.96% and 4.14%, respectively. Similarly, comparison charts of experimental results and estimation results for emission results (CO, HC, NOX and soot) are given in Figure 6. When the comparison charts of the experimental results and the estimation results for HC, CO, NOX and soot emissions given in Figure 6 are examined, it is seen that the experimental results and the ANN estimation results are in high agreement. The R^2 values obtained from the designed ANN model were obtained as 0.9895, 0.9433, 0.948 and 0.9596, respectively. The obtained R^2 values show that the model used is sufficient for estimating the relevant emissions. The RMSE values for HC, CO, NO_X and soot emissions were obtained as 1.47 ppm, 0.23%, 118.23 ppm and 0.17%, respectively. Similarly, MRE values were obtained as 3.86%, 23.36%, 3.19% and 5.82%, respectively. Similar results have been reported in previous studies [38, 42, 45]. Comparisons of the estimation results and experimental results obtained with the ANN model used are given in Table 6 for exhaust emissions, and engine performance comparisons are given in Table 7. The equation used to determine the % error value in the comparison is given in Equation (6).

$$error = \frac{test\ result - predicted\ result}{test\ result}\ x\ 100 \qquad (6)$$

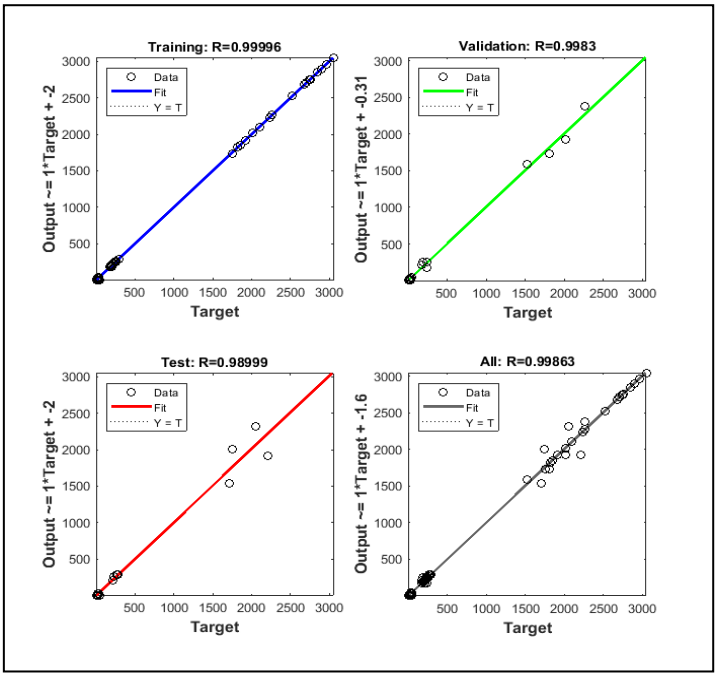

Figure 4. Regression graphs of training, testing, validation, and all results of ANN

Table 6. Comparison of experimental and prediction results for exhaust emissions

Engine Speed (min^{-1})	Biodiesel Ratio (%)	Diesel Ratio (%)	Propanol Ratio (%)	Value	HC (ppm)	CO (%)	NOx (ppm)	Smoke (%)
1000	20	75	5	ANN	46.273	2.198	1623.81	3.265
				Experimental	45	2.35	1742	3.36
				Error (%)	2.82	6.46	6.78	2.82

Table 7. Comparison of experimental and prediction results for engine performance

Engine Speed (min^{-1})	Biodiesel Ratio (%)	Diesel Ratio (%)	Propanol Ratio (%)	Value	ET (Nm)	EP (kW)	BSFC (g/kWh)
1000	20	75	5	ANN	24.03	2.545	266.62
				Experimental	22.78	2.55	278.87
				Error (%)	5.48	0.19	4.39

When the comparison results of the experimental and estimation results given in Table 6 and Table 7 are examined, it is seen that the output parameters for the input parameters of 1000 min^{-1} engine speed 75% diesel, 20% biodiesel and 5% propanol have low error rates for both engine performance and exhaust emissions appears to be predictable. Experimental results for HC, CO, NO_X and Smoke emissions were 45 ppm, 2.35%, 1742 ppm and 3.36 %, respectively, while in the ANN estimation results, they were 46,273 ppm, 2.198 %, 1623.81 ppm and 3.265 %, respectively. It is seen that the estimation results are close to each other with the experimental results. The % error rates were obtained as 2.82, 6.46, 6.78 and 2.82, respectively. Similarly, in the comparison made for engine performance, it is understood that it can be predicted with high accuracy. While the experimental results for ET, EP and BSFC were obtained as 22.78 Nm, 2.55 kW and 278.87 g/kWh, respectively, the ANN estimation results were obtained as 24.03 Nm, 2.545 kW and 266.62 g/kWh, respectively. It is seen that the % error rates are 5.58, 0.19 and 4.39, respectively. Previously, Kurtgoz et al., [46] reported that the ANN models they designed in a study they designed gave good results with high correlation and low error rates for the prediction of performance values in spark ignition biogas engine.

3.1 RSM Result

Analysis of variance (ANOVA) results for engine performance (ET, EP and BSFC) and emissions (HC, CO, NO_X and smoke) are given in Table 8.

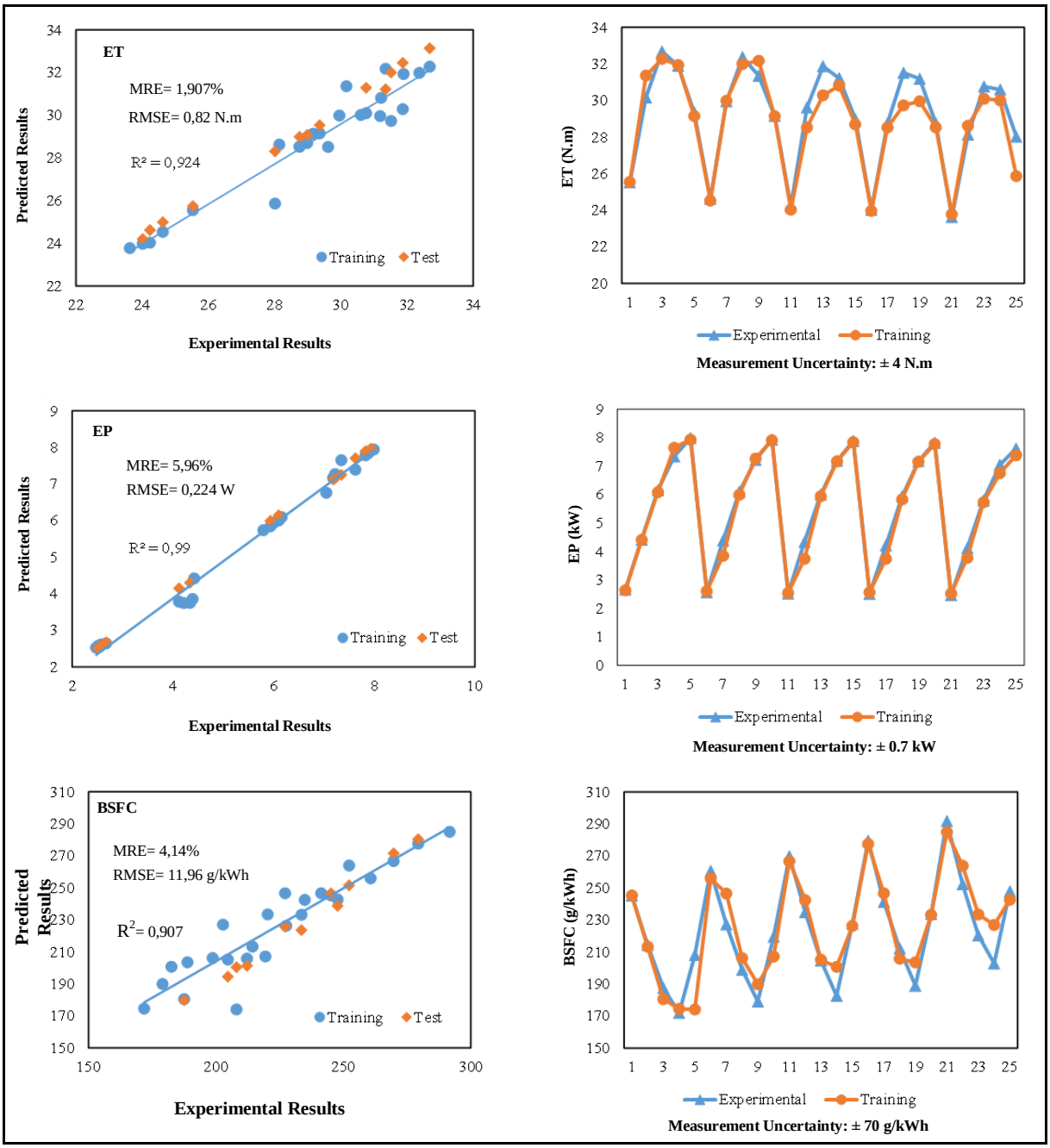

Figure 5. ANN prediction results with experimental results for engine performance results

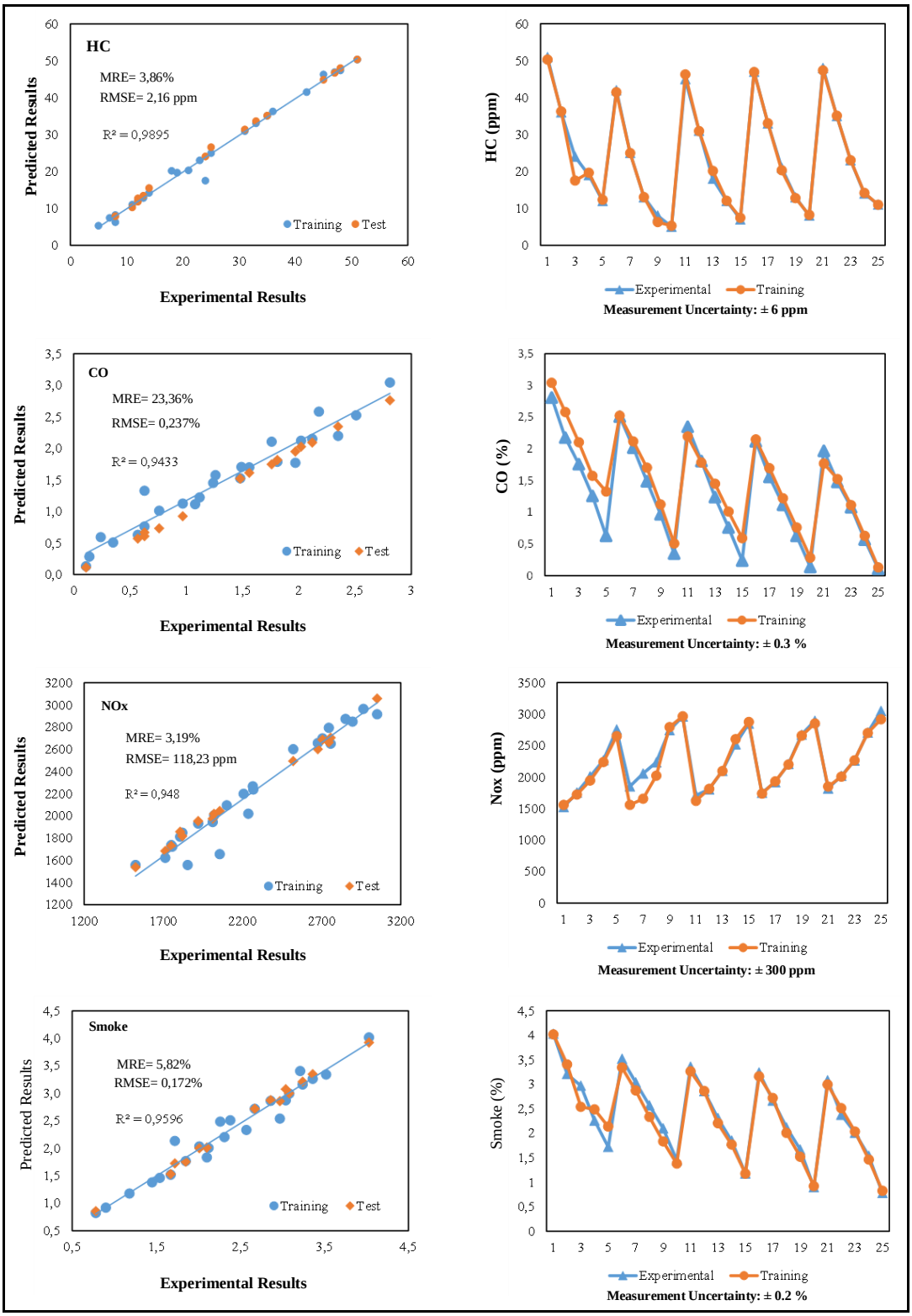

Figure 6. ANN prediction results with experimental results for exhaust emission results

When the ANOVA results given in Table 8 are examined, it is understood that the model and linear coefficients of all outputs are important. It is seen that the p values given in Table 8 are less than 0.05. Analysis of variance (ANOVA) provides numerical information for the probability value [47]. In the ANOVA results, the p value is a parameter that indicates whether the model is important or not. A "p" value greater than 0.05 indicates that the model is unimportant. If a factor's p-value is less than 0.05, it means that the factor has a high impact on the model under development [48]. In the developed model, it is understood that the biodiesel, diesel and propanol ratios are insignificant for all outputs, and the engine speed is important for all outputs. The correlation coefficients of the proposed model for engine performance and exhaust emissions are given in Table 9.

Table 8. Analysis of Variance for engine performance and exhaust emissions

	DF	ET	EP	BSFC	HC	CO	NO_X	Smoke
		p-value	p-value	p-value	p-value	p-value	p-value	p-value
Model	9	0.000	0.000	0.000	0.000	0.000	0.000	0.000
Linear	4	0.000	0.000	0.000	0.000	0.000	0.000	0.000
(A) Engine Speed	1	0.000	0.000	0.000	0.000	0.000	0.000	0.000
(B) Biodiesel	1	0.243	0.811	0.880	0.062	0.886	0.609	0.481
(C) Diesel	1	0.293	0.749	0.806	0.130	0.703	0.716	0.575
(D) Propanol	1	0.424	0.748	0.841	0.224	0.948	0.724	0.485
Square	2	0.000	0.002	0.000	0.000	0.349	0.089	0.633
A^2	1	0.000	0.000	0.000	0.000	0.154	0.031	0.479
C^2	1	0.812	0.656	0.698	0.670	0.949	0.991	0.529
2-Way Interaction	3	0.084	0.745	0.954	0.894	0.096	0.046	0.386
AxB	1	0.328	0.682	0.908	0.522	0.039	0.307	0.607
AxC	1	0.290	0.671	0.896	0.518	0.042	0.357	0.584
AxD	1	0.241	0.635	0.903	0.528	0.049	0.429	0.617

Table 9. Correlation coefficients of the proposed model for engine performance and exhaust emissions

	ET	EP	BSFC	HC	CO	NOX	İs
R^2 (%)	97.29	98.62	92.56	98.72	99.37	97.33	98.57
Adj.R^2 (%)	95.67	97.79	88.10	97.95	98.99	95.73	97.72
Pred.R^2 (%)	90.75	95.98	78.92	96.83	97.18	92.33	95.25

The modified version of R^2 (Adjusted R^2) shows the conformity of the estimators with the conventional estimation. Significant factor (Predictors R^2) shows how well a regression model predicts responses from new observations. Adj. R^2 and Pred. When the R^2 values are examined, it is understood that the values for ET, EP, BSFC, HC, CO NO_X and is are compatible at an acceptable level. The highest difference between these values is approximately 9.18%. In a previous study, Adj. R^2 and Pred. It has been reported that the difference between the R^2 values is less than 20% and therefore these values are reasonably compatible [49]. Second-order regression equations produced by RSM to estimate the output parameters depending on the input parameters are given in Equation 7-13, respectively.

$$HC = 1076- 0.255Engine\ Speed – 8.23Biodiesel – 11.7Diesel – 8.76Propanol + 0.000012Engine\ Speed*Engine\ Speed + 0.0198\ Diesel * Diesel + 0.00179\ Engine\ Speed*Biodiesel + 0.00187\ Engine\ Speed*Diesel + 0.00194\ Engine\ Speed*Propanol \quad (7)$$

$$CO = -42.5 + 0.0221\ Engine\ Speed + 0.418Biodiesel + 0.475Diesel + 0.431Propanol- 0.0000001Engine\ Speed*Engine\ Speed – 0.00011Diesel*Diessel – 0.000225Engine\ Speed*Biodiesel – 0.000229Engine\ Speed*Diesel – 0.000234Engine\ Speed*Propanol \quad (8)$$

$$NOx = 18564- 12.8Engine\ Speed- 186Biodiesel – 170Diesel - 138Propanol + 0.000177\ Engine\ Speed*Engine\ Speed – 0.02Diesel*Diesel + 0.138Engine\ Speed*Biodiesel + 0.128Engine\ Speed\ *Diesel + 0.117Engine\ Speed*Propanol \quad (9)$$

$$Smoke = 44.7- 0.0109Engine\ Speed – 0.265Biodiesel – 0.570Diesel – 0.346Propanol + 0.0000001Engine\ Speed*Engine\ Speed + 0.00177Diesel*Diesel + 0.000087Engine\ Speed*Biodiesel + 0.000095Engine\ Speed\ *Diesel + 0.000092Engine\ Speed*Propanol \quad (10)$$

$$ET = -257 + 0.1122Engine\ Speed + 2.14Biodiesel + 2.91Diesel + 2.69Propanol – 0.000008Engine\ Speed*Engine\ Speed – 0.0030Diesel*Diesel – 0.000740Engine\ Speed\ *Biodiesel – 0.000831Engine\ Speed\ *Diesel – 0.000983Engine\ Speed\ *Propanol \quad (11)$$

$$EP = -69 + 0.0247Engine\ Speed + 0.383Biodiesel + 0.95Diesel + 0.574Propaol – 0.000001Engine\ Speed*Engine\ Speed- 0.00298Diesel*Diesel – 0.000164Engine\ Speed*Biodiesel – 0.000176Engine\ Speed\ *Diesel – 0.000210Engine\ Speed\ *Propanol \quad (12)$$

$$BSFC = 1856 - 0.49\,Engine\ Speed - 5.1\,Biodiesel - 23.3\,Diesel - 8.0\,Propanol + 0.000074\,Engine\ Speed*Engine\ Speed + 0.095\,Diesel*Diesel + 0.0017\,Engine\ Speed*Biodiesel + 0.0020\,Engine\ Speed*Diesel + 0.0020\,Engine\ Speed*Propanol \quad (13)$$

The applied RSM model was used to determine the optimum parameters of engine speed, diesel, biodiesel and propanol ratios, taking into account the predictive values of the developed ANN model. In the RSM model, the optimization is designed to maximize the engine performance parameters ET, EP, and minimize it for the BSFC and emission parameters (HC, CO NO_X and smoke). Optimum operating parameters obtained from the optimization results are given in Figure 7.

When the optimization results given in Figure 7 are examined, it is seen that 2034 min^{-1} engine speed, 11.3% biodiesel ratio, 74.667% diesel ratio and 15% propanol ratio are obtained. The best responses corresponding to the optimum operating parameters are 171.642 g/kWh for BSFC, 7.54kW for EP, 32.27 Nm for ET, 1.14% for soot emissions, 2488.8 ppm for NO_X emissions, 1.08% for CO emissions, and HC emissions It was found as 7.51 ppm for the obtained optimization results show that the engine performance and exhaust emission parameters are significantly affected by the input parameters. Dubey et al., [50] developed a regression model to analyze the effects of input parameters on BSFC, BTE, smoke, NOx , CO and HC in their study where they evaluated the effect of diesel biodiesel binary fuel mixture on engine performance and emissions experimentally and analytically. They stated that the input parameters were effective on BSFC, BTE, smoke, NOx, CO and HC and were statistically significant. In addition, they stated that the maximum desirability of the dual fuel mixture was 0.928, and the adequacy of the model was below 6% with validation tests. In addition, a combined desirability (D) value close to 1 is an indicator of optimization acceptability. In the obtained optimization results, the combined desirability was obtained as 0.7833. The obtained desirability value shows that the optimization works well. Confirmation test results of RSM results are given in Table 10. It can be seen that the validation test results can be obtained with a very low error rate for both engine performance and exhaust emission results. It is seen that the highest error rate for all results was in the ET response with 6.36%. When similar studies in the literature are examined, it is seen that the results obtained are close to the literature [47, 48, 51]. In a study by Şimşek et al [52] using RSM, they stated that the maximum error between the experimental results and the optimum results was 4.96%. In the results obtained, they stated that the RSM model could successfully model a single-cylinder diesel engine.

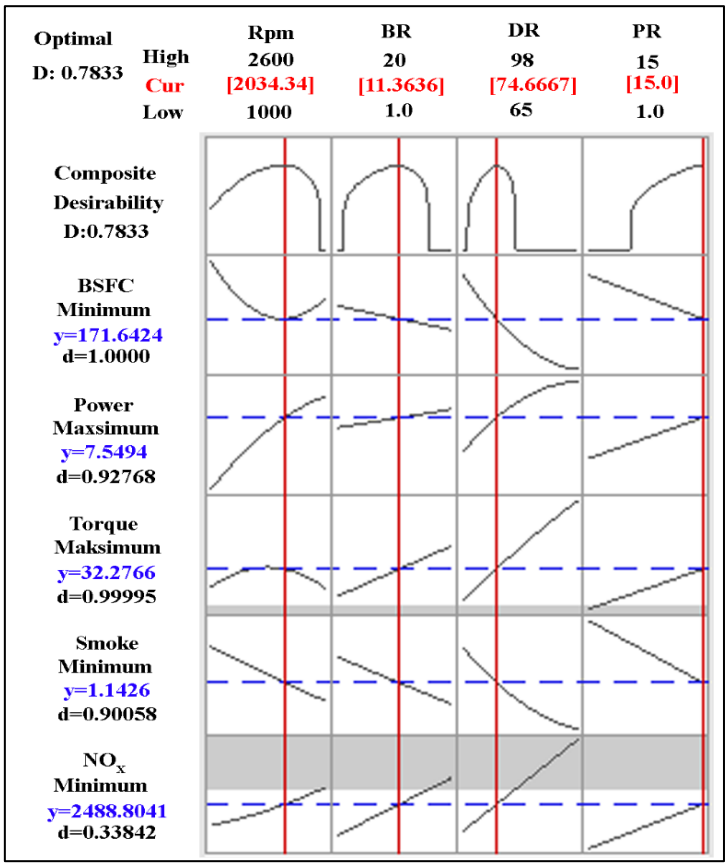

Figure 7. Optimization results

Table 10. RSM validation test results

Engine Speed (min^{-1})	Biodiesel Ratio (%)	Diesel Ratio (%)	Prop. Ratio (%)	Value	ET (Nm)	EP (kW)	BSFC (g/kWh)	HC (ppm)	CO (%)	NO_X (ppm)	Smoke (%)
1000	20	75	5	Opt.	24.2	2.53	269.76	44.225	2.276	1613	3.3
				Exp.	22.7	2.55	278.87	45	2.35	1742	3.36
				E. (%)	6.36	0.78	3.26	1.72	3.15	7.37	1.78

3. Conclusion

In this study, it is aimed to determine the optimum operating parameters of a diesel engine working with diesel biodiesel and propanol fuel mixtures. For this reason, an ANN model was developed and it was aimed to reduce the number of experiments to determine engine parameters. Optimum operating parameters of the obtained ANN results were determined with an RSM-based optimization model. In the ANN results, the R^2 values for ET, EP, BSFC, HC, CO, NO_X and soot emissions were obtained as 0.924, 0.99, 0.907, 0.989, 0.943, 0.948 and 0.959, respectively. The RMSE values of the ANN results were obtained as 0.82 Nm, 0.224 kW, 11.96 g/kWh, 1.47 ppm, 0.23%, 118.23 ppm and 0.17%, respectively. The MRE values of the ANN results were obtained as 1.907%, 5.96%, 4.14%, 3.19%, 26.37%, 3.86%, 5.82%, respectively. When the ANN and experimental results are compared, it is seen that the performance and exhaust emissions of a diesel engine operating with a diesel/biodiesel/propanol mixture can be predicted with a low error rate. In the RSM-based optimization results, the optimum engine operating (input) parameters were obtained as 2034 min-1 engine speed, 74.667% diesel ratio, 11.36% biodiesel ratio and 15% propanol ratio. On the other hand, the output parameters were obtained as 32.28 Nm, 7.55 kW, 171.64 g/kWh, 7.51 ppm, 1.08%, 2488.8 ppm and 1.14% for ET, EP, BSFC, HC, CO, NOX, and smoke, respectively. In the confirmation tests of the RSM results, it was seen that the results were close to the results obtained from the experimental study. In the validation test, the highest error rate was obtained as 6.36%. During the validation tests, it was observed that the error rate of the responses obtained with RSM was lower compared to ANN. Additionally, training the ANN model requires a larger amount of data (test results). However, RSM allows for predictions with a limited number of test results. Considering both the monetary and time aspects, RSM is believed to be more prominent.

Declaration

The author declared no potential conflicts of interest with respect to the research, authorship, and/or publication of this article. The author also declared that this article is original, was prepared in accordance with international publication and research ethics, and ethical committee permission or any special permission is not required.

Author Contributions

First Author and second author developed the methodology. Second author performed the experimental study. First Author and third author performed the analysis studies. First Author and second author supervised and improved the study. Authors wrote the manuscript together. Second author proofread the manuscript.

References

1. Aydın, M., Uslu, S and Çelik, M.B., *Performance and emission prediction of a compression ignition engine fueled with biodiesel-diesel blends: A combined application of ANN and RSM based optimization.* Fuel, 2020. **269**: p. 117472.
2. Çelik M.B. and Şimşek, D., *The determination of optimum injection pressure in an engine fuelled with soybean biodiesel/diesel blend.* Thermal Science, 2014. **18**(1): p. 229-238.
3. Koçak, M.S., Ileri, E. and Utlu, Z., *Experimental study of emission parameters of biodiesel fuels obtained from canola, hazelnut, and waste cooking oils.* Energy & Fuels, 2007. **21**(6): p. 3622-3626.
4. Ozer, S. and Doğan, B., *Thermodynamic analyzes in a compression ignition engine using fuel oil diesel fuel blends.* Thermal Science, 2022, **26**(4): p.3079-3088.
5. Sahin, F., Halis, S., Yıldırım, E., Altın, M., Balaban, F., Solmaz, H. and Yücesu, H.S., *Effects of premixed ratio on engine operation range and emissions of a reactivity controlled compression ignition engine.* SAE International Journal of Fuels and Lubricants, 2023, **16**(2): p. 169-179.
6. Vural, E. and Serkan, Ö., *The investigation of effect of the ceramic coatings with bond-layer coated on piston and valve surface on engine performance of a diesel engine*. International Advanced Researches and Engineering Journal, 2020, **4**(2): p. 87-93.
7. Akcay, M., Özer, S. and Satılmış, G., *Analytical Formulation for Diesel Engine Fueled with Fusel Oil/Diesel Blends*. Journal of Scientific & Industrial Research, 2022, **81**(7): p.712-719.
8. Ertugrul, I., Ulkir, O. Ozer, S. and Ozel, S., *Analysis of thermal barrier coated pistons in the COMSOL and the effects of their use with water+ ethanol doped biodiesel*. Thermal Science, **26**(4-A): p. 2981-2989.
9 Serkan, Ö., Vural, E. and Binici, M., *Taguchi method for investigation of the effect of TBC coatings on NiCr bond-coated diesel engine on exhaust gas emissions.* International Advanced Researches and Engineering Journal, 2020, **4**(1): p. 14-20.
10. Vural, E., Özer, S., Özel, S. and Binici, M., *Analyzing the effects of hexane and water blended diesel fuels on emissions and performance in a ceramic-coated diesel engine by Taguchi optimization method.* Fuel, 2023, **344**: p. 128105.

11. Bhale, P.V., Deshpande, N.V., and Thombre, S.B., *Improving the low temperature properties of biodiesel fuel*. Renewable Energy, 2009, **34**(3): p. 794-800.
12. Moser, B.R., *Influence of blending canola, palm, soybean, and sunflower oil methyl esters on fuel properties of biodiesel.* Energy & Fuels, 2008, **22**(6): p. 4301-4306.
13. Ileri, E., Karaoglan, A.D. and Atmanli, A., *Response surface methodology based prediction of engine performance and exhaust emissions of a diesel engine fuelled with canola oil methyl ester.* Journal of Renewable and Sustainable Energy, 2013, **5**(3): p. 033132.
14. Ma, Q., Zhang, Q., Liang, J. and Yang, C., *The performance and emissions characteristics of diesel/biodiesel/alcohol blends in a diesel engine*. Energy Reports, 2021, **7**: p. 1016-1024.
15. Özkan, M., *Comparative study of the effect of biodiesel and diesel fuel on a compression ignition engine's performance, emissions, and its cycle by cycle variations*. Energy & Fuels, 2007, **21**(6): p. 3627-3636.
16. Şimşek, D. and Çolak, N.Y., *Biyodizel/Propanol yakıt karışımlarının dizel motor emisyonlarına etkisinin incelenmesi.* El-Cezeri Journal of Science and Engineering, 2019, **6**(1): p. 166-174.
17. Aydin, H. and Ilkılıc, C., *Effect of ethanol blending with biodiesel on engine performance and exhaust emissions in a CI engine.* Applied Thermal Engineering, 2010, **30**(10): p. 1199-1204.
18. Atmanli, A., *Effects of a cetane improver on fuel properties and engine characteristics of a diesel engine fueled with the blends of diesel, hazelnut oil and higher carbon alcohol.* Fuel, 2016, **172**: p. 209-217.
19. Liang, J., Zhang, Q., Chen, Z. and Zheng, Z., *The effects of EGR rates and ternary blends of biodiesel/n-pentanol/diesel on the combustion and emission characteristics of a CRDI diesel engine*. Fuel, 2021, **286:** p. 119297.
20. Cornils, B., *Handbook of Commercial Catalysts. Heterogeneous Catalysts. By Howard F. Rase.* 2004, Wiley Online Library.
21. Liu, K.H., Atiyeh, K., Stevenson, B. S., Tanner, R. S., Wilkins, M.R. and Huhnke, R.L., *Continuous syngas fermentation for the production of ethanol, n-propanol and n-butanol.* Bioresource Technology, 2014, **151**: p. 69-77.
22. Kumar, B.R. and Saravanan, S., *Use of higher alcohol biofuels in diesel engines: A review*. Renewable and Sustainable Energy Reviews, 2016, **60**: p. 84-115.
23. Venkata Rao, K. and Murthy, P., *Modeling and optimization of tool vibration and surface roughness in boring of steel using RSM, ANN and SVM*. Journal of Intelligent Manufacturing, 2018, **29**(7): p. 1533-1543.
24. Xu, Z., Kang, Y. and Lv, W., *Analysis and prediction of vehicle exhaust emission using ANN.* 36th Chinese Control Conference. 2017. IEEE. p. 4029-4033.
25. Abuhabaya, A., Ali, J., Fieldhouse, J., Brown, R. and Andrijanto, E., The optimisation of bio-diesel production from Sunflower oil using RSM and its effect on engine performance and emissions. 36th Chinese Control Conference. 2011. IEEE. p. 310-314.
26. Baranitharan, P. Ramesh, K. and Sakthivel, R., *Measurement of performance and emission distinctiveness of Aegle marmelos seed cake pyrolysis oil/diesel/TBHQ opus powered in a DI diesel engine using ANN and RSM*. Measurement, 2019, **144**: p. 366-380.
27. Ghanbari, M., Mozafari-Vanani, L., Dehghani-Soufi, M. and Jahanbakhshi, A., *Effect of alumina nanoparticles as additive with diesel–biodiesel blends on performance and emission characteristic of a six-cylinder diesel engine using response surface methodology (RSM).* Energy Conversion and Management: X, 2021, **11**: p. 100091.
28. Rao, K.P., Babu, T.V., Anuradha, G., and Rao, B.V.A., *IDI diesel engine performance and exhaust emission analysis using biodiesel with an artificial neural network (ANN).* Egyptian Journal of Petroleum, 2017, **26**(3): p. 593-600.
29. Yilmaz, N., Atmanli, A., Hall, M. J. and Vigil, F. M., *Determination of the optimum blend ratio of diesel, waste oil derived biodiesel and 1-pentanol using the response surface method.* Energies, 2022, **15**(14): p. 5144.
30. Caligiuri, C., Bietresato, M., Algieri, A., Baratieri, M. and Renzi, M., *Experimental Investigation and RSM Modeling of the Effects of Injection Timing on the Performance and NOx Emissions of a Micro-Cogeneration Unit Fueled with Biodiesel Blends.* Energies, 2022, **15**(10): p. 3586.
31. Ong, M.Y., Nomanbhay, S., Kusumo, F., Raja Shahruzzaman, R.M.H. and Shamsuddin, A.H., *Modeling and optimization of microwave-based bio-jet fuel from coconut oil: Investigation of Response Surface Methodology (RSM) and Artificial Neural Network Methodology (ANN).* Energies, 2021, **14**(2): p. 295.
32. Simsek, S. and Uslu, S., *Determination of a diesel engine operating parameters powered with canola, safflower and waste vegetable oil based biodiesel combination using response surface methodology (RSM)*. Fuel, 2020, **270**: p. 117496.
33. Kumar, B.R., Saravanan, S., Rana, D. and Nagendran, A., *Combined effect of injection timing and exhaust gas recirculation (EGR) on performance and emissions of a DI diesel engine fuelled with next-generation advanced biofuel–diesel blends using response surface methodology.* Energy Conversion and Management, 2016, **123**: p. 470-486.
34. Uysal, A. and Bayir, R., *Real-time condition monitoring and fault diagnosis in switched reluctance motors with Kohonen neural network.* Journal of Zhejiang University Scıence C, 2013, **14**: p. 941-952.
35. Saritas M.M., and Yasar, A., *Performance analysis of ANN and Naive Bayes classification algorithm for data classification.* International Journal Of Intelligent Systems and Applications in Engineering, 2019, **7**(2): p. 88-91.
36. Hao, D., Mehra, R.K., Luo, S., Nie, Z., Ren, X. and Fanhua, M., *Experimental study of hydrogen enriched compressed natural gas (HCNG) engine and application of support vector machine (SVM) on prediction of engine performance at specific condition.* International Journal of Hydrogen Energy, 2020, **45**(8): p. 5309-5325.
37. Zou, J., Han, Y. and So, S.S., O*verview of Artificial Neural Networks*. 2008, **458:** Humana Press.
38. Uslu, S. and Celik, M.B., *Performance and exhaust emission prediction of a SI engine fueled with I-amyl alcohol-gasoline blends: an ANN coupled RSM based optimization*. Fuel, 2020, **265**: p. 116922.
39. Bayir, R. and Soylu, E., *Real time determination of rechargeable batteries' type and the state of charge via cascade correlation neural network.* Elektronika Ir Elektrotechnika, 2018, **24**(1): p. 25-30.
40. Oğuz, H., Sarıtas, I., and Baydan, H.E., Prediction of diesel engine performance using biofuels with artificial

neural network. Expert Systems with Applications, 2010, **37**(9): p. 6579-6586.

41. Tasdemir, S., Saritas, I., Ciniviz, M. and Allahverdi, N., *Artificial neural network and fuzzy expert system comparison for prediction of performance and emission parameters on a gasoline engine.* Expert Systems with Applications, 2011, **38**(11): p. 13912-13923.
42. Singh, Y., Sharma, A., Singh, G.K., Singla, A. and Singh, N.K., *Optimization of performance and emission parameters of direct injection diesel engine fuelled with pongamia methyl esters-response surface methodology approach*. Industrial Crops and Products, 2018, **126**: p. 218-226.
43. Karagöz, M., ANN based prediction of engine performance and exhaust emission responses of a CI engine powered by ternary blends. International Journal of Automotive Science And Technology, 2020, **4**(3): p. 180-184.
44. Yusaf, T.F., Buttsworth, D., Saleh, K.H., and Yousif, B., *CNG-diesel engine performance and exhaust emission analysis with the aid of artificial neural network.* Applied Energy, 2010, 87(5): p. 1661-1669.
45. Ramesh, K., Alwarsamy, T., and Jayabal, S., *Prediction of cutting process parameters in boring operations using artificial neural networks.* Journal of Vibration and Control, 2015, **21**(6): p. 1043-1054.
46. Kurtgoz, Y., Karagoz, M. and Deniz, E., Biogas engine performance estimation using ANN. Engineering SScience and Technology, an International Journal, 2017, **20**(6): p. 1563-1570.
47. Krishnamoorthi, M., Malayalamurthi, R. and Shameer, P.M., *RSM based optimization of performance and emission characteristics of DI compression ignition engine fuelled with diesel/aegle marmelos oil/diethyl ether blends at varying compression ratio, injection pressure and injection timing.* Fuel, **221:** p. 283-297.
48. Awada, O.I., Mamat, R., Obed M. A. Azmi, W.H., Kadirgama, K., Yusri, I.M., Leman, A.M. and Yusaf, T., Response surface methodology (RSM) based multi-objective optimization of fusel oil-gasoline blends at different water content in SI engine. Energy Conversion and Management, 2017, **150**: p. 222-241.
49. Shameer, P.M. and Ramesh, K., *Influence of antioxidants on fuel stability of Calophyllum inophyllum biodiesel and RSM-based optimization of engine characteristics at varying injection timing and compression ratio*. Journal of the Brazilian Society of Mechanical Sciences and Engineering, 2017, **39**: p. 4251-4273.
50. Dubey, A., Prasad, R.S., Singh, J.K., and Nayyar, A., *Optimization of diesel engine performance and emissions with biodiesel-diesel blends and EGR using response surface methodology (RSM).* Cleaner Engineering and Technology, 2022, **8**: p. 100509.
51. Simsek S. and Uslu, S., *Investigation of the effects of biodiesel/2-ethylhexyl nitrate (EHN) fuel blends on diesel engine performance and emissions by response surface methodology (RSM).* Fuel, 2020, **275**: p. 118005.
52. Simsek, S., Uslu, S., and Simsek, H., *Response surface methodology-based parameter optimization of single-cylinder diesel engine fueled with graphene oxide dosed sesame oil/diesel fuel blend.* Energy and AI, 2022, **10**: p. 100200.

Available online at www.dergipark.org.tr/en

INTERNATIONAL ADVANCED RESEARCHES and ENGINEERING JOURNAL

Journal homepage: www.dergipark.org.tr/en/pub/iarej

e-ISSN: 2618-575X

International Open Access

Volume 07
Issue 03

December, 2023

Research Article

Hydrodynamic behaviour improvement of check valves through CFD analysis

Erhan Ozkan [a,*]

[a]*Dikkan R&D Center, Izmir 35370, Turkey*

ARTICLE INFO

Article history:
Received 02 August 2023
Accepted 05 December 2023
Published 15 December 2023

Keywords:
CFD
FEA
Hydrodynamic
Valve

ABSTRACT

In this article, the computer assisted design, flow simulation, optimization of production parameters and unique design prototype manufacturing of a check valve with 16 bar pressure, 5 m/s flow rate and 52000 m^3/h flow coefficients, which have never been achieved before in the valve sector, were presented to the attention of the readers. Check valves have a critical role that do not allow reverse flow of the fluid passing through them and are generally designed to secure the pipeline. A small mistake in design may cause great damage in the system. For this reason, a new product of which the disc material exposed to 5 m/s fluid velocity, the body subjected to 16 bar pressure and the system with a flow coefficient of 52000 m^3/h were designed by the SolidWorks, the flow was simulated with CFD (Computational Fluid Dynamics), and the mechanical resistance was analysed by FEA (Finite Element Analysis). Fluent, CFD and mechanical modules of ANSYS were used to define the parameters of the design. The manufactures of the products designed in the computer environment have been produced by casting method with a 45% ferritic microstructure and impact resistance twice as high as the standard requirements have been implemented.

1. Introduction

Check valves are one-way safety valves that prevent the fluids passing through the installation from moving in one direction and returning, thus allowing the system to operate more efficiently [1]. Check valves are simple devices. They perform a vital function by preventing reverse flow. Possible reverse flow in the system can often cause damage or malfunction to other equipment connected to the installation, such as valves and pumps [2]. Even if there is no malfunction, it may cause loss of system integrity. The operation of the check valve, which has a single inlet and outlet, is based on pressure difference. The valve opens when the pressure from the inlet side is greater than the pressure from the outlet side. If the pressure in the inlet direction is lower than the pressure in the outlet direction, it closes, and the fluid is prevented from returning [3]. Check valves do not require a lever, actuator, or human power, unlike the opening and closing principle of other valve types. Closing and opening is completely automatic [4-7].

There are more than one check valve type depending on the system in which it will be used. The selection should be made according to factors such as type of fluid, operating method, installation direction, maximum pressure, connection point, temperature, closing speed. The main types are swing check valve, wafer check valve, spring check valve, tilting check valve, ball check valve, dual check valve [8-12].

A check valve requires a minimum pressure between the inlet and outlet to operate [13-16]. This lowest pressure, which causes the valve to open, is called cracking pressure. This required minimum pressure varies depending on the size and design of the check valve [17]. When choosing a check valve, it should be noted that the system can produce this pressure [18].

If the flow pressure in the system drops below the separation pressure or a reverse flow occurs, the check valve will close. The closing mechanism inside the check valve varies depending on the type [19]. In all cases, the mechanism inside the check valve will prevent backflow and provide sealing [20].

As the they operate through a single way, it is very important to install them in the correct direction to the installations to be used [21]. If installed in the opposite direction, flow will stop and cause pressure build-up. This causes damage to other hardware in the system. There is a mark on each valves indicating the flow direction [22].

* Corresponding author. Tel.: +90-232-877-17-14; Fax: +90-232-877-17-15.
E-mail addresses: erhan.ozkan@dikkan.com *(E. Ozkan)*
ORCID: 0000-0002-3849-6713
DOI: 10.35860/iarej.1336567 *(E. Ozkan)*

There are some points to consider when choosing a check valve. The most important of these criteria are connection type (flange, threaded, grooved, etc.), highest pressure and lowest separation pressure, horizontal or vertical installation direction, size, material compatibility, internal and external temperature, easy access for repair [23].

Fluid characterization has a critical role to define the check valve design parameters. CFD (computational fluid dynamics) analysing programs and simulations are often used for this purpose. CFD is a branch of fluid mechanics in which numerical methods and algorithms are used to analyse and solve fluid mechanics problems. The interactions of liquids and gases with solid surfaces are simulated with the help of computers [24,25]. The state of the results relative to the actual interaction depends on the performance of the computer or computers used. When the complex geometries, viscosity, temperature differences factors are applied to the fundamental equations of classical fluid mechanics, the solution is very difficult, even often impossible. In classical fluid mechanics, results can only be achieved in idealized simple geometries such as flat plates and pipes with circular cross-sections. CFD is required to obtain results in 99% of the remaining real problems such as lack of fluid, transition from laminar into the turbulence characteristic, deviation from the steady state condition. For this, the flow region is divided into a network of small regular elements and points simulating the basic differential equations of the flow, and the whole solution is reached step by step from these small elements with iterations [25-28].

In this article, studies on the development of a prototype, which has never been done before, that can operate at high flow loss coefficients provided by disc, which is a mechanical component used in check valves to control the flow speed, dimensions determined by analysing in computer-aided design and simulation environment and at the same time allow double-time closure with a different piston design were presented in detail. At the same time, details of the challenges addressed by the new prototype developed and how it compares with existing solutions were presented. With the prototype developed by CFD and FEA (finite element analysis), a product with increased disc strength, optimized valve weight and reduced energy losses by minimizing resistance to flow is designed. With the intensive use of simulation techniques, the competitive conditions of environmentally friendly and highly efficient valves have been improved and an innovative product has been introduced. The unique aspect of this study is that, unlike existing studies in the literature, the production and characterization of check valves were presented together using CFD analysis and simulation-supported designs with different parameters.

2. **Materials and Methods**

2.1 Design and Simulation

CFD is the design and analysis method commonly used in the valve industry. In this way, 3-dimensional flows inside the valve were simulated using various equations that describe the flow conditions. Its importance for designers is that all analyses can be carried out in a virtual environment before the prototype is produced. In this way, it will be ensured that the product can be transferred to rapid environmental conditions on the right basis the first time, with less labour and material loss. The three-dimensional designs of the products were made with the Solidworks drawing program. ANSYS computer aided simulation program was used for CFD analysis and FEA. In CFD analysis, it was solved with the K-epsilon turbulence model, and improvements were made in the boundary layers and mesh by keeping the y+ value at 3 and below. This model is the most widely used turbulence model and is mainly used for simple turbulent flows. It calculates the relationship between the kinetic energy of the fluid and the dispersed turbulent kinetic energy.

The strength values of the valve designed in FEA were determined according to the boundary conditions defined in the *EN 1074* standard. The parts were handled with two different numerical methods, singular and assembled, and interpolation solution was realized with the Rayleigh-Ritz method. It is important to consider the structural damping effects of the system in dynamic analyses. The structural damping coefficient, which is generally defined as a constant coefficient in static analyses, is defined by calculating it separately for the mass and stiffness matrices in dynamic analyses. In order to orient the mass and stiffness matrices correctly, Rayleigh damping coefficients were calculated and transferred to the system. The boundary conditions specified in the standard were applied exactly and were defined as one and a half times the nominal pressure value for the body part and ten percent more than the nominal pressure value for the disc part. With the results obtained from this stage, the material analysis and selection stage were started.

2.2 Material Selection and Justification

While modelling the body part in contact with the fluid, a body material that can withstand one and a half times the body pressure was selected regarding the analyses made according to *EN 12266* and *EN 1074* standards. The disc material that would withstand ten percent of the pressure value was selected by the same method, and the material was chosen regarding to the stresses and deformation results in the parts according to the body and disc strength analyses. Considering the FEA results, *EN GJS 400-15* (also defined as *GGG 40*) material was selected regarding to its high

strength. The main reason for the high mechanical strength of *EN GJS 400-15* material was to obtain a ferritic microstructure. The carbon dissolved in the austenite phase was in the form of spherical graphite dispersed in the ferritic microstructure. The samples were produced by sand mould casting method at 1465 °C with 30% dkp steel, 30% ductile iron, and 40% runner ratio.

2.3 Sample Production and Testing

Chemical analysis of the casting material was carried out with Metavision 1008 brand spectrometer. The mechanical properties of the samples were determined by notch impact and tensile tests. The samples prepared for the notch impact test were tested with an OTTO WOLPERT WERKE PW 30/15 brand machine located in the R&D Center at a temperature of 25 °C, and the samples prepared for the tensile test were tested at room temperature with an OTTO WOLPERT U-40 type tensile device. The main reason for choosing this equipment was that they enable precise measurements to be made easily.

2.4 Microstructural Analysis

The samples, which were fixed into polyester moulds for microstructural analysis, were grinded and polished with the STRUERS Tegrapol-21 brand grinding and polishing device by turning 90° each time with 600 grades SiC sandpaper, 220 grade 9 µm, 3 µm and 1 µm felt and diamond pastes, respectively, and made ready for the etching process. Prepared samples for the microstructure analyses were etched with 3% Nital solution. The samples were investigated with a 1000 magnification NIKON ECLIPSE LV 150 optical microscope. The hardness values were tested at room temperature with an ALBERT GNEHM brand universal hardness measuring machine with Brinell tip. It was possible to conduct more detailed research with these devices.

2.5 Hydrodynamic Tests

The hydrodynamic tests of the produced body and mounted disc were carried out according to EN 1074 standard. Regarding to the definition of this standard, pressure tests were evaluated for the body under 16 bar pressure without showing the leakage and damage on the valve. The reason to choose this procedure was to evaluate the hydrodynamic behaviour of the check valves on the tough environment.

3. Results and Discussion

One of the most important steps in performing CFD analyses properly is to define and handle the data correctly, and more detailed data about the line and fluid is needed. Therefore, the technical details targeted in the article for the CFD analyses in line with the requirements defined in the *EN 1267* and *EN 1074* standards are given in Table 1.

The parameter that would support the velocity vector analysis of this system should be its characteristic behaviour under 16 bar pressure, and velocity vector analysis was carried out. Accordingly, when the disc was in the fully open position, the resistance of the disc and the body against flow could be characterized more clearly. Innovative design trials have been carried out to suit the desired conditions. Figure 1 shows the velocity vector analysis of the system under 5 m/s. According to the research in the literature, it has been determined that there are factors that disrupt laminar flows, sharp surface change, temperature change and material resistance in valve disc materials [29-31]. As a result of these evaluations, the methodology proved effective in the CFD analysis of the disc material at a flow rate of 5 m/s, and it was observed that the flow lines were suitable in green colour.

Table 1. Technical properties of the design inputs

Line Pressure (Bar)	16
Fluid Velocity (m/s)	5.0
Flow Coefficient (m^3/h)	52000

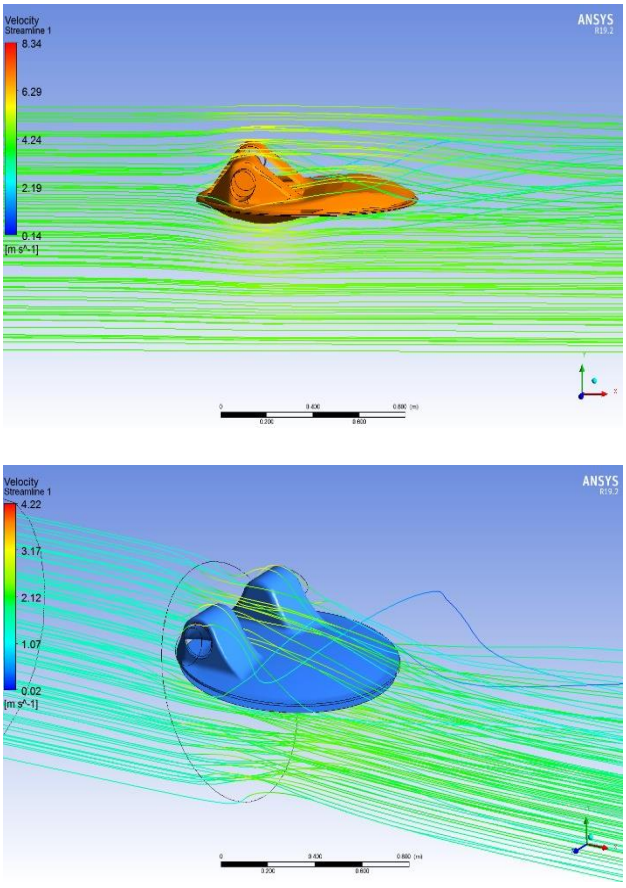

Figure 1. Velocity vector analyses of the design for front (upper) and isometric (below) views

In order to increase the desired flow coefficient, in other words, the valve efficiency, various designs have been made in the disc geometry. The mechanical numerical analysis method was carried out by defining the boundary condition of ten percent of the nominal pressure for the disc materials, which were carried out by considering the yield strength values of 240 MPa. Accordingly, the mechanical analysis of the disc regarding to 18 bar, which corresponds to 1.1 times the maximum working pressure of 16 bar, is shown in Figure 2. The design developed to increase the mechanical strength of the disc exposed to the flow surface was defined by FEA and no red areas, which represent high stress zone encouraging plastic deformation, were observed.

The assembly of body, disc, and shaft materials by using the Solidworks design program and simulations by the help of ANSYS FEA are shown in Figure 3. In this Figure (a) represents the body, disc, and shaft assembly. (b) expresses disc material's and (c) expresses shaft material's mechanical strength by FEA analysis. The most important issue here would be that no plastic deformation was observed in the designs. While elastic deformation regions are defined in green, high plastic deformation is observed in the regions defined in red. In this case, the material will exhibit irreversible defects and will dangerously fail in application. According to the results obtained, the absence of red areas indicates that there was no plastic deformation in all of the components, and the results achieved were satisfactory.

The final version of the solid models of the designs before casting was realized with the help of Solidworks drawing program and the final version was decided (Figure 4). The most important advantage of this stage is to show that 3D designs of products can be made on a component basis according to exact measurements. This allows designers to quickly make final revisions of the product before the prototype goes into production.

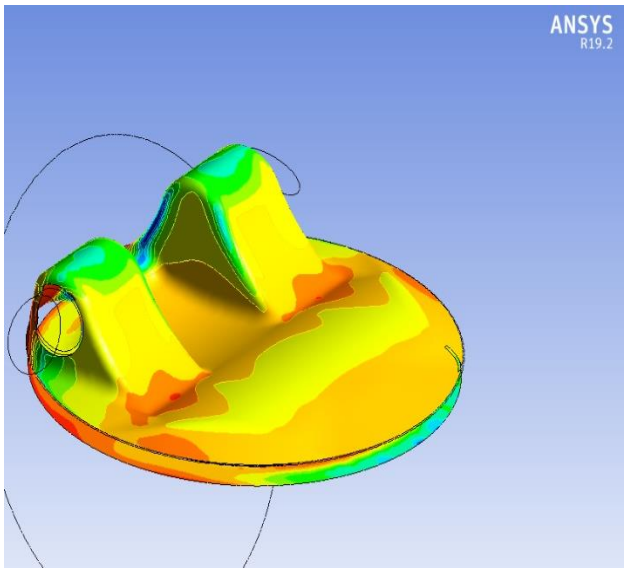

Figure 2. Mechanical strength definition by FEA

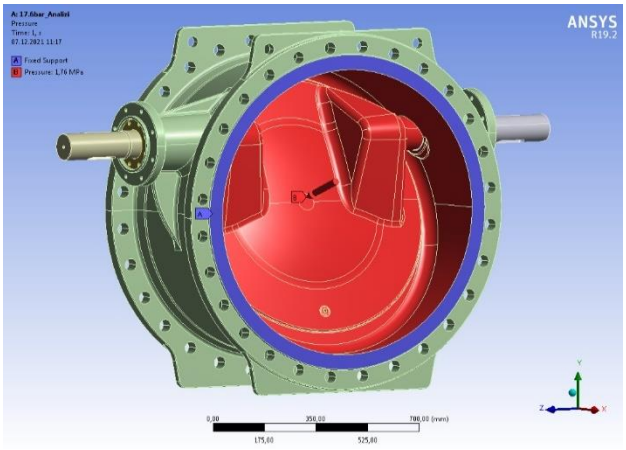

a

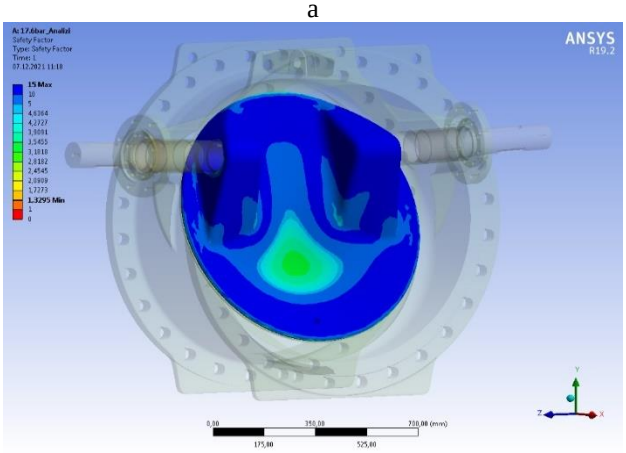

b

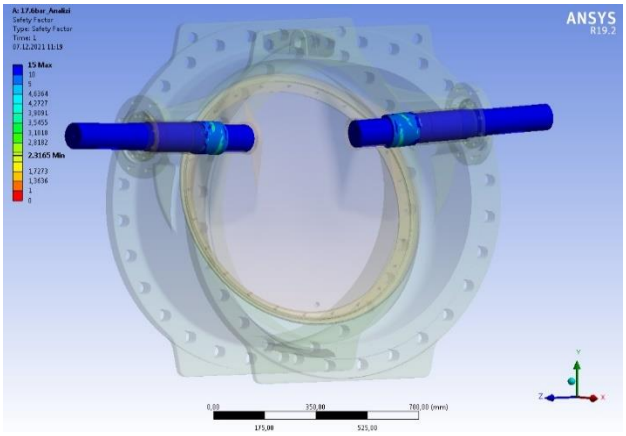

c

Figure 3. Assembled body, disc, and shaft's FEA analysis

The casting models of the disc and body materials, which were designed by analysing their hydrodynamic properties, and the production of the core box were carried out on CNC machines with CAM software. The wooden models' productions of the valve components are shown in Figure 5. The use of CAD-CAM applications gives accurate results when used for CNC milling. This results in a significant increase in accuracy. In this sense, it greatly increases control over the production process. Using CAD-CAM engineering helps save time at every stage, meaning prototypes and finished products can be produced much faster. Improved accuracy and time savings also have an important benefit today: It reduces costs.

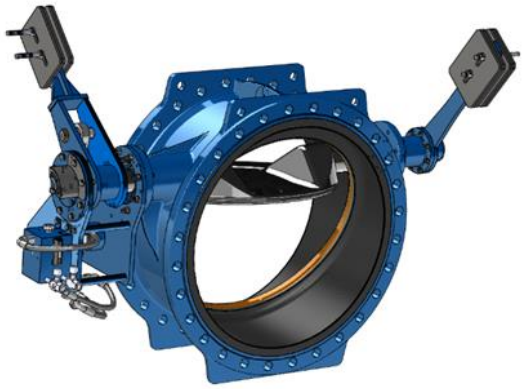

Figure 4. Final version design made by Solidworks

Figure 5. Pre-cast preparations of components' material

The four main factors controlling the microstructure in cast irons are carbon content, alloying element, solidification during and after solidification cooling rate and after casting heat treatments. What makes these stages important are carbon and phosphorus analyse with manganese and silicon values. The final chemical of the parts that were the subject of the study analysis values are shown in Table 2. As can be seen in the chemical composition, ferrite levels of the building elements perlite phase in the structure affects the amount of formation. Obtaining a completely pearlitic structure, the silicon content must be low, where the manganese rate has to be high. However, since there was no need for a full pearlitic structure in this study, cast iron products containing 2-4% carbon, 0.4-3% silicon, 0.4 - 0.8% manganese and 0.1 - 0.8% phosphorus were preferred. This also fulfilled the requirement of the general used cast iron products.

Microstructure, hardness, shrinkage over the cast part obtained after the applications of the production processes strength, % elongation, notch impact tests were performed. These tests were taken from the cast part itself applied to the samples. Figure 6 shows the microstructure images. According to the literature, it was expected to have a high ferrite content and a homogeneous distribution of sphericity. Regarding to the etched microstructure image with homogeneously distributed graphite with 45% ferrite was obtained [32,33].

Considering the literature research and standard scans, it is appropriate that the yield strength of the product is 200 N/mm^2 and the tensile strength is 300 N/mm^2. As a result of this study, 250 N/mm^2 yield strength and 400 N/mm^2 tensile strength were obtained and ideal conditions were provided. On the other hand, micro hardness values should be 130-175 HB and Charpy impact test values must be minimum 12 Joule at the room temperature. As the mechanical test results given in the Table 3, it was observed that the mechanical values fulfilled the requirements of the standards [34,35].

The visual of the prototype production, which has been casted, assembled, and ready for the hydrodynamic test, is given in the Figure 7. When the water flow starts, the check valve flap is pushed by the pushing force of the water and continues its flow towards the direction of the water flow. When the water flow stops, the valve starts to close. The check valve closes with the help of the weight attached to the flap shaft and the pushing force of the returning water. It prevents water from returning to the floodplain or flow line. It has been observed that the design carried out in the solid model and the prototype production exactly overlap.

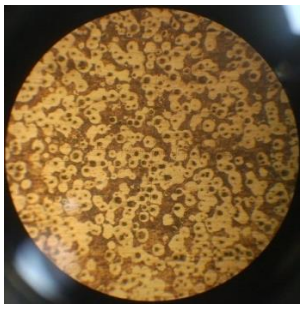

Figure 6. Casting material etched microstructure image

Table 2. The mechanical analyses of the disc, body, and shaft materials

Yield Strength (N/mm^2)	Tensile Strength (N/mm^2)	Elongation (%)	Hardness (HB)	Charpy (Joule)	Structure
250	400	18	150	23	Ferritic

Figure 7. Prototype production of the developed design

Figure 8. Hydrodynamic test equipment

The pressure tests of the produced body and the assembled disc were carried out according to defined standard conditions. Materials in contact with water intended for human consumption must comply with the requirements of national regulations in the country of use and must not affect the water in any way. This means that the chemistry and physical appearance of the water should not change after contact with a valve – you should not see, smell, feel or taste any difference in the water. Additionally, all interior and exterior materials must be resistant to corrosion or protected by appropriate means. Pressure tests were evaluated for the body under a pressure of 16 bar without the leakage and damage on the valve. The design in which the pressure test was performed is given in the Figure 8.

4. Conclusions

As a result of the analyses, simulations, prototype production and hydrostatic tests, a unique check valve article was presented for the first time in the industry. The project has been a guide in improving and developing the product geometry for the final goal, with various and repetitive applications on flow analysis. At the same time, it has been satisfactory that the needs can be met with the mechanical auxiliary equipment applied. With this completed project, R&D capability for the design of variant products has been increased and national and international patent applications have been made for the curved body and stepped shaft of the product that is the output of this project. Regarding this design, R&D Innovation Project has also been successfully concluded.

As a result of simulation analyses in products designed for use in fluid lines, no turbulent flow was observed at a flow rate of 5 m/s and an ideal laminar flow was determined. These results were validated by hydrostatic tests and verified by leak tests.

Simulation studies were carried out in such a way that the fluid coefficient was 52000 m^3/hour when the valve was in the fully open position under 16 bar pressure and 5 m/s fluid velocity, which were fulfilled the requirements of the *EN 1267* and *EN 1074* standards.

No defects were detected in the casting of the valve components and 45% ferritic structure was obtained. In the ferritic structure, it takes time for all the carbon dissolved in the austenite to turn into spherical graphite required. This microstructure of the material consists of randomly dispersed spherical graphite, which causes high impact strength, high hardness, and convenient tensile test results. The casted components were showed twice Charpy impact strength resistance than required and met the tensile-hardness tests standards requirements.

In final summary, the check valve with %45 ferritic structure, resistant to the 52000 m^3/hour fluid coefficient, exposed to the flow tests with 5 m/s fluid velocity was designed successfully. The acceptance tests were carried out according to a minimum yield strength of 240 N/mm^2 in the body design, no adverse events were detected under 16 bar and no plastic deformation occurred in the product under 24 bar pressure.

This research serves as a guide for improving product geometry through flow analysis. It has been satisfactory that the needs can be met with the applied mechanical auxiliary equipment. It has increased its R&D capability for similar products to be produced. The product that is the subject of the article is a design, which has the potential for commercialization, as it will increase the manufacturability of the companies and then the same or similar ones can be made within the needs.

Declaration

The author declared no potential conflicts of interest with respect to the research, authorship, and/or publication of this article. The author also declared that this article is original, was prepared in accordance with international publication and research ethics, and ethical committee permission or any special permission is not required.

Author Contributions

Erhan Ozkan developed the methodology, performed the analysis, and wrote the manuscript.

Acknowledgment

This study supported by Dikkan Research Program at the R&D Center approved by Industry and Technology Minister, Turkey.

References

1. Pibarot, P., H.C. Herrmann, C. Wu, R. T. Hahn, C. M., Otto, and A. E. Abbas, *Standardized definitions for bioprosthetic valve dysfunction following aortic or mitral valve replacement: JACC state-of-the-art review*. Journal of the American College of Cardiology, 2022. **80**.5: p. 545-561.
2. Dikshit, A., A. E. Anikanov, P. Petukhov, A. Rudic, G. Woiceshyn, and C. Jurgensen, Sand Screen with Check-Valve Inflow Control Devices. SPE Drilling & Completion, 2020. **35**.04: p. 707-713.
3. Pan, Q. H., Z. Huang, B. Huang, R. Li, B. Wang, and Z. Feng, *Development of a piezoelectric pump with ball valve structure*. Journal of Intelligent Material Systems and Structures, 2021. **32**.18-19: p. 2289-2299.
4. Jung, C. and J. K. Sung, *Investigation into the effects of passive check valves on the thermal performance of pulsating heat pipes.* International Journal of Heat and Mass

Transfer, 2023. **204:** 123850.

5. Li, S. T., H. Shen, M. Yu, and Z. Lei, *Analysis and Optimization of the Opening Dynamic Characteristics of Molten Salt Check Valves for Concentrating Solar Power.* Applied Sciences, 2023. **13**.5: 3146.
6. Kim, N. and J. Yong-Hoon, *An investigation of pressure build-up effects due to check valve's closing characteristics using dynamic mesh techniques of CFD.* Annals of Nuclear Energy, 2021. **152**: 107996.
7. Mao, Z., Y. Kazuhiro, and K. Joon-wan, *A micro vertically-allocated SU-8 check valve and its characteristics.* Microsystem Technologies, 2019. **25**: p. 245-255.
8. Li, S. T., H. Shen, M. Yu, and Z. Lei, *Analysis and Optimization of the Opening Dynamic Characteristics of Molten Salt Check Valves for Concentrating Solar Power.* Applied Sciences, 2023. **13**.5: p. 3146.
9. Zhao, R., L. Weihua, and Z. Weilin, *Unsteady characteristic and flow mechanism of a scroll compressor with novel discharge port for electric vehicle air conditioning.* International Journal of Refrigeration, 2020. **118**: p. 403-414.
10. Shoykhet, K., B. Ken, and W. D. Michael, *Modern HPLC pumps: perspectives, principles, and practices.* LC GC North America, 2019. **37**.6: p. 374-384.
11. Qian, J., C. W. Hou, X. J. Li, and Z. J. Jin, *Actuation mechanism of microvalves: A review.* Micromachines, 2020. **11**.2: p. 172.
12. Chamas, A., L. Qi, H. S. Mehta, J. A. Sears, S. L. Scott, E. Walter, and D. W. Hoyt, *High temperature/pressure MAS-NMR for the study of dynamic processes in mixed phase systems.* Magnetic Resonance Imaging, 2019. **56**: p. 37-44.
13. Birkitt, K., K. Loo-Morrey, M. C. Sanchez, and L. O'Sullivan, *Materials aspects associated with the addition of up to 20 mol% hydrogen into an existing natural gas distribution network.* International Journal of Hydrogen Energy, 2021. **46**.23: p. 12290-12299.
14. Lin, Z., X. Sun, T. Yu, Y. Zhang, Y. Li, and Z. Zhu, *Gas–solid two-phase flow and erosion calculation of gate valve based on the CFD-DEM model.* Powder Technology, 2020. **366:** p. 395-407.
15. Filo, G., L. Edward. and R. Janusz, *Design and flow analysis of an adjustable check valve by means of CFD method.* Energies, 2021. **14**.8: p. 2237.
16. Żyłka, M., N. Marszałek. and W. Żyłka, *Numerical simulation of pneumatic throttle check valve using computational fluid dynamics (CFD).* Scientific Reports, 2023.**13**(1): p. 2475.
17. Bhowmik, P. K. and Y. S. Kune, *Flow mapping using 3D full-scale CFD simulation and hydrodynamic experiments of an ultra-supercritical turbine's combined valve for nuclear power plant.* International Journal of Energy and Environmental Engineering, 2021. **12**.3: p. 365-381.
18. Szpica, D., G. Mieczkowski, A. Borawski, V. Leisis, S. Diliunas, and T. Pilkaite, *The computational fluid dynamics (CFD) analysis of the pressure sensor used in pulse-operated low-pressure gas-phase solenoid valve measurements.* Sensors, 2021. **21**.24: p. 8287.
19. Žic, E., B. Patrik. and L. Luka, *Hydraulic analysis of gate valve using computational fluid dynamics (CFD).* Scientific Review Engineering and Environmental Sciences, 2020. **29**.3: p. 275-288.
20. Imam, H., M. Sabreen, K. Pibars, and W. M. M. Soltan. *Studying the hydraulic characteristics of UPVC butterfly valve by CFD technique.* Plant Archives, 2019. **19**.2: p. 377-383.
21. Buczkowski, D. and G. Nowak. *Increase in tuning ability of a car shock absorber valve using CFD.* Journal of Applied Fluid Mechanics, 2019. **12**.6: p. 1847-1854.
22. Jakobsen, J. H. and R. H. Michael, *CFD assisted steady-state modelling of restrictive counterbalance valves.* International Journal of Fluid Power, 2020. p. 119-146.
23. Cao, Y., L. Zhou, C. Ou, H. Fang, and D. Liu, *3D CFD simulation and analysis of transient flow in a water pipeline.* AQUA—Water Infrastructure, Ecosystems and Society, 2022. **71**.6: p. 751-767.
24. Zhang, Z., J. Li. and Y. Lixin, *Numerical simulation study on the opening process of the atmospheric relief valve.* Nuclear Engineering and Design, 2019. **351**: p. 106-115.
25. Yedekçioğlu, F., S. Akyıldız, and Z. Parlak, *Numerical investigation of aerodynamic performance and noise characteristic of air multiplier bladeless fan.* International Advanced Researches and Engineering Journal, 2023. p. 13-22.
26. Arsenoaia, V., V. Vlâduţ, I. Ţenu, I. Voicea, G. Moiceanu, and, P. M. Cârlescu, *Mathematical Modeling and Numerical Simulation of the Drying Process of Seeds in a Pilot Plant.* INMATEH-Agricultural Engineering, 2019. **57**(1): p. 55-62.
27. Malekjani, N. and S.M. Jafari, *Simulation of food drying processes by Computational Fluid Dynamics (CFD); recent advances and approaches.* Trends in Food Science & Technology, 2019. **78:** p. 206-223.
28. Filo, G., L. Edward, and R. Janusz, *Flow analysis of a switching valve with innovative poppet head geometry by means of CFD method.* Flow Measurement and Instrumentation, 2019. **70**: p. 101643.
29. Guzei, D. V., A. V. Minakov, and V. Y. Rudyak, *On efficiency of convective heat transfer of nanofluids in laminar flow regime.* International Journal of Heat and Mass Transfer, 2019. **139**: p. 180-192.
30. Li, R., Q. Huang, F. Huo, K. Fan, W. Li, and D. Zhang, *Effect of shear on the thickness of wax deposit under laminar flow regime.* Journal of Petroleum Science and Engineering, 2019. **181**: p. 106212.
31. Shi, H., N. D. M. Raimondi, D. F. Fletcher, M. Cabassud, and C. Gourdon, *Numerical study of heat transfer in square millimetric zigzag channels in the laminar flow regime.* Chemical Engineering and Processing-Process Intensification, 2019. **144**: p. 107624.
32. Cruz, R., A. Alejandro, G. E. Colin, R. J. Téllez, and H. A. Magaña, *Performance Evaluation of Austempered Ductile Iron Camshaft Low Alloyed with Vanadium on an Electric Spin Rig Test.* Metals, 2023. **13**.2: p. 198.
33. Franzen, D., P. Björn, and B. P. Andreas, *Influence of graphite-phase parameters on the mechanical properties of high-silicon ductile iron.* International Journal of Metalcasting, 2023. **17**.1: p. 4-21.
34. Upadhyay, S. and K. S. Kuldeep, *Effect of Cu and Mo addition on mechanical properties and microstructure of grey cast iron: An overview*. Materials Today: Proceedings, 2020. **26**: p. 2462-2470.
35. Li, Y., S. Dong, P. He, S. Yan, E. Li, X. Liu, and B. Xu, *Microstructure characteristics and mechanical properties of new-type FeNiCr laser cladding alloy coating on nodular cast iron*. Journal of Materials Processing Technology, 2019. **269**: p. 163-171.

Available online at www.dergipark.org.tr/en

INTERNATIONAL ADVANCED RESEARCHES and ENGINEERING JOURNAL

Journal homepage: www.dergipark.org.tr/en/pub/iarej

e-ISSN: 2618-575X

International Open Access

Volume 07
Issue 03

December, 2023

Research Article

Investigation of mechanical properties and damage types of E-glass fiber reinforced epoxy matrix composites under various loadings

Ali İmran Ayten [a]

[a]*Yalova University, Faculty of Engineering, Department of Polymer Materials Engineering, Yalova, 77200, Turkey*

ARTICLE INFO

Article history:
Received 30 July 2023
Accepted 31 October 2023
Published 15 December 2023

Keywords:
Damage mechanisms
E-glass
Mechanical characterization
Thermoset composites

ABSTRACT

This study presents a comprehensive experimental investigation to determine the elastic material properties of a unidirectional E-glass fiber/epoxy composite. Tension, compression, in-plane shear, and flexural tests were conducted in both longitudinal and transverse directions. The composite laminates were manufactured using vacuum-assisted resin transfer molding (VARTM) with a 65% fiber weight fraction. Mechanical tests were performed according to ASTM standards, and special fixtures were used for shear and compression tests. The damage mechanisms were interpreted for each test, revealing fiber splitting in tension and kink band failure in compression were dominant damage modes. The findings provide valuable insights into the behavior and performance of the composite under various loading conditions, which may help in its application in different engineering fields.

1. Introduction

Polymer matrix composites find widespread utilization in various fields like aerospace, automotive, marine, and defense due to their remarkable properties, including high stiffness and strength-to-weight ratio, low density, and exceptional impact resistance [1-5]. Moreover, these composites offer design flexibility through options like fiber orientation [6], hybridization variations [7-11], and stacking sequence [12-13]. These materials exhibit the ability to carry the extensive loading until they fail by various damage mechanisms, including delamination [14], matrix cracking [15] and fiber breakage [16-17]. Glass fiber reinforced polymer matrix composites have been using in various application area such as ballistic impact [18-21], shock response [22] and low velocity impact [23-27]. Dong and Davies [28] investigated the flexural properties of glass and carbon fiber reinforced epoxy matrix hybrid composites. They presented composites using three combinations of carbon and glass fibers, namely S-2&T700S, S-2&TR30S, and E&TR30S. They determined that compressive failure was the dominant mode of failure. To gain further insights, finite element analysis was employed to simulate flexural behavior. Both experimental results and finite element analysis indicated that the flexural modulus decreased as the percentage of glass fibers increased. Additionally, substituting carbon fibers with glass fibers on the compressive surface showed positive hybrid effects.

Evci and Gülgeç [23] studied impact response of unidirectional E-Glass, woven E-Glass, and woven Aramid composites. The research revealed that woven composites surpass unidirectional composites in their ability to withstand low-velocity impacts, and furthermore, damage propagation within woven composites was limited with a smaller area. It is concluded that the strength of the composite materials significantly increases under dynamic loading in comparison to static loading due to their sensitivity to strain rate.

Subagia and Kim [29] carried out a series of experimental studies to understand flexural properties of carbon-basalt/epoxy hybrid laminates. They revealed an approximate solution for flexural strength and modulus of the hybrid composite depending on the number of basalt fabrics. The flexural properties of carbon-basalt/epoxy hybrid composites were found to be highly influenced by stacking sequence of the carbon and basalt fabric layers.

Baky et al. [30] studied tensile, flexural and impact properties of flax/basalt/E-glass fibers reinforced epoxy composites. There was a noticeable improvement in the flexural and impact resistances of the material by

* Corresponding author. Tel.: +902268155421.
E-mail addresses: aiayten@yalova.edu.tr (A.İ. Ayten)
ORCID: 0000-0002-3948-3690
DOI: 10.35860/iarej.1334883

incorporating high-strength fibers into the outer layers of the composite. However, it was observed that this enhancement in performance came at the cost of reduced tensile properties. In other words, the composite exhibited improved resistance to bending and impact loadings but experienced a decrease in its ability to withstand tension loadings. This trade-off between flexural/impact properties and tensile properties should be carefully considered when selecting the optimal fiber arrangement for specific engineering applications.

Fiber, matrix, and interface properties of composites have an effect on in-plane shear behavior of polymer matrix composites [31]. It has been observed that shear behavior of carbon fiber reinforced epoxy matrix composites includes two regions. One of these is controlled by matrix yielding and the second is controlled by elastic deformation of reinforcement material. Yield strength of matrix and interface strength properties are the key parameter on in-plane shear behavior of composite materials while the properties of reinforcement material have no effect on it.

This study has been presenting a series of experimental studies including tension, compression, in-plane shear, and flexural tests to get elastic material properties for using them in numerical studies. Each of the experiments was conducted in both 0° (longitudinal) and 90° (transverse) directions. Additionally, damage mechanisms were interpreted for tension, compression, in-plane shear, and flexural test. The specific results obtained throughout this study will be a data set for numerical studies which includes unidirectional E-glass reinforced epoxy matrix composites.

2. Materials and Method

330 g/m^2 areal density unidirectional (UD) E-glass fiber fabric and Araldite LY1564/Aradur 3486 epoxy resin/hardener were used in this study. The hardener was used 34 g for 100 g of epoxy resin as described in datasheet. 12 layers of fabric was used to obtain 3 mm of thickness plate (Figure 1). The composite plate was manufactured by vacuum-assisted resin transfer molding (VARTM) method. First, the aluminum plate was heated, and epoxy resin mixture was transferred through resin flow medium (Figure 1b) into the UD E-glass fabrics and kept under 100 °C for 1 h. Then, it was cooled to the room temperature for 24 h. Tabbing with same material was applied to tension and compression test specimens to prevent specimens from crushing. 65% fiber weight fraction (w_f) was determined by dividing used fabric weight (W_f) to composite plate weight (W_c) after cutting process as shown in Equation (1). Specimens were cut via CNC water jet machine (Figure 1f).

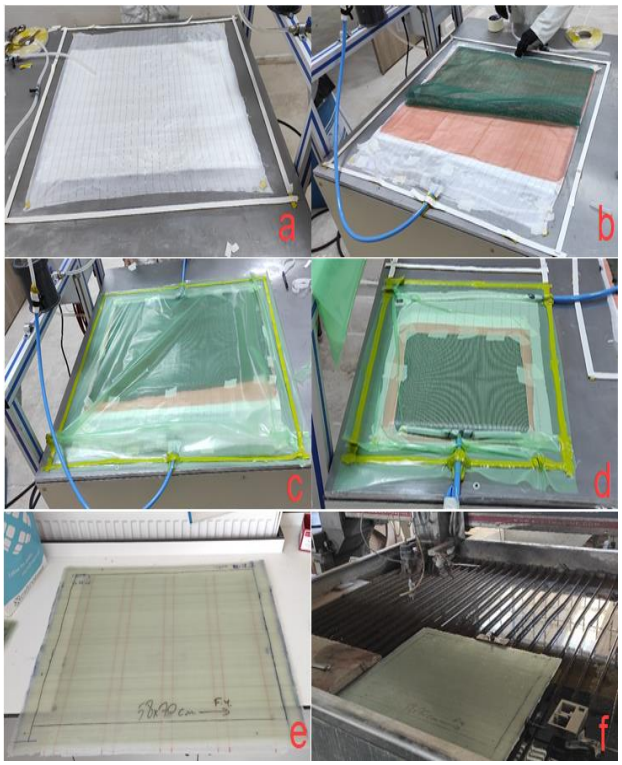

Figure 1. Manufacturing and sample preparation steps for composite plate. a) Application of sealant tapes and peel ply (white color), b) putting release film (orange color), resin flow medium (dark green color), polyethylene tube (blue color) c) covering vacuum bagging film (green color), d) after vacuum was applied, e) obtained composite plate, f) positioning of composite plate on CNC water-jet machine for cutting test samples.

The mechanical tests were conducted using a universal electromechanical test device equipped with a 50 kN load cell (Shimadzu AGSX series, manufactured by Shimadzu Scientific Instruments). Tension, in-plane compression, in-plane shear test and flexural tests were performed according to ASTM D3039, ASTM D6641, ASTM D7078, ASTM D790 standards, respectively. During the experiments, the tensile and shear samples were subjected to a test speed of 2 mm/min, while the compression and flexural samples were tested at a speed of 1.3 and 1 mm/min, as specified in the corresponding ASTM standards. To prevent buckling during the compression tests, the gage length of the samples was set at 13 mm. Special test fixtures were manufactured for the shear and compression tests. The complete set of mechanical tests applied to the composite samples can be found in Figure 2a-d.

$$w_f = \frac{W_f}{W_c} \quad (1)$$

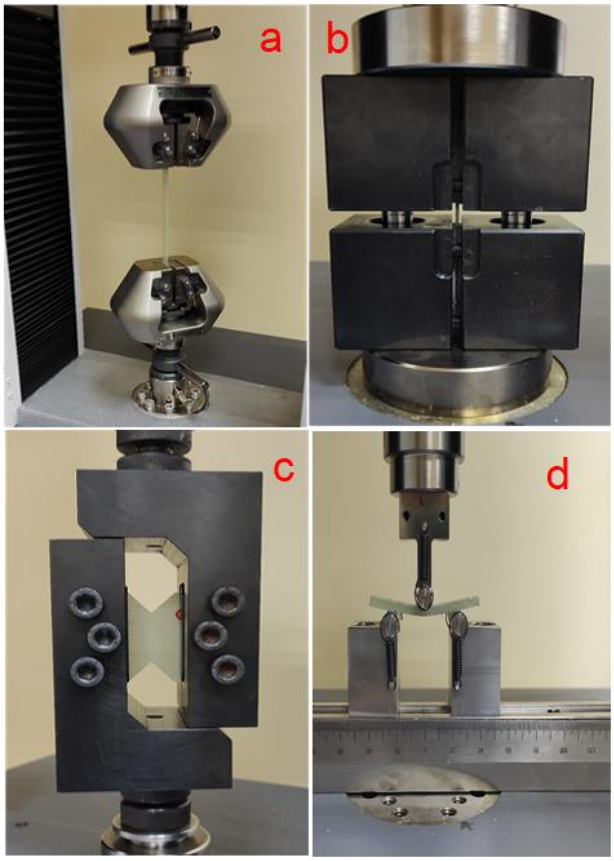

Figure 2. Mechanical test fixtures which were used throughout the study. a) Tension, b) in-plane compression, c) in-plane shear (V-notched) test, d) flexural test.

Among various shear tests such as short-beam shear, two-rail shear, three-rail shear, and +45° tensile shear available for composites, the V-notched rail shear test was selected for its ability to apply a uniform shear stress to the test samples. To ensure accurate and reliable results, the bolts of the shear test apparatus were tightened to a torque of 55 Nm. Using a torque lower than this value could potentially lead to slipping of the sample between the grips, which could compromise the test results. By applying the appropriate torque, the shear test apparatus would firmly hold the specimen in place, preventing any undesired movement during the test.

3. Results and Discussion

The mechanical properties of the UD E-glass fiber/epoxy composite, with a fiber weight ratio of 65%, were determined through various tests, including tensile, compression, in-plane shear, and flexural tests (Figure 3 and 4). In the case of the tensile test at longitudinal direction, the sample failed at 628.4 MPa of stress and 5.62% of strain while these values were 73.57 MPa and 2.83% for the tensile test at transverse direction. For compression test, the maximum compression strength and failure strain were determined as 375 MPa and %23 at longitudinal direction while they are 118 MPa and 15.5%

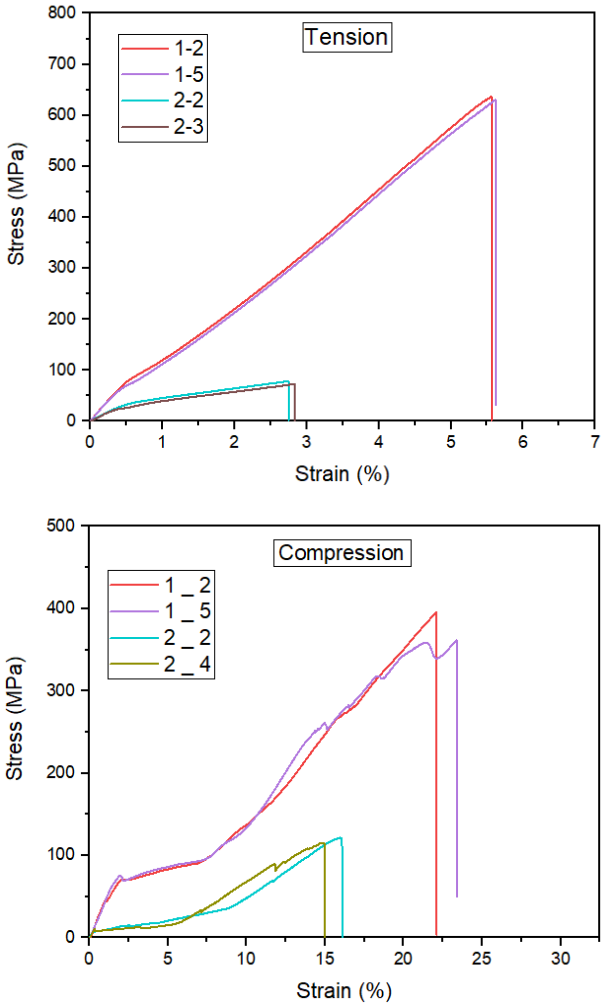

Figure 3. Tension and compression results of unidirectional E-glass fiber reinforced composite

for transverse compression test. Additionally, the maximum shear stress was observed at 56.68 MPa at the strain of 17.8% for longitudinal direction and 51.3 MPa and 18% for transverse direction. Finally, maximum load observed in flexural test was 1.93 kN at 3.33 mm displacement for longitudinal direction while they were 0.484 kN at 2.62 mm displacement value for transverse direction.

For V-notched shear test curves, the results of both fiber direction (0° and 90°) specimen behavior are similar to each other until their maximum loading point. Sudden load drop has been occurring in transverse direction specimen because the loading and fiber have the same direction. This situation will force the specimen for shear breakage as can be seen in Figure 6a (specimen 2-4). On the other hand, fibers have been performing extension because the fibers are perpendicular to the loading direction like in Figure 6a (specimens 1-3 and 1-4). The loading in the V-notched shear test for the specimens having longitudinal direction is not like a pure tensile loading, that's why the fibers did not break at the low strain values like in tensile test.

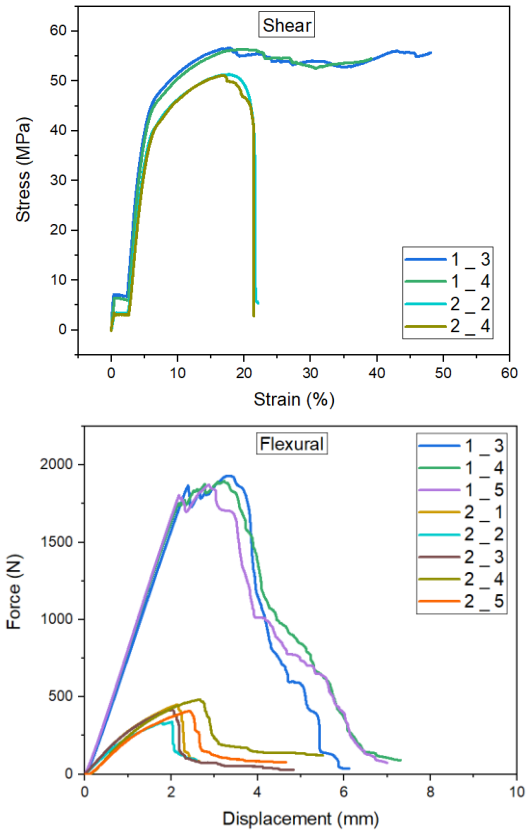

Figure 4. Shear and flexural test results of unidirectional E-glass fiber reinforced composite

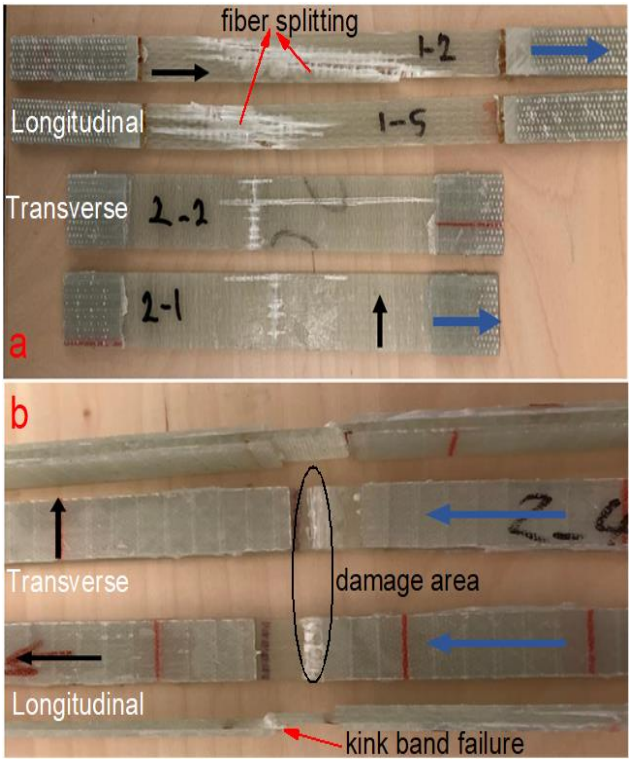

Figure 5. Damage patterns occurred at the end of a) 0° (longitudinal) and 90°(transverse) tension, b) 0° and 90° compression test. Blue arrows indicate loading direction. Black arrows indicate fiber direction.

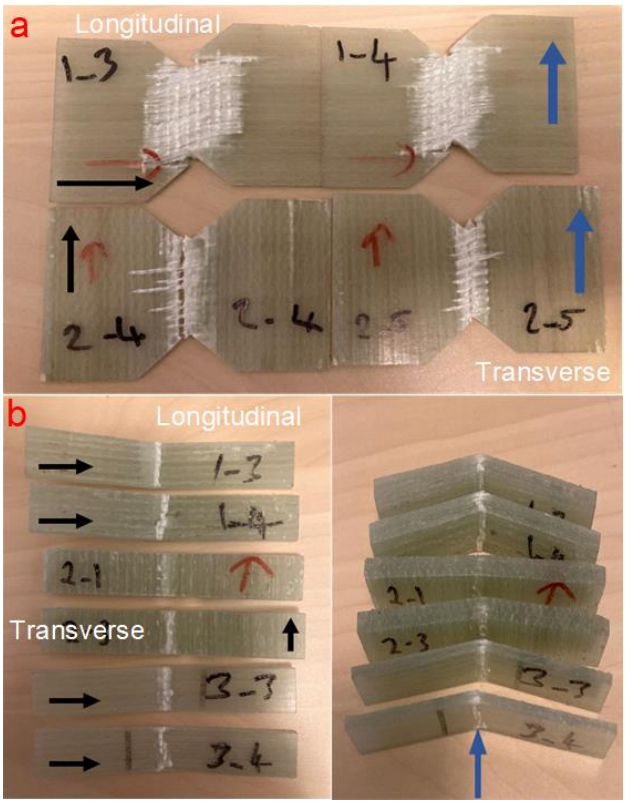

Figure 6. Damage patterns occurred at the end of a) 0° and 90° shear, b) 0° and 90° flexural test. Blue arrows indicate loading direction. Black arrows indicate fiber direction.

In Figure 4, the flexural test curves perform a linear elastic behavior until 2 mm deflection values. At this point, the matrix cracking started, and it caused small vibrations in the curves. Then the load drastically drops due to the fiber breakage [32].

Figure 5a and 5b show damage zones that occurred at the end of tension and compression tests in longitudinal and transverse directions. Fiber splitting damage mechanism is dominant in 0° (longitudinal) test specimens (1-2 and 1-5). There is no damage around tab region, so it can be said that experiments are valid [33]. For transverse direction, a discontinuity was observed in specimen 2-2. One of the fiber bundles failed throughout tabbing. On the other hand, the curve of specimen 2-2 in Figure 3 does not include any instability. Edge delamination failure can be seen in specimen 2-1. It means the stress waves propagated through the edge due to the fiber direction.

In Figure 5b, damage occurred in the gage section, and it is close to the tabbing because gage length is 13 mm. Herein, side views are important to understand whether experiments are valid or not. If there is no propagated damage through the edges of specimen, it may be assumed experiment is valid [33]. Kink band failure can be seen at the below specimen in Figure 5b because compression loading was applied in longitudinal direction. This type of failure has been commonly observed in longitudinal compression [34-35].

Table 1. Mechanical properties of E-glass fiber reinforced epoxy matrix composite material

Experiment	Modulus (GPa)	Strength (MPa)	Strain at failure (%)
0°-Tensile	16.53	636	5.62
90°-Tensile	6.81	73.57	2.83
0°-Compression	3.75	375	23
90°-Compression	0.31	118	15.5
In-plane shear	1.18	56.68	18

Figure 6a presents in-plane shear test specimens for 0° and 90° fiber direction. When this figure is evaluated with shear test curves in Figure 4, it will be more understandable. The first difference between the two specimens is the damage area. In specimens 1-3 and 1-4, fiber direction is vertical to the loading direction. This is the reason why the damage area in 1-3 and 1-4 is bigger than 2-4 and 2-5. Fibers in specimens 1-3 and 1-4 have been subjected to tension-dominated loading.

These mechanical test results provide valuable insights into the behavior and performance of the UD E-glass fiber reinforced epoxy matrix composite under different loading conditions, contributing to a better understanding of its mechanical properties and potential applications.

4. Conclusions

Tension, compression, in-plane shear, and flexural tests were performed in both longitudinal and transverse directions to characterize the material behavior under various loading conditions. The results of this study provide valuable insights into the mechanical behavior and performance of the E-glass fiber reinforced epoxy composite. The key findings from the mechanical tests are summarized below:

• In tension tests, the composite exhibited a tensile strength of 628.4 MPa and 73.57 MPa in the longitudinal and transverse directions, respectively. The corresponding strain at failure was 5.62% and 2.83%, highlighting the anisotropic nature of the material.

• In compression tests, the composite displayed a maximum compression strength of 375 MPa in the longitudinal direction and 118 MPa in the transverse direction, with failure strains of 23% and 15.5%, respectively.

• The maximum shear stress observed was 56.68 MPa for longitudinal shear and 51.3 MPa for transverse shear, both at a strain of 18%. In flexural tests, the composite exhibited a maximum load of 1.93 kN and 0.484 kN for longitudinal and transverse flexure, respectively. All mechanical properties were presented in Table 1.

Fiber splitting was identified as the dominant failure mode in tension tests, while kink band failure was prominent in compression tests. In-plane shear tests showed varying damage areas depending on the fiber orientation.

These comprehensive mechanical characterizations provided essential material model parameters for future numerical studies and simulations involving this E-glass fiber reinforced epoxy composite. The presented mechanical properties data, including modulus, strength, and strain at failure, can serve as a fundamental for modeling and predicting the behavior of this material in various engineering applications.

References

1. Atas, C. and O. Sayman, An overall view on impact response of woven fabric composite plates. Composite Structures, 2008. **82**(3): p. 336-345.
2. Aktaş, M., et al., An experimental investigation of the impact response of composite laminates. Composite Structures, 2009. **87**(4): p. 307-313.
3. Yang, L., Y. Yan, and N. Kuang, Experimental and numerical investigation of aramid fibre reinforced laminates subjected to low velocity impact. Polymer Testing, 2013. **32**(7): p. 1163-1173.
4. Ünal, H. and K. Ermiş, Determination of mechanical performance of glass fiber reinforced and elastomer filled polyamide 6 composites. International Advanced Researches and Engineering Journal, 2021. **5**(3): p. 405-411.
5. Chen, Y., et al., Advances in mechanics of hierarchical composite materials. Composites Science and Technology, 2021. **214**: p. 108970.
6. Tarfaoui, M., S. Choukri, and A. Neme, Effect of fibre orientation on mechanical properties of the laminated polymer composites subjected to out-of-plane high strain rate compressive loadings. Composites Science and Technology, 2008. **68**(2): p. 477-485.
7. Nagaraja, K.C., et al., Mechanical properties of polymer matrix composites: Effect of hybridization. Materials Today: Proceedings, 2021. **34**: p. 536-538.
8. Yang, H., et al., Low-velocity impact performance of composite-aluminum tubes prepared by mesoscopic hybridization. Composite Structures, 2021. **274**: p. 114348.
9. Wang, M., et al., Effect of carbon/Kevlar asymmetric hybridization ratio on the low-velocity impact response of plain woven laminates. Composite Structures, 2021. **276**: p. 114574.
10. Guo, R., et al., Effect of fiber hybridization types on the mechanical properties of carbon/glass fiber reinforced polymer composite rod. Mechanics of Advanced Materials and Structures, 2022. **29**(27): p.6288-6300.
11. Kaware, K. and M., Kotambkar, Experimental investigation of hybridization effect of Kevlar and Glass fibers on CFRP composite under low velocity impact. International Journal of Crashworthiness, 2023. https://doi.org/10.1080/13588265.2023.2230634.
12. Karaduman, Y., L. Onal, and A. Rawal, Effect of stacking sequence on mechanical properties of hybrid flax/jute fibers reinforced thermoplastic composites. Polymer Composites, 2014. **36**(12): p. 2167-2173.
13. Andrew, J. J., et al., Influence of patch lay-up configuration and hybridization on low velocity impact and post-impact tensile response of repaired glass fiber reinforced plastic

composites. Journal of Composite Materials, 2019. **53**: p. 3-17.

14. Schwab, M., et al., Modeling, simulation, and experiments of high velocity impact on laminated composites. Composite Structures, 2018. **205**: p. 42-48.
15. Wagih, A., et al., A quasi-static indentation test to elucidate the sequence of damage events in low velocity impacts on composite laminates. Composites Part A: Applied Science and Manufacturing, 2016. **82**: p. 180-189.
16. Ayten, A.İ., B. Ekici, and M.A. Taşdelen, A numerical and experimental investigation on quasi-static punch shear test behavior of aramid/epoxy composites. Polymers and Polymer Composites, 2019. **28**(6): p. 398-409.
17. Rahman, M. B., and L., Zhu, Low-Velocity Impact Response on Glass Fiber Reinforced 3D Integrated Woven Spacer Sandwich Composites. Materials, 2022. **15**: p. 2311.
18. Gellert, E.P., S.J. Cimpoeru, and R.L. Woodward, A study of the effect of target thickness on the ballistic perforation of glass-fibre-reinforced plastic composites. International Journal of Impact Engineering 2000. **24**: p. 445-456.
19. Farias-Aguilar, J. C., et al., Evaluation of the ballistic protection level of (glass-fiber reinforced polyamide 6)-aramid fabric sandwich composite panels. Journal of Materials Research and Technology, 2021. **12**: p. 1606-1614.
20. Ojoc, G. G., et al., Ballistic Response of a Glass Fiber Composite for Two Levels of Threat. Polymers, 2023. **15**: p. 1039.
21. Mahesh, V., et al., Damage mechanics and energy absorption capabilities of natural fiber reinforced elastomeric based bio composite for sacrificial structural applications. Defence Technology, 2021. **17**: p. 161-176.
22. Dandekar, D.P., et al., Shock response of a glass-fiber-reinforced polymer composite. Composite Structures, 2003. **61**(1-2): p. 51-59.
23. Evci, C. and M. Gülgeç, An experimental investigation on the impact response of composite materials. International Journal of Impact Engineering, 2012. **43**: p. 40-51.
24. Boukar, A., et al., Finite element modelling of low velocity impact test applied to biaxial glass fiber reinforced laminate composites. International Journal of Impact Engineering, 2022. **165**: p. 104218.
25. Wang, W., et al., Low-velocity impact behaviors of glass fiber-reinforced polymer laminates embedded with shape memory alloy. Composite Structures, 2021. **272**: p. 114194.
26. Gemi, D. S., et al., Experimental investigation of the effect of diameter upon low velocity impact response of glass fiber reinforced composite pipes. Composite Structures, 2021. **275**: p. 114428.
27. Farhood, N. H., et al., Experimental investigation on the effects of glass fiber hybridization on the low-velocity impact response of filament-wound carbon-based composite pipes. Polymer and Polymer Composites, 2021. **29**(7): p. 829-841.
28. Dong, C. and I.J. Davies, Flexural properties of glass and carbon fiber reinforced epoxy hybrid composites. Proceedings of the Institution of Mechanical Engineers, Part L: Journal of Materials: Design and Applications, 2012. **227**(4): p. 308-317.
29. Ary Subagia, I.D.G. and Y. Kim, A study on flexural properties of carbon-basalt/epoxy hybrid composites. Journal of Mechanical Science and Technology, 2013. **27**(4): p. 987-992.
30. Abd El-Baky, M.A., et al., Flax/basalt/E-glass Fibers Reinforced Epoxy Composites with Enhanced Mechanical Properties. Journal of Natural Fibers, 2020. **19**(3): p. 954-968.
31. Totry, E., et al., Effect of fiber, matrix, and interface properties on the in-plane shear deformation of carbon-fiber reinforced composites. Composites Science and Technology, 2010. **70**: p. 970-980
32. Ma, Y., et al., Effect of fiber breakage position on the mechanical performance of unidirectional carbon fiber/epoxy composites. Reviews on Advanced Materials Science, 2021. **60**: p. 352-364.
33. American Society for Testing Materials, Standard test method for compressive properties of polymer matrix composite materials using a combined loading compression test fixture. ASTM D6641/D6641M-09 standard.
34. Wang, Y., et al., Evolution of fibre deflection leading to kink-band formation in unidirectional glass fibre/epoxy composite under axial compression. Composite Science and Technology, 2021. **213**: p. 108929.
35. Wilhelmsson, D., et al., Influence of in-plane shear on kink-plane orientation in a unidirectional fibre composite. Composites Part A, 2019. **119**: p. 283-290.

Available online at www.dergipark.org.tr/en

INTERNATIONAL ADVANCED RESEARCHES and ENGINEERING JOURNAL

Journal homepage: www.dergipark.org.tr/en/pub/iarej

e-ISSN: 2618-575X

International Open Access

Volume 07
Issue 03

December, 2023

Research Article

Utilization and effects of various particle sizes of waste glass powder as partial replacement of cement in concrete

Wafiullah Shirzad [a, *], ***Mohammad Mukhlis Behsoodi*** [a,b] ***and Muhammad Yaqub Tasal*** [a]

[a] *Civil Engineering Department, Alfalah University, Jalalabad, Nangarhar, Afghanistan*
[b] *Academic Division, Spinghar Institute of Higher Education, Jalalabad, Nangarhar, Afghanistan*

ARTICLE INFO

Article history:
Received 26 March 2023
Accepted 13 December 2023
Published 15 December 2023

Keywords:
Cement
Compressive Strength
Utilization
WGP
Workability

ABSTRACT

This paper outlines the study undertaken regarding the usage and impacts of different particle sizes of Waste Glass Powder (WGP) when used as a partial replacement for cement in concrete. Through utilization WGP as a cement substitute, the mechanical and physical attributes, compressive strength and workability of concrete were assessed. The glass has been sieved from #200 sieve which has size of 74 µm and also sieved from #325 sieve which has size of 44 µm for a partial substitute of cement. To compare the WGP-replaced concrete's properties to reference specimens with no replacement at all, WGP was used to substitute 20% of the Portland cement in the concrete. The control samples were created following the IS-10262-2009 standard to reflect a goal of 30 Mpa, and cylindrical samples were fabricated, subjected to curing, and assessed for workability and compressive strength at intervals of 7, 14, 21, and 28 days after its casting. In conclusion, when the WGP particles are smaller, concrete becomes more workable and has a higher compressive strength then concrete with bigger particle sizes of WGP and control samples with no replacement. The findings of this study led to the conclusion that WGP's cementitious properties are acquired by its finer particles.

1. Introduction

Concrete, a fundamental material in construction, stands as the most extensively utilized man-made substance globally. In the year 2007, the consumption of concrete in the United States alone reached a staggering 800 million tons, contributing to a worldwide estimate of 11 billion tons—an equivalent of roughly 1.7 tons per capita for every individual on the planet [1]. Moreover, being the predominant construction material, concrete is primarily manufactured through processes that heavily rely on nonrenewable natural resources and energy-intensive methods, leading to significant greenhouse gas emissions. There is a possibility to enhance the industry's sustainability through a comprehensive exploration of alternative materials [2]. However, it is a composition of cement, aggregate, and sand, with the possibility of incorporating additional elements such as additives, retardants, hardeners, and more [3].

In 1824, Joseph Aspdin achieved a groundbreaking milestone by introducing Portland Cement, an artificial hydraulic lime. This development, reminiscent of James Parker's Roman Cement from 1796, marked a significant step in the evolution of cement production. William Aspdin further refined this process in 1842 in England, shaping Portland Cement into its modern manifestation. Key ingredients in cement production include alumina (Al2O3) limestone (CaCO3), magnesium oxide (MgO), Silica (SiO2), and ferrous oxide (Fe2O3) [4]. Moreover, while serving as the primary component in concrete, providing strength, and acting as the binding agent for other ingredients, cement is produced on a colossal scale. The United States alone produces an estimated 85.9

* Corresponding author. Tel.: *+93 786 101 652 - +93 747 402 611.*
E-mail addresses: shirzad.wafiullah@gmail.com *(Wafiullah Shirzad)*, mukhlis.behsoodi@gmail.com *(Mohammad Mukhlis Behsoodi)*, yaqubtasal123@gmail.com *(Muhammad Yaqub Tasal)*
ORCID: 0009- 0000-191-0147 *(Wafiullah Shirzad)*, 0000-0002-4087-3979 *(Mohammad Mukhlis Behsoodi)*, 0009-0002-9418-4615 *(Muhammad Yaqub Tasal)*
DOI: 10.35860/iarej.1270868

million metric tons of cement, contributing to a global production exceeding a staggering 4,200 million metric tons [5]. Nonetheless, the production of the traditional binding material used in concrete, specifically cement, imposes a detrimental effect on the environment [6]. Furthermore, its manufacturing involves substantial energy consumption and produces substantial amounts of CO2 into the air. With annual production rates rising to fulfill the increasing demand, the heightened usage of energy and CO2 emissions underscore the urgency of exploring alternative materials that can partially replace the use of cement [5]. Moreover, the production of cement, requiring substantial energy, contributes significantly to carbon dioxide (CO2) emissions and adds to greenhouse gases. Over the past 200 years, atmospheric carbon dioxide levels have increased by approximately 30 percent [7].

The utilization of reused materials emerges as a pivotal and highly effective approach for both economic conservation and environmental sustainability. Specifically, recycling glass significantly contributes to the global well-being. In the face of restricted and dwindling capacities in landfill areas, recycled glass stands out as a positive force. Categorized as non-biodegradable, waste glass finds itself among discarded materials, including vehicles, building windows (both colored glass and clear), cathode ray tube glass and lamp glass [8]. Moreover, the recyclability of a material is contingent on its ability to maintain both its crystalline structure and chemical composition [6]. Although it is a single material, when finely ground into a powder, it demonstrates pozzolanic properties suitable to partially substitute cement in concrete [9].

Its remarkable attributes like low permeability, chemical inertness, optical transparency, and high intrinsic strength, glass emerges as an exceptionally versatile material on a global scale. Nevertheless, on an annual basis, millions of tons of waste glass are produced globally. Once glass transforms into waste, it is commonly relegated to landfills, presenting sustainability challenges due to its non-decomposable nature in the environment. Recognizing that glass predominantly consists of silica, integrating milled (crushed) waste glass into concrete as a partial alternative to cement becomes a pivotal measure in crafting sustainable infrastructure systems—ones characterized by environmental friendliness, energy efficiency, and economic viability. The procedure of grinding WG into tiny-sized particles is expected to trigger reactive reactions with cement compounds, culminating in the creation of secondary Calcium Silicate Hydrate (C-S-H) [10]. However, the approximate global volume of glass deposited in landfills each year is estimated to be around 200 million tons, indicating an exceptionally low rate of recycling. [11]. Moreover, the idea of integrating waste glass into concrete production, either as a substance with cement-like properties or a partial replacement for cement, stems from the inherent pozzolanic attributes of glass. However, the pozzolanic characteristics of glass undergo significant variations contingent upon the sizes of the glass particles [12]. Furthermore, the introduction of GP into concrete impacts both the hardened and fresh characteristics of the concrete [13].

The workability of freshly mixed concrete refers to its ease of proper mixing, placement, consolidation, and finishing without significant loss of uniformity. The traditional slump test is employed to evaluate the workability of fresh concrete. The incorporation of Waste Glass Powder (WGP) is noted to improve the workability of concrete [4]. Moreover, waste glass particles exhibited reduced water absorption in comparison to sand, consequently improving the workability of the concrete mix [14]. Moreover, it was verified that the slump measurements of the concrete, across various levels of glass substitution, consistently stayed within the targeted slump range between 100–125 mm without any alteration in the water level [10]. Indeed, the reduction in slump with an increase in WGP content within concrete implies a decreased workability when compared to plain concrete [15].

Replacing cement with glass powder at rates of 20%, 30%, and 40% resulted in a corresponding increase in compressive strength of 19.6%, 25.3%, and 33.7%, respectively [16]. Furthermore, the utilization of 15% GP as a cement additive improved the average concrete compressive strength by 16.0%, outperforming its role as a cement substitute [17]. Upon reaching a 45% WG proportion, a substantial 31% decline was noted. Remarkably, as this proportion further increased to 60%, a noteworthy 49% decrease in compressive strength was noticed [18]. Furthermore, the reduction in strength could be ascribed to a diminished adhesion between the interface of the WG and the cement hydrates [19]. Additionally, the concrete's compressive strengths at 7 days, 14 days, and 28 days exhibit an initial increase with the ascending percentage of cement replacement with WP, attaining a pinnacle at approximately 20%, followed by a subsequent decline [20]. Hence, employing glass in concrete within the replacement range of 10% to 25% in cement results in a 12% decrease in strength [21]. Nevertheless, at later ages, there appears to be an enhancement in the concrete's compressive strengths with higher degrees of cement substitution with GP. The concrete with 20% substitution of cement with GP exhibited the concrete combination with the highest compressive strength [22].

The categorization of concrete's tensile strength typically falls into one of three categories: flexural strength, splitting tensile strength, or direct tensile

strength. These classifications are established using different testing methodologies [23]. In addition, in ordinary concrete, a 5% WGP replacement demonstrated an estimated rise of 8% in compressive strength and 13% in tensile strength, respectively [24]. Moreover, there is a reduction in splitting tensile strength with the growth in GP content [14]. Moreover, beyond the 28-day period, there was an observed improvement in tensile strength in the mixes incorporating glass powder. The mix with 20% glass powder displayed the mix with 30% achieved the highest tensile strength, glass powder demonstrated strength comparable to the control mix. The heightened increase in tensile strength might be attributed to the decrease in pore size due to the pozzolanic reaction intensifies, resulting in the creation of denser Calcium Silicate Hydrate (CSH) [25]. Moreover, with the incorporation of 15%, 18%, and 21% WP, there was a corresponding decrease in tensile strength by 34%, 44%, and 45%, respectively. Furthermore, a notable 51% reduction in the tensile strength was detected when the GP composition reached 24% in the concrete mix [26]. Though, lacking any glass powder in the concrete mixture, the concrete samples containing crushed glass aggregate exhibited substantially lower splitting tensile and compressive strength values contrasted to the concrete incorporating natural mineral aggregate [27].

In this study, we investigated the impact of substituting 20% of the weight of #325 sieves that passed WGP and 20% of the weight of #325 sieves that retained WGP for cement. Our examination focused on the compressive strength and workability of concrete specimens, alongside the passing and retaining of the #325 sieve under the #200 sieve. Comparing the concrete mix with WGP of #325 sieve passing to normal M-30 concrete mix revealed minimal differences, as did the comparison of the concrete mix with WGP of #200 sieve passing and retainment of #325 sieve in its composition. This study significantly contributes to the existing literature by providing a comprehensive analysis of how concrete behaves when various particle sizes of WGP are utilized as a partial substitute for cement.tt

2. Research Significances

Non-recyclable WG poses a significant challenge for landfills as it does not biodegrade. Due to Its non-degradable nature and the limited availability of landfill space in urban or urban surrounding areas, its disposal is considered as a considerable difficulty. To convince people that glass waste may be used in buildings, it is essential to evaluate if glass waste is suitable as an alternative cement in concrete. To establish if the results of the test satisfy the standards or not, the test must be examined. This is true since the test results will show if glass trash is capable of achieving the minimum standards for both physical and mechanical qualities. Due to glass having similar chemical composition and physical characteristics to cement, the cement industries and concrete offer a promising avenue for utilizing glass waste. It will simultaneously protect the environment, preserve natural resources, and revive the economy. In some cases, recycled glass can be used in place of cement to make concrete. It is strongly advised and a highly regarded as a substitute for cement in concrete construction due to its pozzolanic properties.

3. Methods and Materials

3.1 Used Materials

Below is a description of the materials used in this investigation:

3.1.1 Cement

A fine substance called cement serves as a binder in concrete. In this study, Stallion ordinary Portland cement, PLC-CEM II/B-L with a strength class of 42.5N and compliant with PS 5313:2014, was used (Tables 1-3).

Table 1. The results of physical tests conducted on cement

Test Name	Unit	Obtained Result
Le. Chatlier	mm	1.00
Fineness	m^2/k_g	406.00
Setting Time (Initial)	minutes	165.00
Consistency	%	26.00
Setting Time (Final)	minutes	215.00

Source: The above tests were conducted by Bestway Cement Limited Farooqia according to PS 5313:2014.

Table 2. Cement Compressive Strength Tests Result

Duration	Unit	Achieved Outcome
02 Days	Mpa	23.63
28 Days	Mpa	43.34

Source: The above tests were conducted by Bestway Cement Limited Farooqia according to PS 5313:2014.

Table 3. Cement Chemical Tests Result

Test Name	Unit	Achieved Outcome
SiO_2	%	18.83
Al_2O_3	%	4.18
CaO	%	61.48
MgO	%	2.84
Fe_2O_3	%	3.43
Na_2O	%	0.07
Cl	%	0.001
K_2O	%	0.82
SO_3	%	2.92
LOI	%	8.38
IR	%	0.89
Alkalis	-	0.61
C_3A	-	5.27
ALM	-	1.22

Source: The above tests were conducted by Bestway Cement Limited Farooqia according to PS 5313:2014.

3.1.2 Coarse Aggregate

As filler elements for concrete, course aggregate doesn't participate in the chemical reaction of concrete but has a significant part in the composition of concrete. It contributes between 60 and 75 percent to the total amount of concrete produced. Although typically ranging from 9.5 to 37.5 mm, coarse aggregate particles are bigger than 4.75 mm. The material used is a well-graded crushed coarse aggregate that is readily available locally, ranging in size from 4.75 mm to 19 mm. After that, laboratory tests were performed on the coarse aggregate (Table.4).

3.1.3 Sand (Fine Aggregate)

Throughout this project, river sand that passes through a filter with a 4.75 mm opening and includes 75 μm is employed. Using ASTM guidelines, further tests were carried out (Table 5).

3.1.4 Water

During concrete casting and curing, fresh and potable water is employed. It was obtained from a source behind Laboratory Building, Civil Engineering Department of Faculty of Engineering at Alfalah University in, Jalalabad, Nangarhar Province, Afghanistan.

Table 4. Lab Test Results Conducted on Coarse Aggregate

Tests	Unit	Results	Standards
Impact Value	%	7.665	BS812: Part 110: 1990
Elongation Index	%	23.221	BS812: part 105
Crushing Value	%	19.524	BS812: part 110: 1990
Los Angeles Abrasion Value	%	33.96	ASTM C131 – 03
Rodded Bulk Density	gr/cm^3	1.648	AASHTO T – 19 OR ASTM C29
Loose Bulk Density	gr/cm^3	1.487	ASTM C29 Or AASHTO T – 19
(SSD) Specific Gravity	–	2.723	ASTM C127
Water Absorption	%	0.648	ASTM C127
(OD) Specific Gravity	–	2.706	ASTM C127
Flakiness Index	%	9.459	BS812: part 105

Source: The aforementioned tests were conducted by the author.

Table 5. Results of Laboratory Tests on Sand

Tests	Unit	Results	Standards
SSD Specific Gravity	-	2.685	ASTM C128
Sand Equivalent	%	6.326	ASTM D-2419
OD Specific Gravity	-	2.613	ASTM C128
Rodded Bulk Density	gr/cm^3	1.598	ASTM C-29
Fineness Modulus	-	2.748	ASTM C136
Grading Zone	-	1	-
Loose Bulk Density	gr/cm^3	1.503	ASTM C-29
Water Absorption	%	2.774	ASTM C128

Source: The aforementioned tests were conducted by the author.

Table 6. Glass Chemical Composition

Oxides	Percentage	Oxides	Percentage
SiO_2	68.10	Al_2O_3	0.90
CaO	14.50	K_2O	0.80
Na_2O	12.20	Fe_2O_3	0.60
MgO	1.80	SO_3	0.40
LOI	-	Moisture	-

Source: The above chemical composition of glass is taken form a research paper [10].

3.1.5 GP (Glass Powder)

Sustainability entails a system's capacity for long-term continuation, incorporating the reutilization, recycling, and reduction of materials as integral components [28]. Although, the waste glass was sourced from the disposal sites of glass retail stores, indicating an effort towards incorporating sustainable practices. The WG was washed with water to eliminate dust and other impurities before being ground into powder to produce WGP. After that, it was left to dry naturally for 24 hours. Following that, it was crushed using a Los Angeles Abrasion machine until the particles reached a very small size to be retained and passed via a No. 325 mesh sieve, achieving the desired cement grading, and it was incorporated into the concrete to improve its qualities (Figures 1-2). WG has a 2.56 specific gravity [5]. WGP was utilized as a partial substitute for cement in concrete at a rate of 20% in a variety of particle sizes. Two different WGP particles, passing at 74 μm (#200 sieve) and retain at 44 μm (#325 sieve), as well as the passing at 44 μm (#325 sieve), were employed in this study. Using ASTM standards, the consistency test was completed on WGP. The table below outlines the chemical composition of the glass (Tables 6-7).

Table 7. Lab Tests Result of WGP Consistency

Tests	Unit	Result of No.325 Sieve Passing	Result of No.325 Sieve Retain	Standards
Consistency	%	32.70	30	ASTM C - 187

Source: The test above was conducted by the author in the lab to demonstrate the consistency of WGP.

Figure 1. Broken waste glass

Figure 2. Passing and retaining waste glass through a No. 325 sieve

3.2 Methods

To produce the requisite concrete for the control mix, a mix ratio of 1 part cement to 0.75 parts fine aggregate to 1.5 parts coarse aggregate per IS-10262-2009 was employed [29]. Table 8 presents the mix proportion for control sample.

Table 8. Mix Proportion for Control Sample

Cement	Sand	Coarse aggregate	W/C ratio
1	0.75	1.50	0.45

Source: The table above displays the proportions of concrete samples utilized in the study, formulated by the author.

Natural fine aggregate and well-graded coarse aggregate were used to make the design concrete mix of M30. A sufficient number figurefof concrete cylinders were made using a mixed design with a W/C ratio of 0.45. Two further experiments were utilized without a control, using different WGP particle sizes that had 20% of their weight replaced with cement. The objective of the slump tests was to assess the workability of a concrete mixture that had different WGP particle sizes. Concrete cylinders were given a 7, 14, 21, and 28-day cure. Nine cylinders were cast for each trial to estimate the compressive strength measured at intervals of 7, 14, 21, and 28 days. Concrete cylinders were made using cylinder molds which has dimensions of 150mm diameter and 300mm height. Table 9 presents the mix proportions of prepared specimens.

4. Results and Discussions

4.1 Cement

The outcomes of the slump test, conducted according to ASTM C143 to determine and specify the workability of concrete are presented in Table 10.

The findings of the slump tests show that adding WGP to concrete changed its slump (Figure 3). In comparison to concrete which had WGP in its composition was more workable than the concrete which hadn't WGP in its composition. Furthermore, the water absorption of WGP-containing concrete was almost equal to zero and it made concrete to absorb less water than the concrete which hadn't WGP.

4.2 Compressive Strength

The results for 7, 14. 21 and 28 days of compressive strength of concrete, conducted as per ASTM C39. Table 11 presents the average compressive strength value.

Table 9: Mix Ratios for Prepared Samples

Mix Type	Number of Samples	Cement (Kg)	Sieved WGP (Kg)				Fine Aggregate (Kg)	Coarse Aggregate (Kg)	Water (Liter)
			Sieve #200		Sieve #325				
			P*	R**	P*	R**			
Control	12	43.2	Yes	-	NA	NA	36	85.92	19.44
Trail 1	12	34.56	Yes	-	8.64	0	36	85.92	19.44
Trail 2	12	34.56	Yes	-	0	8.64	36	85.92	19.44
*P=Passing, **R=Retained									

Source: The above table shows the mix proportion of prepared samples which was used in this research and it made by author.

Table 10. Slump Value

Mix Type	Cement Replacement Level With WGP (%)	Slump Measurement (mm)
Control	0	60
Trail 1	20	70
Trail 2	20	65

Table 11. Compressive Strength Value

Compressive Strength (Mpa)				
Cylinders				
Mix Type	7 days	14 days	21 days	28 days
Control	27.13	32.09	36.61	38.15
Trial 1	23.30	27.20	33.87	37.12
Trial 2	23.92	27.37	31.30	34.13

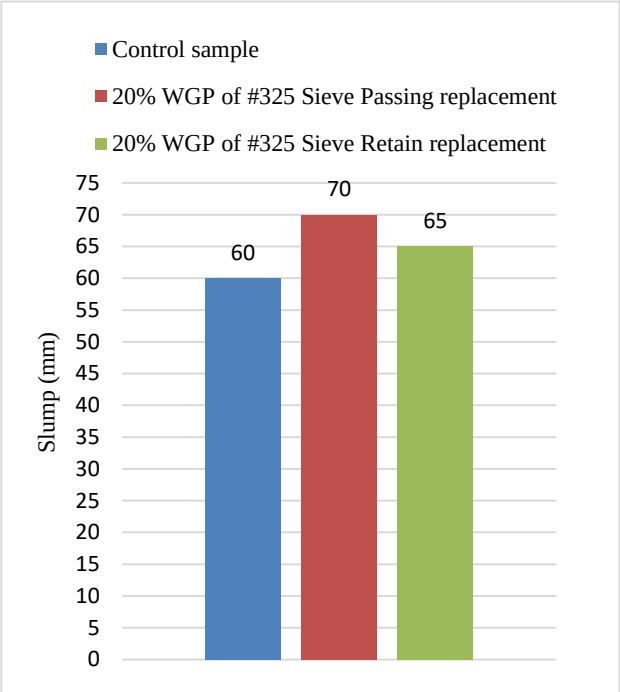

Figure 3: Comparison of slump values

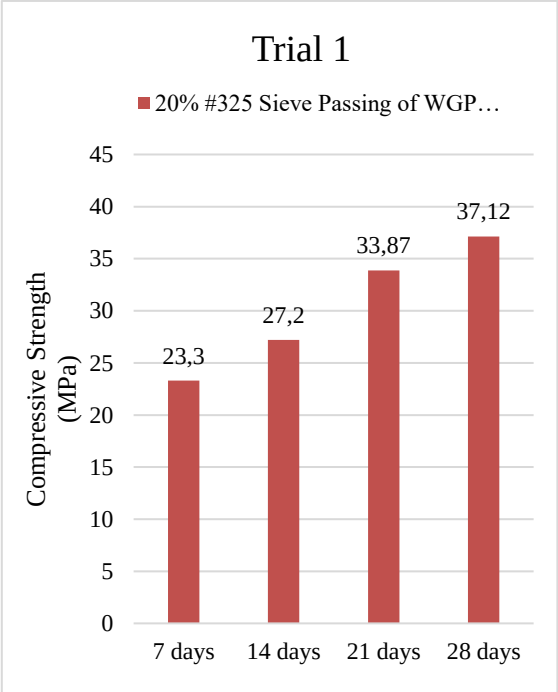

Figure 5: Trial 1 Compressive Strength

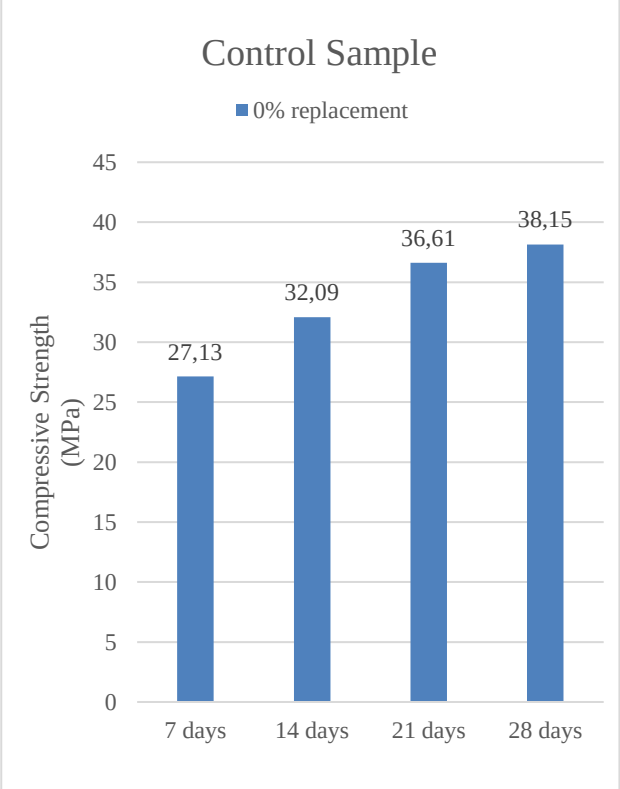

Figure 4: Control Samples Compressive Strength

Figure 4 illustrates the compressive strength of the M-30 control mix at 7, 14, 21, and 28 days. According to the test findings, the control mix was crushed into cylinders to determine the average compressive strength value after 28 days, which came to 38.15 Mpa. The average compressive strength value was attained at 28 days as 37.12 Mpa, which was approximately the target strength, according to Figure 5 which also displays the compressive strength test results of the concrete mix containing 20% of material passing through a #325 sieve passed WGP. Also, Figure 6 shows the compressive strength test results of the concrete mix containing 20% of #325 sieve retained WGP, and the average compressive strength value after 28 days was obtained 34.13 Mpa. Comparing Trials 1 and 2, it's evident from the data that the compressive strength values at 7 and 14 days were identical, and there was less of a difference between them at 21 and 28 days (Figure 7). Nevertheless, the 28-day compressive strength of the control mix and Trial 1 are nearly the same, demonstrating that the WGP-passed concrete mix offers the same strength as the concrete mix without WGP in it.

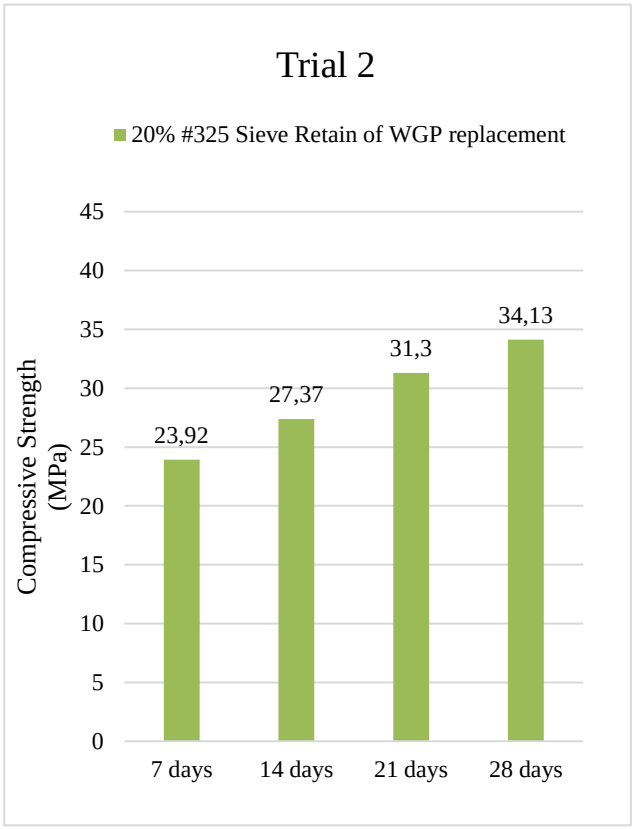

Figure 6: Trial 2 Compressive Strength

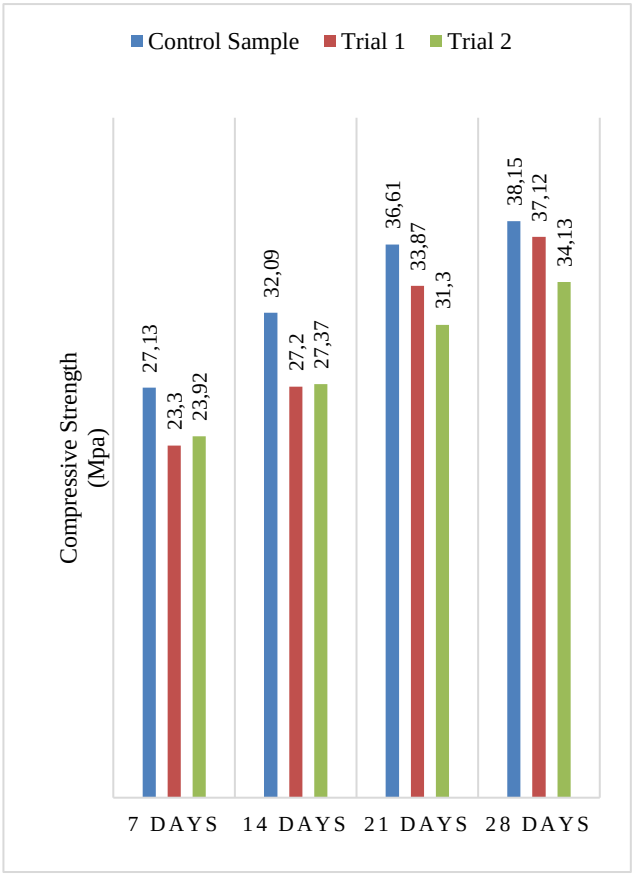

Figure 7: Comparison of Compressive Strength among Control, Trial 1, and Trial 2 Samples

4.3 Future Scope

Because of its possible benefits, such as decreasing the carbon footprint of concrete manufacturing and improving concrete durability, incorporating waste glass powder (WGP) as a partial substitute for cement in concrete has garnered a considerable interest and attention in recent times. The future scope of research on the utilization and effects of various particle sizes of WGP as a partial substitute for cement and/or sand in concrete can be categorized into the following areas:

- Optimization of WGP particle size: The impact of various particle sizes of WGP on the durability and mechanical characteristics of concrete has been studied in several research works. However, the optimal WGP particle size for achieving the desired properties of concrete is still a subject of ongoing research. Further investigations can be conducted to determine the optimal particle size of WGP for different types of concrete applications.
- Long-term performance evaluation: There is need for more investigations and research to assesses the extended performance of concrete containing WGP as a substitute for a portion of the cement. The service life and durability of concrete structures are influenced by several factors, including the utilization of additional cementitious materials. Hence, durability characteristics evaluations of concrete incorporating Waste Glass Powder (WGP) under different environmental and loading conditions should be carried out.
- Rheological characteristics of fresh concrete: The rheological characteristics of fresh concrete are crucial to ensure proper placement and consolidation of concrete during construction. Employing WGP as a partial substitute for cement can affect the rheological behavior of fresh concrete, which may result in workability issues. Therefore, the rheological properties of fresh concrete incorporating various particle sizes of WGP needs to be studied to ensure the proper placement and consolidation of concrete.
- Environmental impact: The utilization of WGP as a partial substitution of cement in concrete can decrease the carbon emissions associated with concrete production. However, the environmental impact of WGP production and its incorporation into concrete needs to be assessed. The environmental impacts of WGP-based concrete may be assessed using life cycle assessment (LCA) and compared to conventional concrete.

In conclusion, the future scope of research on the utilization and effects of different particle sizes of WGP as partial cement substitution in concrete is vast and encompasses several areas. Further investigations in

these areas may result in the formation of durable and environmentally friendly concrete with reduced carbon footprint.

5. Conclusion

Upon analyzing the test results, the below findings can be made:

- The slump tests indicated that incorporating Waste Glass Powder (WGP) into concrete altered its slump. Concrete containing WGP exhibited greater workability compared to concrete without WGP.
- The water absorption of WGP-containing concrete approached zero, resulting in significantly reduced water absorption compared to concrete without WGP.
- 28th days Compressive strength tests demonstrated that the concrete mixture containing Waste Glass Powder (WGP) passing through a #325 sieve exhibited comparable strength to the control mix without WGP. Similarly, the concrete mix with WGP retained on a #325 sieve showed slightly lower strength but still maintained acceptable levels.
- As the WGP particle size decreased, concrete became more workable, and compressive strength increased. The addition of finer particles of WG influenced the slump and workability of the concrete.
- Notably, the deficiency of compressive strength at 21 and 28 days for trials 1 and 2, when compared to the control sample, indicates that finer particles of WGP acquire cementitious capabilities.

In summary, this research demonstrates that the cementitious properties of Waste Glass Powder (WGP) are closely tied to its finer particles. Finer particles of WGP improve both the slump and compressive strength of concrete, providing a sustainable means of reusing and recycling glass waste.

Declaration

The author(s) stated that there are no conflicts of interest regarding the research, authorship, and publication of this article. Additionally, they affirmed that the article is original and was created in adherence to international publication and research ethics. No ethical committee permission or special authorization was required.

Author Contributions

All authors collaborated and contributed equally to the completion of this research.

Acknowledgment

The authors are thankful to Mr. Mohammad Jafar Malikzai, Lab Technician of Construction Materials Testing Lab of Faculty of Engineering at Alfalah University in Jalalabad, Afghanistan. The authors express their gratitude for the support offered by the Department of Civil Engineering and the close cooperation with the R&D (Research and Development) Department of Alfalah University, Jalalabad, Nangarhar, Afghanistan.

Nomenclature

WGP	: Waste Glass Powder
R&D	: Research and Development
LCA	: Life Cycle Assessment
W/C	: Water-Cement Ratio
WG	: Waste Glass
GP	: Glass Powder
NA	: Not Available
R	: Retain
P	: Passing

References

1. Aliabdo A. A., A. E. M. Abd Elmoaty, and A. Y. Aboshama, *Utilization of waste glass powder in the production of cement and concrete*. Construction and Building Materials, 2016. **124**: p. 866–877.
2. Federico, L. M. and S. E. Chidiac, *Waste glass as a supplementary cementitious material in concrete – Critical review of treatment methods*. Cement & Concrete Composites, 2009. **31**(8): p. 606–610.
3. Jangid, K. V. and A. K. Sharma, *Partial replacement of cement, sand & aggregate with waste material generated from constructional & deterioration work*. International Research Journal of Modernization in Engineering Technology and Science, 2021. **03**(12): p. 1690–1697.
4. Pashtoon, M. I., S. Miakhil, and M. M. Behsoodi, *Waste Glass Powder ' An Alternative of Cement in Concrete ' : A Review*. International Journal of Current Science Research and Review, 2022. **05**(07): p. 2541–2549.
5. Kalakada, Z., J. Doh, and S. Chowdhury, *Glass powder as replacement of cement for concrete – an investigative study*. European Journal of Environmental and Civil Engineering, 2019. **26**(3): p. 1046–1063.
6. Khan, F. A., K. Shahzada, Q. S. Ullah, M. Fahim, S. W. Khan, and Y. I. Badrashi, *Development of environment-friendly concrete through partial addition of waste glass powder (WGP) as cement replacement*. Civil Engineering Journal, 2020. **6**(12): p. 2332–2343
7. Khatib, J. M., E. M. Negim, H. S. Sohl, and N. Chileshe, *Glass Powder Utilisation in Concrete Production*. European Journal of Applied Sciences, 2012. **4**(4): p. 173–176.
8. Mahmoud, A. S., M. M. Yassen, and S. M. Hama, *Effect of glass powder as partial replacement of cement on concrete strength and stress-strain relationship*. Developments in eSystems Engineering (DeSE), 2019. **20**: p. 109–114.
9. Raju, S. and P. R. Kumar, *Effect of Using Glass Powder in Concrete.* International Journal of Innovative Research in Science, Engineering and Technology, 2014. **03**(5): p. 421–427.
10. Islam, G. M. S., M. H. Rahman, and N. Kazi, *Waste glass powder as partial replacement of cement for sustainable concrete practice*. International Journal of Sustainable Built Environment, 2016. **6**(1): p. 37–44.
11. Jiang, Y., T. Ling, K. Hung, and C. Shi, *A critical review of*

waste glass powder – Multiple roles of utilization in cement-based materials and construction products. Journal of Environmental Management, 2019. **242**: p. 440–449.

12. Jani, Y., and W. Hogland, *Waste glass in the production of cement and concrete - A review*. Journal of Environmental Chemical Engineering, 2014. **2**(3): p. 01-34.
13. Elaqra, H. A., M. A. A. Haloub, and R. N. Rustom, *Effect of new mixing method of glass powder as cement replacement on mechanical behavior of concrete*. Construction and Building Materials, 2019. **203**: p. 75–82.
14. Malik, M. I., M. Bashir, S. Ahmad, T. Tariq and U. Chowdhary, *Study of Concrete Involving Use of Waste Glass as Partial Replacement of Fine Aggregates Replacement of Fine Aggregates*. IOSR Journal of Engineering, 2013. **3**(7): p. 7–13.
15. Pashtoon, M. I., S. Miakhil, and M. M. Behsoodi, *Waste Glass "An Alternative of Cement and Fine Aggregate in Concrete"*. International Journal of Engineering Technologies IJET, 2023. **8**(2): p. 70–76.
16. Vijayakumar, G., H. Vishaliny, and D. Govindarajulu, *Studies on Glass Powder as Partial Replacement of Cement in Concrete Production*. International Journal of Emerging Technology and Advanced Engineering, 2013. **3**(2): p. 153–157.
17. Al-jburi Najad A. A., H. Kareem, N. Azline, and N. Ostovar, *Waste glass as partial replacement in cement – A review Waste*. Sustainable Civil and Construction Engineering Conference, 2023. Avaliable from https://doi: 10.1088/1755-1315/357/1/012023.
18. Topc¸u, I. B., and M. Canbaz, *Properties of concrete containing waste glass*. Cement and Concrete Research, 2003. **34**: p. 267–274.
19. Kim, I. S., S. Y. Choi, and E. I. Yang, *Evaluation of durability of concrete substituted heavyweight waste glass as fine aggregate*. Construction and Building Materials, 2018. **184**: p. 269–277.
20. Sakale, R., and S. Jain, *Experimental Investigation on Strength of Glass Powder Replacement by Cement in Concrete with Different Dosages.* International Journal of Science Technology & Engineering, 2016. **2**(08): p. 76-86.
21. Khan, F. A., M. Fahad, K. Shahzada, H. Alam, and N. Ali, *Utilization of waste glass powder as a partial replacement of cement in concrete.* International Journal of Advanced Structures and Geotechnical Engineering, 2015. **04**(03): p. 181-185.
22. Kamali, M., and A. Ghahremaninezhad, *Effect of glass powders on the mechanical and durability properties of cementitious materials*. Construction and Building Materials, 2015. **98**: p. 407–416.
23. Silva, R. V., J. De Brito, and R. K. Dhir, *Tensile strength behaviour of recycled aggregate concrete*. Construction and Building Materials, 2015. **83**: p. 108–118.
24. Ibrahim, K. I. M., *Recycled waste glass powder as a partial replacement of cement in concrete containing silica fume and fly ash*. Case Studies in Construction Materials, 2021. **15**: Avaliable from https://doi: 10.1016/j.cscm.2021.e00630.
25. Elaqra, H., and R. Rustom, *Effects of using glass powder as cement replacement on rheological and mechanical properties of cement paste.* Construction and Building Materials, 2018. **179**: p. 326–335.
26. Olofinnade, O. M., J. M. Ndambuki, A. N. Ede, and C. Booth, *Application of Waste Glass Powder as a Partial Cement Substitute towards more Sustainable Concrete Production*. International Journal of Engineering Research in Africa, 2017. **31**: p. 77–93.
27. Afshinnia, K., and P. R. Rangaraju, *Impact of combined use of ground glass powder and crushed glass aggregate on selected properties of Portland cement concrete*. Construction and Building Materials, 2016. **117**: p. 263–272.
28. Behsoodi, M. M., M. S. Aslam, and E. Latifi, *Assessing sustainability of WASH projects in public and private schools of Jalalabad City , Nangarhar , Afghanistan*. European Journal of Sustainable Development Research, 2023. **7**(4): p. 01-06.
29. Indian Standard Recommended Guidelines For Concrete Mix Design. [MARCH 1998]; Available from https://www.academia.edu/10832787/indian_standard_recommended_guidelines_for_concrete_mix_design_gr_6.